

**CGER'S SUPERCOMPUTER MONOGRAPH REPORT Vol. 15**

**Algorithms for carbon flux estimation using GOSAT  
observational data**

Shamil Maksyutov, Yumiko Nakatsuka, Vinu Valsala, Makoto Saito,  
Nikolay Kadygrov, Tadao Aoki, Nawo Eguchi, Ryuichi Hirata, Motoyoshi Ikeda,  
Gen Inoue, Takakiyo Nakazawa, Ryo Onishi, Prabir K. Patra, Andrew D. Richardson,  
Tazu Saeki, and Tatsuya Yokota

**Center for Global Environmental Research**



**National Institute for Environmental Studies, Japan**



**CGER'S SUPERCOMPUTER MONOGRAPH REPORT Vol. 15**

**Algorithms for carbon flux estimation using GOSAT  
observational data**

Shamil Maksyutov, Yumiko Nakatsuka, Vinu Valsala, Makoto Saito,  
Nikolay Kadygrov, Tadao Aoki, Nawo Eguchi, Ryuichi Hirata, Motoyoshi Ikeda,  
Gen Inoue, Takakiyo Nakazawa, Ryo Onishi, Prabir K. Patra, Andrew D. Richardson,  
Tazu Saeki, and Tatsuya Yokota

**Center for Global Environmental Research**



**National Institute for Environmental Studies, Japan**



**Supercomputer Steering Committee (FY2009):**

Yasumasa Kanada (University of Tokyo)  
Akio Kitoh (Meteorological Research Institute)  
Koki Maruyama (Central Research Institute of Electric Power Industry)  
Akira Noda (Japan Agency for Marine-Earth Science and Technology)  
Takashi Imamura (NIES)  
Kunio Kohata (NIES)  
Kimio Matsumoto (EIC/NIES)  
Kazumi Kishibe (EIC/NIES)  
Yukihiro Nojiri (CGER/NIES)

**Coordination for Resource Allocation of the Supercomputer**

Center for Global Environmental Research  
National Institute for Environmental Studies

**Maintenance of the Supercomputer System**

Environmental Information Center  
National Institute for Environmental Studies

**Operation of the Supercomputer System:**

NEC Corporation

**Editorial Board:**

Center for Global Environmental Research

---

**Copies of this report can be obtained by contacting:**

Center for Global Environmental Research  
National Institute for Environmental Studies  
16-2 Onogawa, Tsukuba, Ibaraki 305-8506, Japan  
Fax: +81-29-858-2645  
E-mail: [www-cger@nies.go.jp](mailto:www-cger@nies.go.jp)

The report is also available as a PDF file.

See: [http://www-cger.nies.go.jp/cger-e/e\\_report/r\\_index-e.html](http://www-cger.nies.go.jp/cger-e/e_report/r_index-e.html)

**Copyright 2010:**

NIES: National Institute for Environmental Studies

This publication is printed on paper manufactured entirely from recycled material (Rank A), in accordance with the Law Concerning the Promotion of Procurement of Eco-Friendly Goods and Services by the State and Other Entities.

## Foreword

The Center for Global Environmental Research (CGER) at the National Institute for Environmental Studies (NIES) was established in October 1990. CGER's main objectives are to contribute to the scientific understanding of global change and to identify solutions for pressing environmental problems. CGER conducts environmental research from interdisciplinary, multi-agency, and international perspectives, provides an intellectual infrastructure for research activities in the form of databases and a supercomputer system, and makes the data from its long-term monitoring of the global environment available to the public.

CGER installed its first supercomputer system (NEC SX-3, Model 14) in March 1992. That system was subsequently upgraded to an NEC Model SX-4/32 in 1997 and an NEC Model SX-6 in 2002. In March 2007, we replaced the whole system with an NEC Model SX-8R/128M16 in order to provide an increased capacity for speed and storage. We expect that our research will benefit directly from this upgrade.

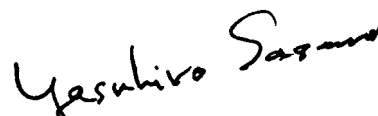
The supercomputer system is available for use by researchers from NIES and other research organizations and universities in Japan. The Supercomputer Steering Committee evaluates proposals of research requiring the use of the system. The committee consists of leading Japanese scientists in climate modeling, atmospheric chemistry, ocean environment, computer science, and other areas of concern in global environmental research.

To promote the dissemination of the results, we publish both an Annual Report and occasional Monograph Reports. Annual Reports give the results for all research projects that have used the supercomputer system in a given year, while Monograph Reports present the integrated results of a particular research program.

This volume of Monograph Report describes the main components of a modeling system that will be used for estimating regional fluxes of carbon dioxide from data obtained by the Greenhouse gases Observing SATellite (GOSAT) and ground-based instruments. The modeling system was developed using our supercomputer system. GOSAT, placed in orbit in January, 2009, is now regularly taking global measurements of carbon dioxide and methane. The data from space are expected to improve the accuracy of the current flux estimates. The result of the model calculation, which will be released from the NIES GOSAT Project, will help us gain better insight into the current trend of the global carbon budget.

In the years to come, we will continue to support environmental research with our supercomputer resources and disseminate the outcomes.

February 2010



Yasuhiro Sasano  
Director

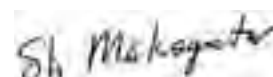
Center for Global Environmental Research  
National Institute for Environmental Studies

## Preface

The Greenhouse gases Observing SATellite (GOSAT) was successfully launched in January 2009 and has been collecting data since the completion of the initial check on the instruments onboard. It is the first high-resolution spectrometer in space designed to observe the atmospheric column abundances of carbon dioxide (CO<sub>2</sub>) and methane (CH<sub>4</sub>) over the globe. An inverse modeling system that utilizes the GOSAT observations for retrieving CO<sub>2</sub> regional fluxes is being developed and tested using the supercomputing facility available at NIES.

This volume of the CGER's Supercomputer Monograph Report is a collection of peer-reviewed published papers that described the main components of the inverse modeling system. The system consists of tracer transport models for the ocean and atmosphere, process models of the carbon cycle in the terrestrial biosphere and ocean, and inventories of anthropogenic and natural CO<sub>2</sub> fluxes. Also included in this volume, other than the descriptions of the components, is an analysis paper which evaluated the degree of contribution that the GOSAT data would make in improving the accuracy of surface CO<sub>2</sub> fluxes estimated monthly on a sub-continental scale. I hope that this issue of Monograph Report would be of a help in understanding how the regional fluxes of CO<sub>2</sub> are calculated using the GOSAT data. On behalf of the members in our research group, I would like to thank those who are involved in maintaining the supercomputers here at NIES and making it available for our researches.

February 2010



Shamil Maksyutov  
Special Senior Researcher  
Center for Global Environmental Research,  
National Institute for Environmental Studies

## Contents

Foreword .....	i
Preface .....	ii
Contents .....	iii
List of Figures .....	vii
List of Tables .....	ix

### Chapter 1

#### **NIES/FRCGC global atmospheric tracer transport model: description, validation, and surface sources and sinks inversion**

Abstract .....	2
1.1 Introduction .....	3
1.2 Model description .....	3
1.2.1 Model equations .....	4
1.2.2 Representation of the physical processes: cumulus convection .....	4
1.2.3 Representation of the physical processes: turbulent diffusion .....	6
1.2.4 Semi-Lagrangian transport and trajectory calculation .....	7
1.2.5 Model grid .....	8
1.2.6 Mass fixer description .....	9
1.2.7 Treatment of the surface emission-sink fields and chemical transformations .....	9
1.3 Validation of NIES/FRCGC global transport model .....	10
1.3.1 Evaluation of vertical transport using simulation of radon .....	10
1.3.2 Evaluation of interhemispheric transport using long-lived gases .....	12
1.3.3 CO <sub>2</sub> transport simulation with TransCom 1 experimental protocol .....	13
1.4 Introduction to high resolution model version (NIES05) .....	14
1.5 Inverse modeling of CO <sub>2</sub> sources and sinks .....	16
1.6 Conclusions .....	19
References .....	20

### Chapter 2

#### **Optimization of the seasonal cycles of simulated CO<sub>2</sub> flux by fitting simulated atmospheric CO<sub>2</sub> to observed vertical profiles**

Abstract .....	26
2.1 Introduction .....	27
2.2 Methods .....	28
2.2.1 Carbon cycle model .....	28
2.2.2 Formalism of the parameter optimization .....	30
2.2.3 Atmospheric transport model .....	30
2.2.4 Observed data of CO <sub>2</sub> .....	31
2.3 Results and discussions .....	32
2.3.1 Optimized parameters .....	32
2.3.2 Growing season net flux and NPP .....	33
2.3.3 Seasonal cycle and vertical profiles of CO <sub>2</sub> with optimized CASA NEP .....	35
2.4 Summary .....	37
References .....	38

## Chapter 3

### Design, simulation and validation of an ocean carbon cycle system using an offline Ocean Tracer Transport Model (OTTM)

Abstract .....	42
3.1 Design of an offline Ocean Tracer Transport Model (OTTM) .....	43
3.1.1 Motivation for OTTM development .....	43
3.1.2 Design .....	45
3.1.2a Vertical mixing .....	45
3.1.2b Horizontal mixing .....	47
3.1.2c Grids .....	48
3.1.3 Numerical implementation .....	49
3.2 Validation of OTTM with CFC-11 simulations .....	51
3.2.1. Data and model experiments .....	51
3.2.2 CFC-11 cycle in the ocean .....	52
3.2.2a Comparison with observations .....	54
3.2.2b Comparison with OCMIP-II participant models .....	59
3.2.2c Error comparison with OCMIP-II participant models .....	62
3.2.3 Discussion and conclusion .....	62
3.2.4 Summary .....	64
3.3 Coupling of a biogeochemical cycle to OTTM .....	64
3.3.1 Carbonate chemistry model .....	65
3.3.2 Ecosystem model .....	65
3.3.3 Data and model setup .....	66
3.3.4 The model air-sea CO <sub>2</sub> flux .....	67
3.3.5 Summary .....	69
References .....	69

## Chapter 4

### An empirical model simulating diurnal and seasonal CO<sub>2</sub> flux for diverse vegetation types and climate conditions

Abstract .....	74
4.1 Introduction .....	75
4.2 Materials and methods .....	76
4.2.1 Input data .....	76
4.2.2 Modeling approach .....	77
4.2.3 Validation data .....	82
4.3 Results and discussion .....	83
4.3.1 Variations in parameters among biomes .....	83
4.3.2 Variations in NEE .....	85
4.3.3 Nocturnal RE .....	90
4.3.4 Application to AsiaFlux ecosystems .....	91
4.4 Conclusions .....	93
References .....	93

## **Chapter 5**

### **Role of simulated GOSAT total column CO<sub>2</sub> observations in surface CO<sub>2</sub> flux uncertainty reduction**

Abstract .....	100
5.1 Introduction .....	101
5.2 Materials and methods.....	101
5.2.1 Total column CO <sub>2</sub> observations and errors.....	101
5.2.2 Time-dependent inversion of CO <sub>2</sub> .....	105
5.3 Results and discussions .....	106
5.3.1 Flux uncertainty reduction .....	106
5.3.2 Perturbed data and bias in fluxes.....	108
5.4 Conclusions .....	110
References .....	111





# List of Figures

## Chapter 1

1.1	An example of zonal average convective mass fluxes for January and July as estimated by the model.....	5
1.2	Comparisons between observations and model simulations of radon-222 averaged for 3 continental sites during winter and summer.....	11
1.3	Interhemispheric gradients in modeled and observed SF <sub>6</sub> concentrations during 1993 are depicted.....	13
1.4	Interhemispheric gradients in fossil fuel CO <sub>2</sub> tracer simulated by TransCom 1 models and NIES/FRCGC model are shown for three vertical levels..	14
1.5	Surface CO <sub>2</sub> concentrations at 03Z30AUG 2002 obtained from (a) 2×2 degrees (left) and (b) 0.25×0.25 degree (right) horizontal resolution simulation.....	15
1.6	Results of NIES05 at four kinds of resolutions at Tsukuba (36.05°N, 140.13°E) 200m high tower, which is in close proximity of megacity Tokyo (35.66°N, 139.75°E), and is occasionally under the influence of strong anthropogenic sources (an episode of up to about 70 ppm on 5 <sup>th</sup> afternoon).....	16
1.7	Long-term trends and inter-annual variability in global and regional in CO <sub>2</sub> fluxes as derived by 64-region TDI model are depicted for the period 1979-2005.....	17
1.8	The inverse modeling results for selected land regions.....	19

## Chapter 2

2.1	Map of vegetation types in CASA.....	29
2.2	(a) $E_{max}$ (b) $Q_{10}$ and of each vegetation type optimized with partial column concentrations of CO <sub>2</sub> and near-surface CO <sub>2</sub> concentration.....	32
2.3	Uncertainty reduction (%) of (a) $E_{max}$ and (b) $Q_{10}$ .....	33
2.4	Latitudinal distributions of GSNF obtained with partial-column CO <sub>2</sub> and near-surface CO <sub>2</sub> .....	35
2.5	Seasonal cycles of CO <sub>2</sub> partial column concentrations.....	35
2.6	Vertical profiles of the simulated and optimized CO <sub>2</sub> concentrations at each location.....	37

## Chapter 3

3.1	A schematic presentation of the model domain decomposition.....	49
3.2	Memory window sharing at strip boundaries.....	50
3.3	The model flow chart showing the sequence of operations in OTTM.....	50
3.4	CFC-11 concentration integrated zonally and vertically over (top) the Atlantic Ocean and inventories along (bottom left) 30°W and (bottom right) 20°W.....	53
3.5	Column inventory of CFC-11 from (left) observations and (middle) model during 1995.....	55
3.6	Model-simulated CFC-11 in the North Atlantic (middle) along 30°W during 1995, (left) corresponding observations, and (right) model error.....	57
3.7	Model-simulated CFC-11 in the North Atlantic (middle) along ~24°N during 1995, (left) corresponding observations, and (right) model error.....	57
3.8	Model-simulated CFC-11 in the North Atlantic (middle) along 40°W during 1995, (left) corresponding observations, and (right) model error.....	58
3.9	Model-simulated CFC-11 in the South Atlantic (middle) along ~0° during 1995, (left) corresponding observations, and (right) model error.....	58

3.10	Zonally integrated column inventories of CFC-11 in the entire Atlantic from the candidate models of OCMIP-2, our model, and corresponding observations.....	60
3.11	Model std dev and correlation with reference data (GLODAP) are displayed as in Taylor (2001). .....	61
3.12	Mean air-sea CO <sub>2</sub> fluxes of the model over the 1980-1999 period (molm <sup>-2</sup> yr <sup>-1</sup> ). .....	68

## Chapter 4

4.1	Dependence of normalized $P_{\max}$ on daily mean air temperature ( $T_a$ ; °C) and vapor pressure deficit (VPD <sub>a</sub> ; kPa) over 15-day periods for seven biomes. ....	78
4.2	Normalized $P_{\max}$ in evergreen needle-leaf forests (ENF) under different conditions of $T_a$ (°C) and VPD <sub>a</sub> (kPa). .....	79
4.3	Relationship between annual NPP and unstressed maximum $P_{\max}$ in evergreen needle-leaf forests. ....	80
4.4	Relationship between bin-averaged $P_{\max}$ and initial slope $\alpha$ in grassland. ....	81
4.5	Distributions of three parameters for seven biomes. ....	83
4.6	Seasonal course of weekly averaged $P_{\max}$ at (a) the Duke Forest site, ENF, in 2004; (b) the Santarem site, EBF, in 2003; (c) the Bartlett site, DBF, in 2004; and (d) the mature red pine site, MF, in 2004. ....	84
4.7	Same as Figure 4.6, but for $\alpha$ . ....	85
4.8	Diurnal and seasonal patterns of observed (left) and predicted (right) NEE at 10 AmeriFlux ecosystem sites. ....	86
4.9	Comparisons between half-hourly variations in observed and predicted NEE, averaged over 10-day periods, at 10 AmeriFlux ecosystem sites. ....	88
4.10	Seasonal courses of LAI, from the MOD15A2 for the areas surrounding the Audubon Research Ranch site, and daily precipitation in 2003. ....	89
4.11	Seasonal course of monthly averaged nocturnal RE at the Howland ENF site in 2001, the Donaldson ENF site in 2001, and the Ozark DBF site in 2007. ....	91
4.12	Same as Figure 4.9, but for four AsiaFlux ecosystem sites. ....	92

## Chapter 5

5.1	Total column CO <sub>2</sub> and errors (in ppm) for July 2005, with 1.8-ppm error for the monthly mean value ( $\sigma_{\text{syst}} = 1$ ppm). ....	102
5.2	Bias (ppm) for July 2005 (maximum value 3.9 ppm, minimum value -1.3 ppm). ....	103
5.3	Ratio $H$ of data (%) with acceptable SNRs to all observational data within a $7.5^\circ \times 7.5^\circ$ grid box in July 2005. ....	104
5.4	Cloud cover (%) measured by CALIPSO in July 2005. ....	104
5.5	Number of successful observations $N$ in July 2005. ....	105
5.6	CO <sub>2</sub> flux uncertainties in 2005 (GtC yr <sup>-1</sup> region <sup>-1</sup> ). ....	107
5.7	Monthly mean reduction ( $\times 100\%$ ) in the annual CO <sub>2</sub> flux uncertainties of GOSAT data with 1.8-ppm precision ( $\sigma_{\text{syst}} = 1$ ppm). ....	107
5.8	Relative CO <sub>2</sub> flux uncertainties for different monitoring network configurations. ....	108
5.9	Total column CO <sub>2</sub> (ppm) in July 2005, perturbed by bias. ....	109
5.10	Corrections (GtC yr <sup>-1</sup> region <sup>-1</sup> ) of <i>a priori</i> fluxes in July 2005 with different inverse model configurations. ....	109
5.11	Same as Figure 5.10c, but for the annual flux in 2005 (minimum = -0.44, maximum = 2.88). ....	110

## List of Tables

### Chapter 2

2.1	Locations and amplitudes of the CO <sub>2</sub> vertical profile data used for this study. ....	31
2.2	NPP and GSNF of each vegetation type after CASA optimizations with near-surface and partial columns of CO <sub>2</sub> .....	34

### Chapter 3

3.1	Test experiments. ....	53
3.2	Statistical summary of test-run simulations shown in Figure 3.3. ....	54
3.3	List of various data sets, periodicity and time-span. ....	65

### Chapter 4

4.1	List of AmeriFlux eddy covariance measurement sites analyzed in this study. ....	76
4.2	List of biome-specific parameter values. ....	78
4.3	List of AmeriFlux eddy covariance measurement sites used for validation.....	82
4.4	Slopes (a), intercepts (b), and $R^2$ values of regression lines, $y=ax+b$ , between the observed and modeled NEE, and the number of observations (N) at 10 AmeriFlux sites. ....	87
4.5	Same as Table 4.1, but for AsiaFlux eddy covariance measurement sites analyzed. ....	92



## Chapter 1

### **NIES/FRCGC global atmospheric tracer transport model: description, validation, and surface sources and sinks inversion**

(Published in Journal of Earth Simulator, Volume 9, 3-18, 2008. Reproduced by permission of the Earth Simulator Center / JAMSTEC.)

Shamil Maksyutov<sup>1,2</sup>, Prabir K. Patra<sup>2\*</sup>, Ryo Onishi<sup>3</sup>, Tazu Saeki<sup>4</sup>, and Takakiyo Nakazawa<sup>5</sup>

1. Center for global Environmental Research, National Institute for Environmental Studies, Tsukuba, Ibaraki 305-8506, Japan
2. Frontier Research Center for Global Change/JAMSTEC, Yokohama, Kanagawa 236-0001, Japan
3. Earth Simulator Center/JAMSTEC, Yokohama, Kanagawa 236-0001, Japan
4. Research Institute for Humanity and Nature, Kyoto 603-8047, Japan
5. Graduate School of Science, Tohoku University, Sendai, Miyagi 980-8578, Japan

\*Corresponding author: Dr. Prabir K. Patra, Atmospheric Composition Research Program, Frontier Research Center for Global Change/JAMSTEC, 3173-25 Showa-machi, Yokohama Kanagawa 236-0001, Japan. E-mail: [prabir@jamstec.go.jp](mailto:prabir@jamstec.go.jp)

## Abstract

We present description, validation, utilization, and update of the NIES/FRCGC (National Institute for Environmental Studies/Frontier Research Center for Global Change) off-line global atmospheric tracer transport model. The model transport is driven by analyzed meteorological fields and designed to simulate seasonal and diurnal cycles, synoptic variations, and spatial distributions of atmospheric chemical constituents in the troposphere. Tracer transport is simulated with semi-Lagrangian transport algorithm. The vertical mixing by the boundary layer turbulence and penetrative convection are parameterized. We have tested the model performance against observations of radon-222 and SF<sub>6</sub>. The long-lived tracer transport properties are also compared to the other models and observations using the simulation of atmospheric CO<sub>2</sub>. Our results suggest that the model can produce realistic interhemispheric exchange rate and vertical tracer distributions in lower and mid troposphere. A new version (NIES05) of the transport model has been developed for simulating diurnally varying CO<sub>2</sub> concentrations at much finer horizontal resolution (0.25°×0.25°×47 levels). The high resolution model results show large improvements in match with the observations at a continental site in Tsukuba (~50km north-east of Tokyo). The NIES/FRCGC model is adopted to run on Earth Simulator for the purpose of source/sinks inversion of atmospheric CO<sub>2</sub>. We used interannually varying meteorology for the forward simulations of known CO<sub>2</sub> fluxes and normalized emissions from 64 divisions of the globe for which CO<sub>2</sub> fluxes are determined by inverse modeling of atmospheric CO<sub>2</sub>. We have discussed the long-term trends and inter-annual variability in global and regional CO<sub>2</sub> fluxes. The results suggest weak increases and reduction in total land/ocean and southern ocean sinks, respectively, for the period of 1982-2004. The estimated land flux variabilities have been explained by accounting ecosystem response to inter-annual climate variability and forest fires.

***Keywords: Forward transport model, High-resolution CO<sub>2</sub> simulations, Inverse modeling of CO<sub>2</sub>, Sources and sinks***

## 1.1 Introduction

Atmospheric transport has to be accounted for when analyzing the relationships between observations of atmospheric constituents and their sources/sinks near the earth's surface or through the chemical transformation in the atmosphere. The tracer transport modeling is done on different scales from local plume spread, regional mesoscale transport to global scale analysis, depending on scales of the phenomena. The global atmospheric tracer transport models are usually applied to studies of the global cycles of the long-lived atmospheric trace gases such as carbon dioxide ( $\text{CO}_2$ ) and methane ( $\text{CH}_4$ ), because the long-lived tracers exhibit observable global patterns (e.g. interhemispheric gradient of the concentration). Global modeling analysis has helped to identify the relative contribution of the land and oceans in Northern and Southern hemisphere to the interhemispheric concentration differences for  $\text{CO}_2$ ,  $\text{CH}_4$ , carbon monoxide and other tracer species (e.g. Bolin and Keeling, 1963; Hein et al., 1997). For the case of the stable and slowly reacting chemical species, a number of studies have derived information on the spatial and temporal distribution of the surface sources and sinks by applying transport model and atmospheric observations (e.g., Tans et al., 1990; Rayner et al., 1999).

In this paper we present the development of a global atmospheric tracer transport model, its application for retrieving  $\text{CO}_2$  flux variability by time-dependent inversion (TDI), and finally recent updates for high resolution simulations using improved meteorology. Our main objective is to model the sub-grid scale physical process parameterizations tuned to recent observations, and at the same time trying to maintain flexibility to choose meteorological input, model resolution and other practical considerations. For atmospheric tracers with a life time longer than several months, an accurate simulation of interhemispheric transport rate appears to be important for global scale analysis, because it affects critically the results for regional or hemispheric breakdown of unknown fluxes, such as the terrestrial  $\text{CO}_2$  sink. Another important feature is a vertical profile of the tracer concentration over emitting regions, influenced by a rate of PBL mixing with free troposphere. Global tracer transport model intercomparison studies (e.g., Jacob et al., 1997; Law et al., 1996; Denning et al., 1999) demonstrated that the sizable difference in vertical mixing rates exists between models, and discrepancies between models and observations appear to be significant for the well established climate and transport models.

## 1.2 Model description

In this section, we describe our model design and numerical representation of the model processes, including the model equations, physical processes parameterizations and their numerical realizations. The development of NIES/FRCGC model reported here is to simulate the seasonal cycles of the long-lived tracer species at a relatively coarse grid resolution (2.5 to 5 degrees longitude-latitude), and to perform sources/sinks inversion of atmospheric  $\text{CO}_2$ . The transport model has been improved by increasing spatial resolution and driven by diurnal cycle resolving meteorology for simulating diurnal-synoptic scale variations (version: NIES05). Present model version evolved since early 1990s (Akimoto et al., 1993; Maksyutov, 1994; Maksyutov and Inoue, 2000; Maksyutov et al., 2000). Several model algorithms and parameterizations tested in this process and were replaced or refined in order to produce more realistic simulation of the various atmospheric tracers.



### 1.2.1 Model equations

We use a terrain-following  $\sigma$  vertical coordinate (Philips, 1957), which is defined by expression:  $\sigma = p / p_s$ , where  $p$  and  $p_s$  are atmospheric and surface pressures, respectively. Atmospheric constituent transport equation can be presented in the Lagrangian-style form (Williamson and Laprise, 2000):

$$\begin{aligned} \frac{dq^k}{dt} &= \frac{\partial q^k}{\partial t} + \mathbf{V} \cdot \nabla_{\sigma} q^k + \dot{\sigma} \cdot \frac{\partial q^k}{\partial \sigma} = \frac{\partial}{\partial \sigma} F^k + S^k \\ \nabla_{\sigma} &= \frac{\partial}{R \cos(\phi) \partial \lambda} + \frac{\partial}{R \partial \phi} \end{aligned} \quad (1)$$

Here  $q^k$  is the mixing ratio (volume) in dry air for tracer  $k$ ,  $F^k$  is the vertical flux due to turbulent diffusion and moist convective transport.  $S^k$  is a mixing ratio tendency due to surface fluxes and chemical transformations,  $\lambda$  and  $\phi$  are longitude and latitude in radians,  $R$  is the radius of the Earth, and  $\mathbf{V}$  the horizontal wind velocity vector with longitudinal and latitudinal components ( $u$ ,  $v$ ).  $\dot{\sigma}$  is vertical wind velocity in  $\sigma$ -coordinate system ( $\dot{\sigma}$  = +ve indicates downward motion). Eqn. (1) is solved using single time-level, time splitting scheme, with separate consecutive steps for surface emissions and transformations, semi-Lagrangian transport, vertical mixing by penetrative convection (all explicit), and vertical diffusion by turbulence (implicit). The winds ( $u$ ,  $v$ ) are interpolated from the global analysis winds. Vertical subgrid-scale fluxes  $F^k$  are obtained using parameterizations of the penetrative cumulus convection and PBL climatology. The vertical wind in sigma coordinates  $\dot{\sigma}$  is derived diagnostically from the global analysis winds. It is assumed that vertical velocity in global analysis  $\omega$  represents a mass flow through constant pressure surface, and is prepared using the equation (see Washington and Parkinson, 1986):

$$\omega = p_s \cdot \dot{\sigma} + \sigma \cdot \left( \frac{\partial p_s}{\partial t} + \mathbf{V} \cdot \nabla_{\sigma} p_s \right), \quad (2)$$

which includes effects of air motion with respect to constant sigma surfaces (as pressure and sigma planes are not parallel) and surface pressure tendency. The  $\dot{\sigma}$  is calculated from Eqn. 2 according to

$$p_s \cdot \dot{\sigma} = \omega - \sigma \cdot \left( \frac{\partial p_s}{\partial t} + \mathbf{V} \cdot \nabla_{\sigma} p_s \right).$$

### 1.2.2 Representation of the physical processes: cumulus convection

The vertical redistribution of tracers by cumulus convection is based on cumulus mass-fluxes calculated in a Kuo-type scheme following Grell et al. (1995), and modified to include entrainment and detrainment processes on convective updrafts and downdrafts proposed by Tiedtke (1989). In this formulation the cloud base level  $\sigma_c$  is obtained by adding small perturbation to humidity and temperature at levels below 700 hPa and adiabatically lifting the air parcel until the condensation occurs. For cloud base  $\sigma_c$  we use the lowest level where condensation would occur, known as lifting condensation level. The supply rate of moisture

available for penetrative convection is then estimated. The horizontal moisture divergence is evaluated from analysis winds and water vapor content (threshold at the cloud base is set to 0.0002 kg/kg). Low-level moisture convergence  $M_1$  is obtained by integrating the horizontal moisture convergence below cloud base level:

$$M_1 = - \left[ \int_{\sigma_c}^1 \nabla_{\sigma} (p_s \cdot \mathbf{V} \cdot q) d\sigma - M_c \right] + S_{evap}. \quad (3)$$

$S_{evap}$  is surface evaporation. For evaporation climatology, we use monthly surface evaporation fields by NASA GEOS-1 reanalysis for 1992-1993 (Schubert et al., 1993). Use of the monthly evaporation rate for estimating the moisture divergence has been tested by Heimann (1995). To account for deviation from the mass conservation in the wind data the moisture divergence term is corrected for non-zero divergence of the air mass  $M_c$ :

$$M_c = \int_{\sigma_c}^1 q \cdot \nabla_{\sigma} (p_s \cdot \mathbf{V}) d\sigma.$$

The mass flux  $M_u$  in updraft is set to  $M_1$  divided by water vapor mixing ratio at cloud base  $q_{base}$ , so that  $M_1 = M_u \cdot q_{base}$ . The vertical profiles of entrainment and detrainment rates are set proportional to  $M_u$  in accordance with Tiedtke (1989). The cloud top is determined by comparing the virtual potential temperatures in the updraft and environment, for which an overshoot of 3 degrees K is allowed. The clouds thinner than  $\Delta\sigma = 0.1$  are excluded. The downdraft mass flux is set to 0.2 of that in the updraft. The vertical distribution of zonal average cumulus mass flux on updrafts is presented in Figure 1.1, which clearly shows the location of the tropical convective cell moving along with the seasonal changes in solar insolation, from southern hemisphere in January to northern hemisphere in July. Also the overall seasonal features in mid-latitude convective zones are well captured.

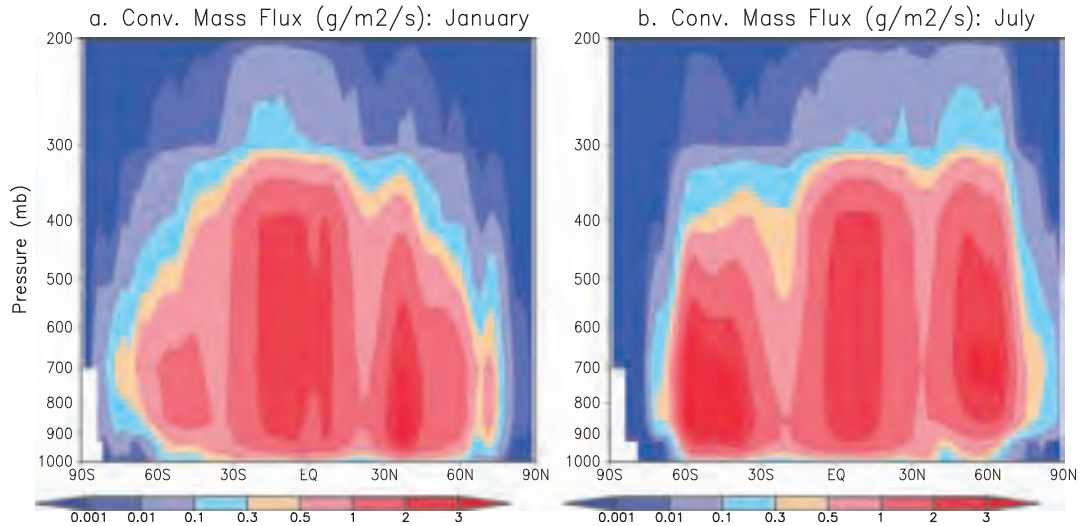


**Figure 1.1** An example of zonal average convective mass fluxes for January and July as estimated by the model.

The tracers are transported vertically by applying a simplified explicit scheme. It is assumed that the updrafts and downdrafts make only a negligibly small part of a grid column; the rest is designated as environment air. First, the vertical profiles of the concentrations in the updraft and downdraft air are computed taking into account rates of mixing with environment air by entrainment and detrainment, and then the concentration tendencies in environment air are obtained from entrainment/detrainment rates.

### 1.2.3 Representation of the physical processes: turbulent diffusion

We used climatological planetary boundary layer (PBL) heights to separate transport processes in the well-mixed PBL and free troposphere. The monthly averages of daily maximum PBL thickness data are prepared from 3-hourly PBL height data at GEOS-1 reanalysis dataset for 1992 - 1993 (Schubert et al., 1993). Daily maximum height is selected to representative time of trace gas observations. The summer-time PBL height over mid-latitude continental areas varies around 150 hPa, approximately 1.5 km. The optimal procedure to derive the monthly PBL climatology can be debated. The other problem is a lack of day to day variability. To overcome this problem and perform more realistic simulation of diurnal cycle, newer version of the model (version: NIES05) uses diurnally varying PBL heights at three-hourly interval contained in the ECMWF analysis and forecast products.

Below the PBL top, the turbulent diffusivity is set to a constant value of  $40 \text{ m}^2/\text{s}$ . The large scale transport such as zonally-averaged vertical profiles of constituents does not change appreciably by decreasing the diffusivity to  $20 \text{ m}^2/\text{s}$ . The selection of the turbulent diffusivity value inside the PBL seems to be not critical as far as vertical profiles in well-mixed daytime conditions are concerned (in the older version). Above the PBL top, the turbulent diffusivity  $K_T$  is calculated using a local stability function, as in Hack et al. (1993):

$$K_T = l^2 \cdot S \cdot F_S(Ri) .$$

Here,  $l$  is a mixing length ( $l = 30 \text{ m}$ ).  $S = \left| \frac{\partial \mathbf{V}}{\partial z} \right|$  is a vertical wind shear.  $Ri$  is a local Richardson number, defined with temperature and wind gradients as:

$$Ri = \frac{g}{S^2} \cdot \frac{\partial \ln \theta_v}{\partial z} .$$

$\theta_v$  is a virtual potential temperature,  $g$  is the acceleration of gravity. The stability dependent function  $F_S(Ri)$  is defined as:

$$F_S(Ri) = (1 - 18 \cdot Ri)^{1/2} \text{ for unstable conditions } (Ri < 0) \text{ and}$$

$$F_S(Ri) = 1 - \frac{Ri}{Ri_C} \text{ for stable conditions } (0 < Ri < Ri_C),$$

where  $Ri_C = 0.2$  is a critical Richardson number, above which  $F_S(Ri) = 0$ .

### 1.2.4 Semi-Lagrangian transport and trajectory calculation

Semi-Lagrangian transport algorithm is an effective way to solve the tracer transport problems in a polar coordinate system (Williamson and Rasch, 1989), as opposed to the regular-grid schemes formulated in flux form, that have a singularity near the poles caused by small grid size in longitudinal direction. In the semi-Lagrangian approach the tracer concentration change due to transport from initial state (time  $t_0$ ) to new value at next time step  $t_0 + \Delta t$  is evaluated in 2 steps:

Step 1 (Trajectory calculation): For the each grid point location a three-dimensional trajectory is calculated for an air parcel, which arrives to that grid point at time  $t_0 + \Delta t$ . The trajectory location at time  $t_0$  is designated as departure point, and the trajectory itself is called a back trajectory, because it is calculated backward in time.

Step 2 (Interpolation): A concentration at departure point at time  $t_0$  is obtained using interpolation from nearby grid point values. In the absence of mixing and transformation processes, concentration at arrival point should be exactly the same as that at the departure point, thus the tracer concentrations at new time step  $t_0 + \Delta t$  are set to those at corresponding departure points.

The trajectories are calculated using explicit integration of the air parcel motion in the Cartesian coordinate system originated in the Earth center. The coordinate transformation from polar to Cartesian coordinate system and back is used on the each time step. Calculation of the departure point on each time step is done in 3 sub-steps:

- a) Interpolate wind and pressure to the current air parcel position in polar coordinates, using bilinear approximations.
- b) Convert the winds and air parcel coordinates to Cartesian coordinate system centered at the Earth center, and calculate displacement tangent to Earth surface.
- c) Convert new position back to polar coordinate system and finding sigma level change by integrating vertical motion.

We provide here a short description of the trajectory calculation equations (as referred in Step 1 above). The horizontal (parallel to Earth surface) air parcel movement is determined in the earth-centered coordinate system. The earth centered system has x-axis passing the point on the Earth surface at  $0^\circ$  East,  $0^\circ$  North; y-axis passes via  $90^\circ$ E,  $0^\circ$ N, z-axis passing via  $90^\circ$  North. Horizontal motion in polar coordinates ( $\lambda, \phi$ ) can be represented as

$$R \cdot \cos(\phi) \frac{d\lambda}{dt} = u, \quad R \cdot \frac{d\phi}{dt} = v.$$

The air parcel displacement in the earth-centered system is given by

$$\begin{aligned} dx &= -\delta\phi \cdot \sin(\phi) \cdot \cos(\lambda) - \sin(\phi) \cdot \delta\lambda \\ dy &= -\delta\phi \cdot \sin(\phi) \cdot \cos(\lambda) + \cos(\phi) \cdot \delta\lambda, \\ dz &= -\delta\phi \cdot \cos(\phi) \end{aligned}$$

where  $dx$ ,  $dy$ ,  $dz$  are air parcel displacements in  $x$ ,  $y$ ,  $z$  directions in the earth-centered coordinate system.  $\delta\lambda$  and  $\delta\phi$  are displacements in longitude, latitude directions, calculated as:

$$\delta\lambda = u \cdot \Delta t = u / (R \cos \phi) \delta t, \quad \delta\phi = v \cdot \Delta t = (v / R) \delta t.$$

Here,  $\Delta t$  is a time step (negative for back-trajectory). A new position of the air parcel is given by

$$x = R \cdot \cos(\phi) \cdot \cos(\lambda) + dx$$

$$y = R \cdot \cos(\phi) \cdot \sin(\lambda) + dy.$$

$$z = R \cdot \sin(\phi) + dz$$

$x, y, z$  are longitudinal, latitudinal, and vertical positions of the air parcel.  $R$  is the radius of the Earth. After the position in the earth-centered coordinate system is determined, the position in the polar coordinate system is given by:

$$\phi = \arctan(z / \sqrt{x^2 + y^2}) \quad \lambda = \arctan(y / x).$$

This trajectory calculation module has been extensively used for analysis of the relationship between the atmospheric transport and observed time series of the long-lived tracers such as nitrous oxide (Tohjima et al., 2000), methane (Tohjima et al., 2002) and ozone (Pochanart et al., 2001). The studies were performed with the same wind and trajectory calculation algorithm as in the present three-dimensional transport model, and a good correlation was observed between the variations of the atmospheric composition and trajectory pathways over a time periods extending from 1994 to 1999. Those results give us some degree of confidence in the model's horizontal transport performance.

### 1.2.5 Model grid

The model's horizontal and vertical resolutions match those of the meteorological dataset when possible. We use pressure level ECMWF operational analyses at 12-hour time step and 2.5 degree horizontal resolution in our model validation experiments, and NCEP reanalysis data at the same resolution for multiyear inverse model simulations (ECMWF, 1999; Courtier et al., 1998). The same horizontal resolution is used in the model; however, the grid layout is different from the meteorological dataset. The first model grid cell on a horizontal plane is located near South Pole, and is confined between (0° E, 90° S) and (2.5° E, 87.5° S). The last one, at North Pole, is confined between (357.5° E, 87.5° N) and (0° E, 90° N). Vertical grid layout was designed to provide enough layers to match the resolution of the wind dataset (ECMWF operational analyses), and the variability in the boundary layer height. The validation tests were performed with 15-layer vertical grids, which have slab centers at  $\sigma_K = \{.97, .93, .89, .85, .775, .7, .6, .5, .4, .3, .25, .2, .15, .1, 0.03\}$ . The slab interfaces are at mid levels  $\sigma_{K+1/2} = (\sigma_K + \sigma_{K+1})/2$ . The model grid is staggered in the vertical dimension. Turbulent diffusivities and convective mass fluxes are assigned to slab interfaces  $\sigma_{K+1/2}$ , while the winds, temperature, and humidity are assigned to slab centers  $\sigma_K$ . The winds are interpolated from the meteorological analysis grid to the model grid using bilinear interpolation in longitudinal, latitudinal, and vertical directions.

The NIES05 model version uses the NCEP operational meteorological analysis data having 26 vertical levels and 1×1 degree horizontal resolution and provided at a six-hour interval. The NIES05 model simulations are performed at various horizontal resolutions, e.g., 0.5×0.5, 1×1, and 2×2 degrees. This version has 47 vertical layers.

### 1.2.6 Mass fixer description

The total tracer mass tendency by the semi-Lagrangian transport algorithm usually deviates from zero, which is often negligible in short term but can disturb the global trends and tracer budgets in long-term simulations. A variety of mass fixers are applied in transport models in order to keep total tracer mass unchanged during transport (Hack et al., 1993; Rasch et al., 1995). We distribute the required correction proportionally to local advection tendencies as described in Taguchi (1996). The mass fixer is designed to conserve as total tracer mass, which is calculated as an integral (with constant factor omitted):

$$M_q = \int_0^1 \int_{-1}^1 \int_0^{2\pi} p_s \cdot (1 - 0.61 \cdot q_w) \cdot q \cdot d\lambda \cdot d(\sin \phi) \cdot d\sigma \quad (4)$$

Here  $q_w$  is a water vapour mixing ratio, so  $(1 - 0.61 \cdot q_w)$  is a dry air mass fraction. Mass fixer is designed to conserve  $M_q$  by balancing the positive and negative tendencies. The constraint for tracer tendencies on each time step is derived from the mass balance equation (Eqn. 4) as follows

$$\frac{\partial}{\partial t} M_q = \int_0^1 \int_{-1}^1 \int_0^{2\pi} \left\{ p_s \cdot (1 - 0.61 \cdot q_w) \cdot \tilde{q} + q \cdot \frac{\partial}{\partial t} [p_s \cdot (1 - 0.61 \cdot q_w)] \right\} \cdot d\lambda \cdot d(\sin \phi) \cdot d\sigma = 0.$$

Here  $\tilde{q}$  is a corrected tendency for each tracer. We apply two different factors,  $a_p$  and  $a_n$ , as multipliers for positive and negative tendencies and obtain

$$\tilde{q} = \dot{q} \cdot [a_p \cdot \theta(\dot{q}) + a_n \cdot \theta(-\dot{q})],$$

where  $\dot{q}$  is a tracer tendency from semi-Lagrangian transport step,  $\theta(\dot{q})$  is a step function ( $\theta(x) = 1$  for  $x \geq 0$ , and  $\theta(x) = 0$  for  $x < 0$ ). The condition  $\max(a_p, a_n) = 1$  is enforced to keep the solution monotonic.

Recent tests conducted for TransCom 3 intercomparison experiment (Gurney et al., 2002) revealed that the mass fixer we use does have a detectable non-local (“teleconnection”) effect. It is caused by the values of  $a_p$  and  $a_n$  being slightly different for each particular tracer. The values of  $a_p$  and  $a_n$  influence the rate of interhemispheric transport, and the difference is generally larger than that for other mass fixers (R. Law, personal communication, 2001), such as flat concentration adjustment (Hack et al., 1993).

### 1.2.7 Treatment of the surface emission-sink fields and chemical transformations

The model is designed to handle constant surface emission fields and seasonally changing emissions in the form of 12 monthly average fields per year. The NIES05 version can ingest fluxes at higher frequency, at up to hourly time interval. The monthly average emissions are interpolated linearly to daily values, and on the 15<sup>th</sup> of each month the emission rate is equal to the monthly average for that month as provided by emission inventory files. The emission inventory fields have higher resolution (e.g.,  $1 \times 1$  degree), than the model grid (e.g.,  $2.5 \times 2.5$  degrees), so the input dataset is mapped to a model grid by counting the overlap area of each



input data cell to all model grid data cells. That assures that the global total emission flux is conserved during interpolation.

### 1.3 Validation of NIES/FRCGC global transport model

An effective way to validate the atmospheric transport models is by simulating the non-reacting or slowly reacting atmospheric tracer species with well-known emissions and transformations. The tracers of choice are both short-lived species like radon-222 for diagnosing local/regional transport (Jacob et al., 1997) and long-lived species for evaluating large scale/interhemispheric transport such as SF<sub>6</sub> (Denning et al., 1996; Levin and Hesshaimer, 1996; Maiss et al., 1996), <sup>85</sup>Kr (Jacob et al., 1987; Heimann and Keeling, 1989; Zimmermann et al., 1989), and chlorofluorocarbons (Prather et al., 1987; Mahowald et al., 1997). General requirements to the suitable tracer species can be summarized as follows: a) availability of reliable emission inventory; b) stable emissions with little seasonal and diurnal variations; c) availability of the observations at required temporal and spatial scales. Most of naturally emitted gaseous species like carbon dioxide, methane, and carbon monoxide can not be used for the model validation because of the large and poorly known spatial-temporal variability of their sources and sinks. Among the most widely used are the gases of the anthropogenic origin – SF<sub>6</sub> and chlorofluorocarbons, because their emission rates are constrained by both the industrial statistics and the trends in global atmospheric content and in addition have no known chemical loss in the troposphere. On the other hand radon-222 (atmospheric residence time of 3.8 days) is emitted only naturally, but its emission rate is related to stable factors, such as type of soil and rocks, rather than the changing vegetation or weather conditions.

We evaluate the model's overall performance using results from several extensively-tested global tracer transport models and comparing our model simulations with observations. Those model simulations include the WCRP model intercomparison experiment for radon (Jacob et al., 1997), TransCom experiment (Law et al., 1996) for CO<sub>2</sub> transport intercomparison, and SF<sub>6</sub> transport intercomparison experiment TransCom 2 (Denning et al., 1996). These modeling setups were developed by large transport modeling community, and provide concise and tested sets of atmospheric observations and surface emission fields. This gives us an opportunity to concentrate on limited number of key and integral simulated tracer field parameters. The limited set of tests may not actually substitute running the comprehensive validation using large variety of observations (e.g., Dentener et al., 1999), but can still give valuable information on the model performance in terms of large scale averages.

#### 1.3.1 Evaluation of vertical transport using simulation of radon

Radon-222 is a product of radium-226 decay and has a lifetime of 3.8 days in the atmosphere. The surface radon emission rate varies considerably from 0.5 to 2 atoms/cm<sup>2</sup>/s; the emission is suppressed by poorly conducting wet soils and snow cover. Yet there is no better choice of relatively short-lived and widely observed tracer for validating a transport model for continental and remote oceanic atmosphere, and between boundary layer and free troposphere. For validating the model performance using transport of radon-222, we follow the World Climate Research Program (WCRP) inter-comparison experiment specification (Jacob et al., 1997). Radon-222 surface fluxes were set to 0.005 atoms/cm<sup>2</sup>/s for oceans and 1

atom/cm<sup>2</sup>/s over land between 60° S to 60° N, and to 0.005 atoms/cm<sup>2</sup>/s for land between 60° N to 70° N.

The observed and simulated radon concentrations for different heights at Crozet, Hawaii and Cincinnati are compared (not shown) by using the data at Cincinnati (Gold et al., 1964), Crozet (Lambert et al., 1995), and Hawaii (Kritz et al., 1990). The model appears to under-predict surface concentrations at Cincinnati and upper atmospheric observations over Hawaii (200 hPa level), and slightly over-predict the observations at Crozet island. Worth mentioning, however, that several models that participated in Jacob et al. (1997) inter-comparison also failed to capture observed variability in the upper troposphere and reproduce the high radon observed values at 200 hPa over Hawaii. Crozet Island is located south of African coast; the data indicate low background concentrations of below 10<sup>-21</sup> mol/mol, with infrequent high radon episodes lasting few days. In case of Crozet, Jacob et al. (1997) found that the low background concentrations are over-predicted; but the amplitude of the high radon episodes is captured more successfully by the “established” transport models, which is believed to be an indication of models’ ability to transport radon to remote atmosphere without significant amplitude loss due to diffusion. The summer maximum at Crozet in our model is within the range of the observed variability.

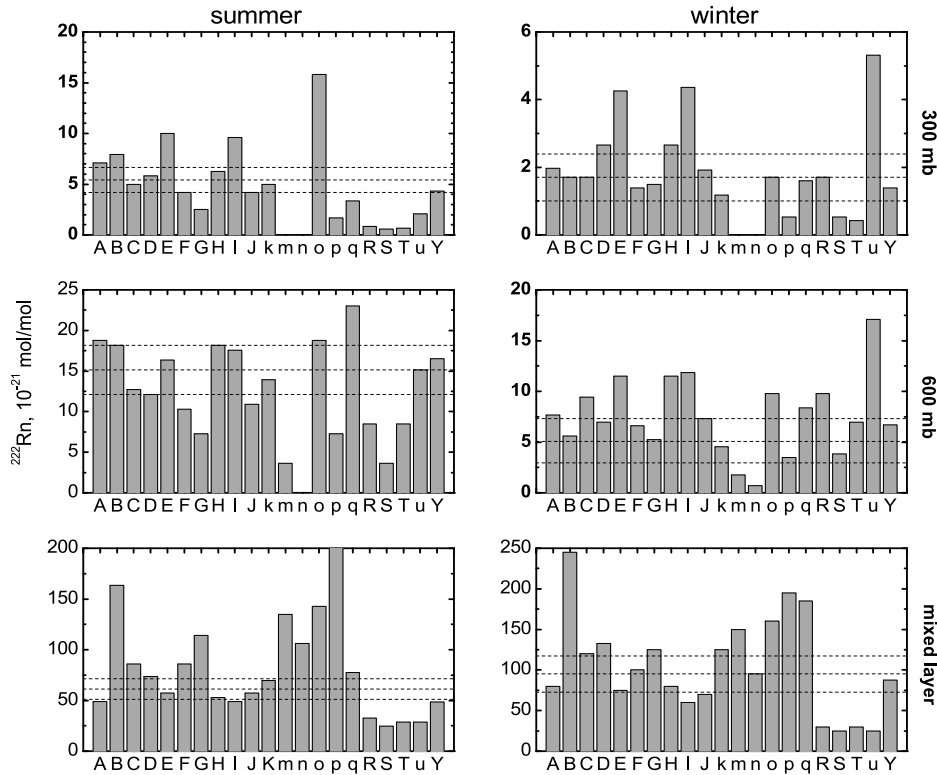


**Figure 1.2 Comparisons between observations and model simulations of radon-222 averaged for 3 continental sites during winter and summer.** Results at three vertical levels (surface, 600 mb and 300 mb) are shown. Models A to J are established three-dimensional models, models k to q are three-dimensional models under development, R to U are two-dimensional models, and Y is for this model. Observations are taken at Cincinnati (40°N, 84°W), Socorro (34°N, 107°W) and Kirov (58°N, 49°E). Different model results are designated by letters along the x-axis: A. CCM2, B. ECHAM3, C. GFDL/ZODIAC, D. GISS/H/I, E. KNMI/TM2, F. LLNL/GRANTOUR, G. LLNL/E, H. LMD, I. TM2Z, J. MOGUNTIA, k. CCC-GCM, m. LaRC, n. LLNL/IMPACT, o. MRI, p. TOMCAT, q. UGAMP, R. AER, S. UCAMB, T. HARWELL, u. UW, Y. NIES/FRCGC (this work).

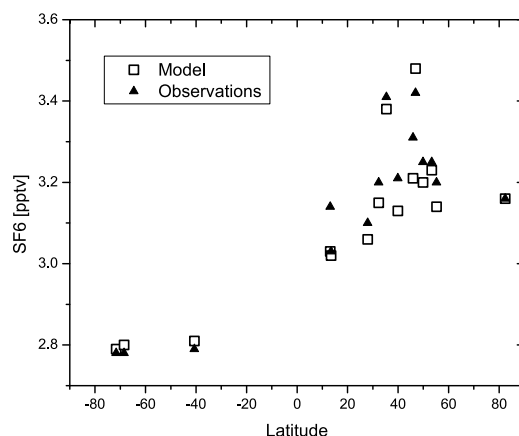


Figure 1.2 shows the comparison of winter and summer averages together with other model results as presented by Jacob et al. (1997). The comparison to the observations concludes that our model performs similarly to the established three-dimensional transport models (see Figure 1.2 caption for details), and the model simulated vertical profiles are close to observed ones. The model results are within the range of observations (widened by observed variability) for all but summer mixed layer value. Even in the later case it is close to lower bound of the observation ranges. This may indicate that the summer time mixing (ventilation of the boundary layer) is stronger than that occur in the real world. The same conclusion is also applicable to some other transport models as well (see Figure 1.2). However, this low value is not conclusive evidence in the view of the fact that the local emission rate uncertainty could be as high as 50%.

### 1.3.2 Evaluation of interhemispheric transport using long-lived gases

The validation of the inter-hemispheric and vertical transport became more reliable with the increasing availability of the observational data on a stable tracer, SF<sub>6</sub>, which can be analyzed accurately in the laboratory after sampling to flasks, has a long atmospheric lifetime of more than 3000 years (Ravishankara et al., 1993), has steady emissions, verifiable via global atmospheric abundance observations (Levin and Hesshaimer, 1996; Geller et al., 1997). We follow the TransCom 2 protocol (Denning et al., 1999) in applying the global emission scenario for SF<sub>6</sub>, and present the 5-year simulation that starts from globally homogeneous concentration of 2 pptv (parts per trillion volume) at the beginning of 1989. In Denning et al. (1999) intercomparison the initial value was set to 2.06 pptv, and that resulted some overestimation of the global 1993 average by all models. They had to scale down the concentration increase by a factor of 0.936, which may be interpreted as the same amount of decrease in emission rate considering linearity in SF<sub>6</sub> transport.

The annual average of simulated SF<sub>6</sub> concentration for 1993 is compared to the observations compiled by Denning et al. (1999) and plotted in Figure 1.3. The common problems that can be observed with both our model and models reported by Denning et al. (1999), are large mismatch for Barbados (13°N, 59°W), and large variability in mismatch for continental and background Northern hemispheric background locations. The pole-to-pole difference (South Pole to Alert) is captured fairly well by our model. Similar simulations of fossil fuel component of CO<sub>2</sub> flux are also conducted. We estimate an interhemispheric exchange time of about 1.5 year and 0.9 year by considering the hemispheric means of surface concentrations and values integrated for the whole hemisphere, respectively.



**Figure 1.3 Interhemispheric gradients in modeled and observed SF<sub>6</sub> concentrations during 1993 are depicted.** The modeling set up for this simulation is similar to TransCom 2 experiment (see text).

According to the data presented, the model in a given configuration tends to under-predict inter-hemispheric gradient in background locations by 10% of interhemispheric difference (taken as 0.4 pptv), but at the continental sites the difference can be both positive and negative. The average mismatch is comparable to that by other established transport models in TransCom 2 intercomparison, but indicates that there are scopes for further improvements in forward modeling as well as the spatial distribution of SF<sub>6</sub> emission. The wish list for those improvements would include: a) increasing the interhemispheric gradient in background atmosphere by extra 10% to improve the match between model and observations at background locations, and b) at the same time keep the match at continental locations within present level. The later action would require enhancing the vertical mixing in lower troposphere potentially leading to widening the mismatch with radon-222 data as in Figure 1.2. Some of these improvements are introduced in the NIES05 version of the model and some results have been discussed later.

### 1.3.3 CO<sub>2</sub> transport simulation with TransCom 1 experimental protocol

Another test of the model performance is given by the TransCom 1 intercomparison study, which provides the handy set of parameters for evaluating both the horizontal (interhemispheric) and vertical tracer transport by comparison with the established models. Here we report the simulation results for “fossil fuel CO<sub>2</sub>” tracer, as specified by Law et al. (1996). The fossil fuel CO<sub>2</sub> source field derived by Inez Fung is the same as in Tans et al. (1990), and is based on CO<sub>2</sub> emission inventory by Marland (1989). The results are presented as averages for North and South Hemispheres for surface level, 500 hPa, and 200 hPa levels. The interhemispheric concentration gradient defined as difference in hemispheric averages simulated by our model and models reported by Law et al. (1996) are summarized in Figure 1.4. According to previous studies with short/long-lived tracers, such as Jacob et al. (1987), Denning et al. (1999), the extensively validated models such as GISS and TM2 are capable of reproducing the interhemispheric gradient of the long-lived tracers with the accuracy of about 10% or better. We use the same yard-stick for evaluating the performance of our model. NIES/FRCGC model is not considerably different from TM2 in terms of the North-South difference at surface. Along with several other global tracer transport models it predicts about 3-ppm difference at surface, however there is a difference in vertical profile of

interhemispheric gradient. At the level of 500 hPa, the relative difference between models becomes larger with TM2 and GISS showing larger interhemispheric difference as compared to others. At 500 hPa our model also produces larger gradient than other models, and difference from TM2 is minor. That is not the case at 200 hPa level. As one can see on Figure 1.4, the North-South difference at 200 hPa is as large as 1.5 ppm for GISS and TM2, and about 1 ppm or less for our and other models. Main reason is a stronger vertical transport in GISS and TM2 models, which also makes smaller the model simulated difference between continental boundary layer and background oceanic air, as discussed in Law et al. (1996) and Denning et al. (1999).

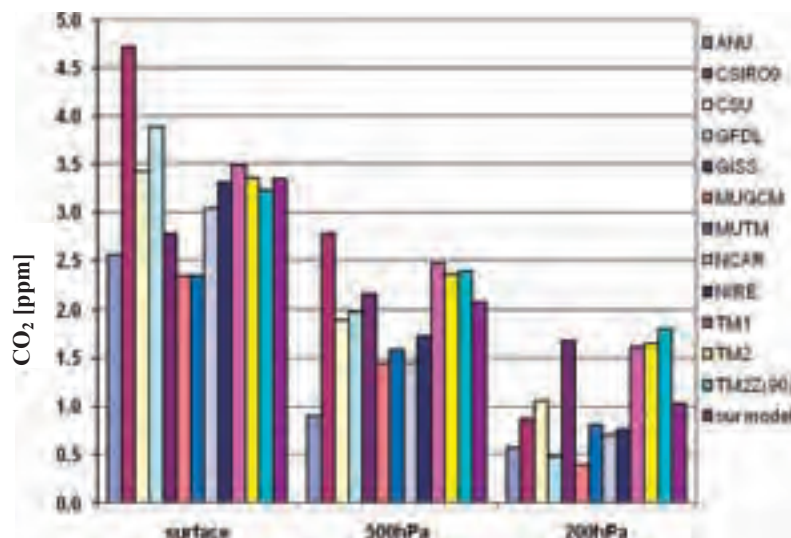


**Figure 1.4** Interhemispheric gradients in fossil fuel CO<sub>2</sub> tracer simulated by TransCom 1 models and NIES/FRCGC model are shown for three vertical levels.

## 1.4 Introduction to high resolution model version (NIES05)

While the NIES/FRCGC model successfully captures overall features in tracer transport and being used for CO<sub>2</sub> sources/sinks estimation by inverse modeling of atmospheric CO<sub>2</sub> (section 1.5), there are increasing demands for simulating tracer distributions at sub-daily time and local scales. Presently about 30 stations are observing atmospheric CO<sub>2</sub> using in situ deployed instruments and provide hourly average values for scientific research (WDCGG, 2007). To understand the observed variability, the transport model simulations are required to be performed at increased spatial resolution and driven by diurnally varying meteorology. We have run our transport model (version NIES05) as high horizontal resolution as 0.25×0.25 degree longitude-latitude, in order to investigate the impact of grid resolution on global CO<sub>2</sub> transportation. Here, we present our simulation results at 4 kinds of horizontal resolutions; 2×2, 1×1, 0.5×0.5 and 0.25×0.25 degrees. The vertical resolution is enhanced to 47 levels for better resolving the mixing processes in the boundary layer. For resolving the diurnal variations in surface concentrations, the NIES05 model version is driven by 3-hourly PBL height data from ECMWF analyzed and forecast products ([http://www.ecmwf.int; path:/products/data/operational\\_system](http://www.ecmwf.int; path:/products/data/operational_system)). The other 2-D and 3-D meteorological parameters, e.g., sea-level pressure, winds, temperature, are taken from NCEP final analysis (<http://dss.ucar.edu; path:/datasets/ds083.2/>). Computational demand increased many-fold to run the model at 0.5×0.5 degree horizontal resolution and 47 vertical level; e.g., time and

memory size required for one month simulation of 3 tracers are 1.4 hours in real time and 4.4 GB, respectively on 6 CPUs of Earth Simulator (NEC SX-6 series processor).

Three surface CO<sub>2</sub> fluxes are used; SiB2 hourly varying terrestrial ecosystem flux (Denning et al., 1996), seasonally varying ocean flux (Takahashi et al., 2002) and anthropogenic fossil fuel emissions (Marland, 1989) following the TransCom continuous experiment protocol (Law et al., 2006). Higher resolution anthropogenic CO<sub>2</sub> emission distributions are generated from 1×1 degree emission inventory, by redistributing the fluxes spatially following the 2.5min global population map data (CIESIN, 2000), and combined with lower resolution ecosystem and oceanic flux data. This redistribution procedure for fossil fuel emission is an approximation and should ideally be placed according to the source locations. The summation of those fluxes is considered as the total CO<sub>2</sub> surface flux. August 2002 is selected as the target period of our test simulation. The preceding simulation (spin-up run) is performed at 2×2 degree horizontal resolution for the period of 1st January to 31st July, 2002 in order to obtain realistic spatial CO<sub>2</sub> gradients. Figure 1.5 shows the snapshots of surface CO<sub>2</sub> distributions over East Asia at the resolutions of (a) 2×2 and (b) 0.25×0.25 degree. Though the area-averages concentrations are similar in both cases, the distribution patterns are quite different from each other. For example, Figure 1.5b shows much clearer city plumes than Figure 1.5a. It also shows clearer vortex shape due to a typhoon near the Kyusyu area (130°E, 30°N).

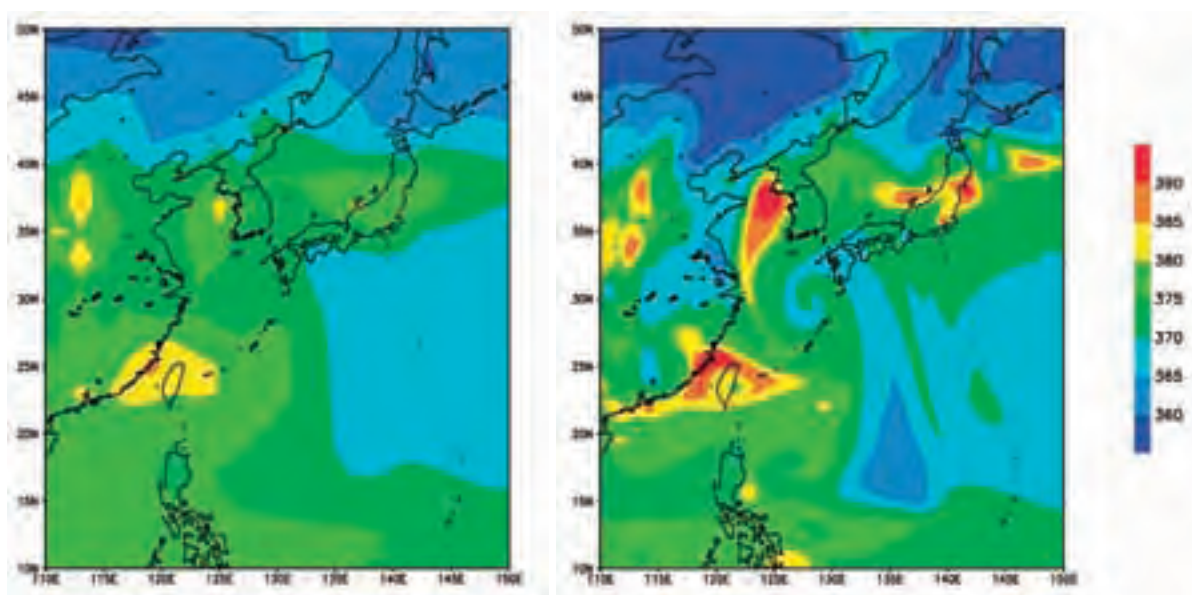


**Figure 1.5 Surface CO<sub>2</sub> concentrations at 03Z30AUG 2002 obtained from (a) 2×2 degrees (left) and (b) 0.25×0.25 degree (right) horizontal resolution simulation.**

Figure 1.6 shows a comparison of atmospheric CO<sub>2</sub> data at Tsukuba 200 m tall tower with NIES05 model results at different horizontal resolutions. Tsukuba is located close to a large anthropogenic CO<sub>2</sub> emission region around Tokyo (distance ~50 km). The observation data are provided by Y. Sawa and H. Matsueda of Meteorological Research Institute (MRI), Tsukuba (also available at WDCGG website). Each simulation result has its offset value, which is determined from the average value in the August. The higher-resolution simulations have stronger diurnal changes, which are more consistent with observed diurnal cycle.

Furthermore, they produce better predictions, particularly during the 3rd to 7th August period when winds from Tokyo dominate. Model simulations at horizontal resolution of  $1\times 1$  degree or coarser do not resolve the separation between Tokyo and Tsukuba emissions and transport as Tokyo and Tsukuba reside within the same grid cell and sampling grid do not accurately represents Tsukuba (see Figure 1.6 caption). The nearest north-eastern model grid is selected for sampling, and the distance between model grids and Tsukuba are estimated to be about 128, 58, 23 and 8 km for  $2\times 2^\circ$ ,  $1\times 1^\circ$ ,  $0.5\times 0.5^\circ$  and  $0.25\times 0.25^\circ$  horizontal resolutions, respectively. Thus the highest resolution run enables us to capture the  $\text{CO}_2$  variabilities more realistically compared to the coarse resolution runs.

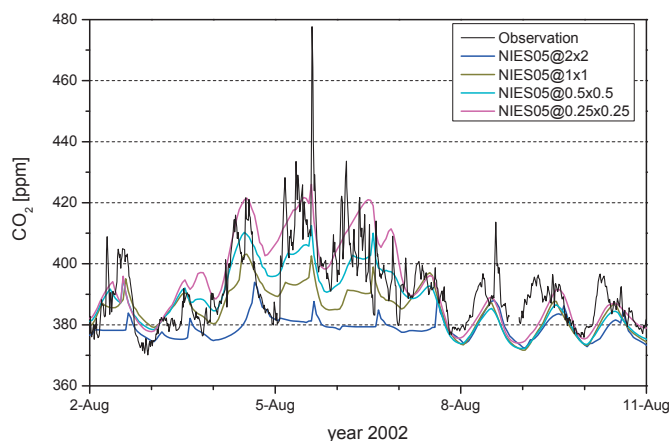


**Figure 1.6 Results of NIES05 at four kinds of resolutions at Tsukuba ( $36.05^\circ\text{N}$ ,  $140.13^\circ\text{E}$ ) 200 m high tower, which is in close proximity of megacity Tokyo ( $35.66^\circ\text{N}$ ,  $139.75^\circ\text{E}$ ), and is occasionally under the influence of strong anthropogenic sources (an episode of up to about 70 ppm on 5<sup>th</sup> afternoon). An offset of 373 ppm is added to the model values for comparison with observations. The model sampling grids are located at ( $37^\circ\text{N}$ ,  $141^\circ\text{E}$ ), ( $36.5^\circ\text{N}$ ,  $140.5^\circ\text{E}$ ), ( $36.25^\circ\text{N}$ ,  $140.25^\circ\text{E}$ ) and ( $36.13^\circ\text{N}$ ,  $140.13^\circ\text{E}$ ) in  $2\times 2^\circ$ ,  $1\times 1^\circ$ ,  $0.5\times 0.5^\circ$  and  $0.25\times 0.25^\circ$  model resolutions, respectively.**

The simulations of  $\text{CO}_2$ , radon-222 and  $\text{SF}_6$  at hourly, daily and synoptic time scales are being evaluated under the TransCom continuous intercomparison project (Law et al., 2006). Though the first forward simulation results are encouraging this model version will not be used in surface  $\text{CO}_2$  sources/sinks inversion for resolving flux variabilities at high spatial and temporal resolutions, until a rigorous evaluation of model simulations of the above mentioned species is completed.

## 1.5 Inverse modeling of $\text{CO}_2$ sources and sinks

Using the NIES/FRCGC model version ( $2.5 \times 2.5$  horizontal resolution and 17 vertical layers) we have employed a 64-region time-dependent inverse model (TDIM) for deriving  $\text{CO}_2$  fluxes at monthly time interval from atmospheric  $\text{CO}_2$  data at 87 stations. Our 64-region TDIM is based on that has been used in Rayner et al. (1999) and partially follows the TransCom3 protocol (Gurney et al., 2000). The results have been widely reported by analyzing inter-annual variability in fluxes (Patra et al., 2005a; 2005b), and for understanding



the anomalous CO<sub>2</sub> growth rate at Mauna Loa during 2001-2003 (Patra et al., 2005c). Fluxes for oceanic regions have been validated in comparison with independent oceanic-pCO<sub>2</sub> inversion and explored for mechanistic understanding of the flux variabilities using biogeochemical models of land and ocean (Patra et al., 2006b; 2007). Here we will present some recent developments that support the derived flux variabilities and trends by our TDIM setup. In addition, NIES/FRCGC model has been utilized exclusively for optimization of futuristic surface observation networks and to study utility of satellite measurements in surface sources/sinks estimation. Most of these studies are conducted using synthetic data experiments in time-independent inversion mode for 22, 42 or 432 region divisions of the globe (Maksyutov et al., 2003a; 2003b; Patra et al., 2002; 2003a; 2003b). Multi-model intercomparisons of time-independent and time-dependent CO<sub>2</sub> flux inversions are done under the TransCom3 project (Gurney et al., 2002; 2003; 2004; Law et al., 2003; Baker et al., 2006; Patra et al., 2006a). The inverted fluxes corresponding to NIES/FRCGC model are found to be similar to most other 12 or 16 participating models.

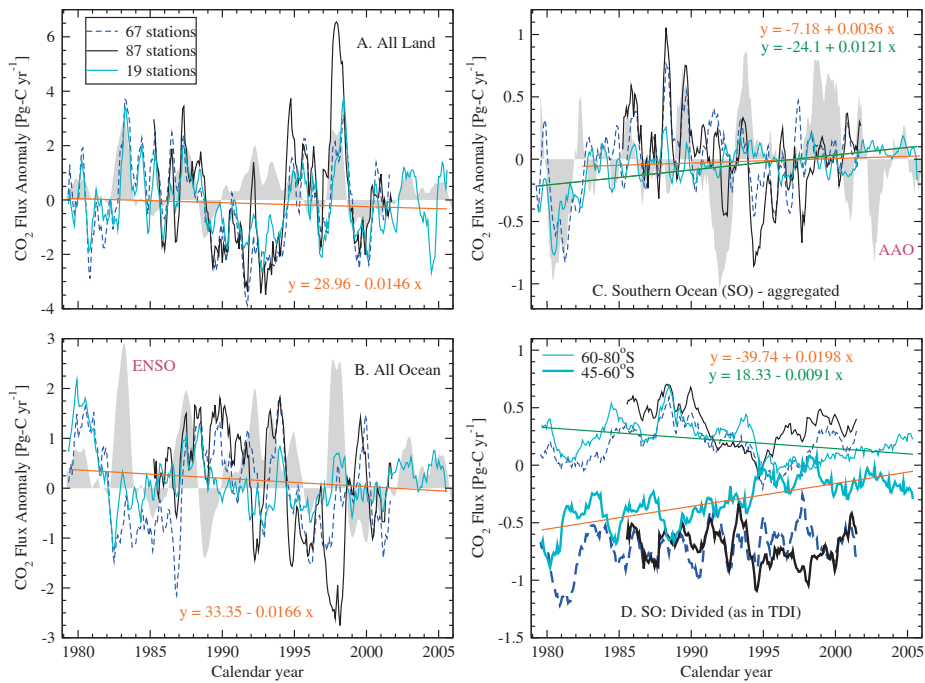


**Figure 1.7 Long-term trends and inter-annual variability in global and regional in CO<sub>2</sub> fluxes as derived by 64-region TDI model are depicted for the period 1979-2005.** The NIES/FRCGC model is used for forward transport simulations and atmospheric CO<sub>2</sub> data are taken from three different observation networks consisting of 87, 67 and 19 stations. Linear fits to the fluxes using 19 stations network are shown as straight lines (panels A and B: orange line, Panel C: green and orange lines for 1979-2005 and 1982-2005 periods, respectively, Panel D: green and orange lines for southern and northern SO parts, respectively). In Panel D, absolute fluxes for two SO regions as in the TDIM are shown: thick and thin lines are for northern and southern parts, respectively. Note all other panels show flux anomalies. The shaded curves are for El Niño Southern Oscillation (ENSO; source: [www.cdc.noaa.gov](http://www.cdc.noaa.gov)) and Antarctic Oscillation (AAO; source: [www.cpc.ncep.noaa.gov](http://www.cpc.ncep.noaa.gov)) indices.

Figure 1.7 shows the TDIM estimated fluxes for the period 1979-2005 using NIES/FRCGC forward model simulations driven by interannually varying winds (TDI/64-IAV), and cyclostationary winds and CO<sub>2</sub> measurements at 67 stations (TDI/64-CYC/67) and

19 stations (TDI/64-CYC/19). Use of cyclostationary winds and smaller CO<sub>2</sub> data network significantly reduces the interannual variability in TDIM derived CO<sub>2</sub> fluxes for both the land and ocean regions (see Patra et al., 2006b for a discussion). However, the trends in fluxes are fairly independent of the forward model transport. Total land and ocean sinks appear to be increasing over the 1980-2005 periods (Figure 1.7a and b) though the inter-annual variability has large influence on the trends derived, i.e., selection of period for trends estimation has measureable impact on the value itself. Similar is the situation for regional flux trends. Recently, trends in CO<sub>2</sub> exchange over the Southern Ocean (SO) have drawn considerable attention (see Le Quéré et al., 2007 and references therein). Their analysis also use results from an atmospheric CO<sub>2</sub> inversion that employs independent technique and derives fluxes at forward model grid resolution (Rödenbeck, 2005). Our model results also suggest a decrease in SO CO<sub>2</sub> sink in the past 2.5 decades but the magnitude of net decrease can be debated and vary between 0.04-0.1 Pg-C/decade depending on period of the fits, and appears to follow the trends in AAO (Figure 1.7c). More detailed look in to the fluxes corresponding to northern (40-60°S) and southern (60-80°S) parts of SO suggests that the former region tending to become a weaker sink of CO<sub>2</sub> (Figure 1.7d), where the biological uptake is prominent. In contrast, the net release from southern part indicates a decrease over our analysis period where the sea-air CO<sub>2</sub> exchange is believed to be controlled by coastal upwelling.

Greater flux anomalies estimated using 64-region inverse model and observations at 87-stations have generated curiosity in the scientific community (e.g., McKinley et al., 2006). The flux variability for total land and ocean show good correspondence with ENSO cycle and vary in opposite phase with each other (Figure 1.7a and b). The amplitude and phase correspondence weakens for total ocean flux variability if atmospheric CO<sub>2</sub> data at smaller number of sites is used in TDIM calculation, and amplitude of total land flux variability reduces although the phase remains fairly similar. Comparison of TDI/64-IAV derived flux anomalies with the estimates based on observations have been done for some of the ocean regions (Patra et al., 2005a). Both approaches result in similar magnitudes in flux anomalies for Equatorial Pacific, North Atlantic and North Pacific. Using an ocean biogeochemical elemental cycling model, sensitivity studies indicate flux anomalies to changes in nutrient supply through dust deposition from the atmosphere can partly explain the TDI/64-IAV derived CO<sub>2</sub> flux anomalies (see Patra et al., 2007 for details). The full range of IAVs for the ocean regions are encompassed by the sensitivity runs selected in that analysis when the dust-iron input is varied by ten times or one-tenth.

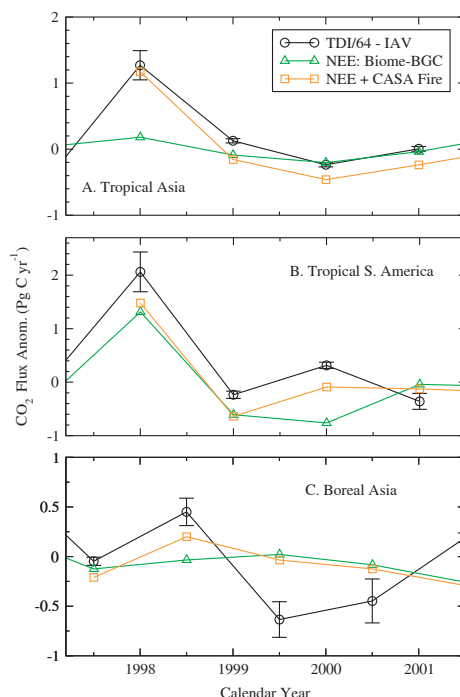


**Figure 1.8 The inverse modeling results for selected land regions.** Biome-BGC + GFED2 fire match with TDI fluxes (observation network of 87 stations case).

For the land regions, analysis using a simulation setup of Biome-BGC terrestrial ecosystem model underestimated the TDI estimated flux variability (Patra et al., 2005b), and they attributed the mismatch between the two to the lack biomass burning processes in Biome-BGC model. Reliable estimates of monthly-mean CO<sub>2</sub> fluxes due to fires (referred to as fire CO<sub>2</sub> flux) for several years have now been produced based on satellite derived burned area estimates, CASA terrestrial ecosystem model based fuel load inventories and known emission factors (van der Werf et al., 2006; version GFED2). Figure 1.8 shows a comparison of Biome-BGC net ecosystem exchange (NEE) and fire CO<sub>2</sub> flux (bottom-up estimate) with that estimated by TDI/64-IAV (top-down). For most of the years, the bottom-up and top-down estimates agree very well (difference within 10%), with the exception of Boreal Asia region for the period 1999-2000 only. This comparison further enhances our confidence in the derived flux IAV in the TDI/64-IAV inversion.

## 1.6 Conclusions

Our “off-line” global atmospheric tracer transport model features a blend of established and newer approaches to representing the physical processes in the atmosphere important for atmospheric tracer transport. The semi-Lagrangian transport algorithm is combined with climatological PBL scheme and penetrative cloud convection parameterization to give a model capable of simulating the variations of the atmospheric tracers at a monthly and longer time scales. The chosen combination of the parameterizations proved to be effective in reproducing observed vertical and horizontal distributions of the passive atmospheric constituents with accuracy similar to those of the established atmospheric transport models. Test problems suite included transport of radon-222 as in WCRP transport model intercomparison experiment, sulfur hexafluoride (SF<sub>6</sub>) following TransCom 2 model



intercomparison, and CO<sub>2</sub> as in TransCom 1 intercomparison experiments. Vertical profiles of radon-222 are simulated successfully except for some possible underestimation of the surface concentrations in summer. The simulations of the long-lived tracers SF<sub>6</sub> and CO<sub>2</sub> demonstrated satisfactory performance in the interhemispheric transport. Strength of interhemispheric gradient in tracer transport is important for realistic estimation of sources/sinks estimation using inverse modeling of atmospheric CO<sub>2</sub> and satisfactory results are obtained for annual and monthly mean flux inversions. We have reviewed the CO<sub>2</sub> sources/sinks inversion results using a 64-region time-dependent inverse model using atmospheric CO<sub>2</sub> data and NIES/FRCGC transport model driven by interannually varying meteorology. Some recent developments in capturing the inter-annual variations in CO<sub>2</sub> fluxes and short-term trends are discussed. Our model results are supported by other independent estimates. Further tests and improvements in the forward transport model design are achieved for better simulation of day-to-day and diurnal variability in the tracer concentrations. The newer model version (NIES05) uses diurnally varying PBL (3-hour interval), and 6-hourly pressure level meteorological parameters (U, V, T etc.). This model is run at one of the finest horizontal resolutions (0.25°×0.25°) globally and 47 layers. The finest -resolution simulation shows remarkable improvements for matching the observations from a tower near to the megacity Tokyo.

## Acknowledgments

We are grateful to H. Akimoto and G. Inoue for supporting this research at FRCGC and NIES. The global meteorological analysis data were provided by the ECMWF, NASA/GSFC DAO, and NCEP/NCAR. Authors thank M. Heimann for providing information on TM2 model design that facilitated development of our cumulus parameterization scheme. This work is benefited from discussions with S. Taguchi and Y. Takayabu.

## References

- Akimoto, H., Maksyutov, S., Ueda, H. (1993) Three-dimensional numerical model of atmospheric pollutant transport and transformation. - In: Proc. 2-nd Symposium of Supercomputer Society, Tokyo, Nov. 1992, CRC Research Institute, 18-23.
- Baker, D.F., et al. (2006) TransCom 3 inversion intercomparison: Impact of transport model errors on the interannual variability of regional CO<sub>2</sub> fluxes, 1988–2003. *Global Biogeochem. Cycles*, 20, GB1002.
- Bolin, B., Keeling, C.D. (1963) Large scale atmospheric mixing as deduced from seasonal and meridional variations of the atmospheric carbon dioxide. *J. Geophys. Res.*, 68, 3899-3920.
- CIESIN (2000) The Center for International Earth Science Information Network, Earth Institute, Columbia University, New York ([www.ciesin.columbia.edu](http://www.ciesin.columbia.edu)).
- Courtier, P., Andersson, E., Heckley, W., Paillex, J., et al. (1998) The ECMWF implementation of the three-dimensional variational assimilation (3D-Var), I, Formulation. *Quart. J. Roy. Meteor. Soc.*, 124, 1783-1807.
- Denning, A.S., Randall, D.A., Collatz, G.J., Sellers, P.J. (1996) Simulations of terrestrial carbon metabolism and atmospheric CO<sub>2</sub> in a general circulation model, Part 2: Simulated CO<sub>2</sub> concentrations. *Tellus*, 48B, 543-567.

- Denning, A.S., Holzer, M., Gurney, K.R., Heimann, M., et al. (1999) Three-dimensional transport and concentration of SF<sub>6</sub>: A model intercomparison study (TransCom 2). *Tellus*, 51B, 266-297.
- Dentener, F., Feichter, J., Jeuken, A. (1999) Simulation of the transport of Rn222 using on-line and off-line global models at different horizontal resolutions: a detailed comparison with measurements. *Tellus*, 51B, 573-602.
- ECMWF, ECMWF/WCRP Level III-A Global Atmospheric Data Archive, ECMWF (<http://www.ecmwf.int>), 1999.
- Geller, L.S., Elkins, J.W., Lobert, J.M., Clarke, A.D., Hirst, D.F., Butler, J.H., Meyers, R.C. (1997) Tropospheric SF<sub>6</sub>: Observed latitudinal distribution and trends, derived emissions and interhemispheric exchange time. *Geophys. Res. Lett.*, 24, 675-678.
- Grell, G., Dudhia, J., Stauffer, D. (1995) A Description of the Fifth-Generation Penn State/NCAR Mesoscale Model (MM5). NCAR/TN-398, 122 pp.
- Gold, S., Barkhau, H., Shleien, W., Kahn, B. (1964) Measurement of naturally occurring radionuclides in air. In: *The natural radiation environment*, edited by J.A.S. Adams and W.M. Lowder, Univ. of Chicago Press, Chicago, Ill., 369-382.
- Gurney, K.R., Law, R.M., Rayner, P.J., Denning, A.S. (2000) TransCom-3 experimental protocol. Paper No. 707, Dept. Atmos. Sci., Colo. State Univ.
- Gurney, K.R., Transcom3 modellers (2002) Towards robust regional estimates of CO<sub>2</sub> sources and sinks using atmospheric transport models. *Nature*, 415, 626-630.
- Gurney, K.R., Transcom3 modellers (2003) TransCom-3 CO<sub>2</sub> inversion intercomparison: 1. Annual mean control results and sensitivity to transport and prior flux information. *Tellus*, 55B, 555-579.
- Gurney K.R., Transcom3 modellers (2004) Transcom 3 inversion intercomparison: Model mean results for the estimation of seasonal carbon sources and sinks. *Global Biogeochem. Cycles*, 18, GB1010.
- Hack, J.J., Boville, B.A., Briegleb, B.P., Kiehl, J.T., Rasch, P.J., Williamson, D.L. (1993) Description of the NCAR community climate model (CCM2), NCAR/TN-382, 108 pp.
- Heimann, M., Keeling, C.D. (1989) A three dimensional model of atmospheric CO<sub>2</sub> transport based on observed winds: 2. Model description and simulated tracer experiments. In: *Aspects of Climate Variability in the Pacific and the Western Americas*, Ed. D.H. Peterson, American Geophysical Union, Washington DC, 237-275.
- Heimann, M. (1995) The TM2 tracer model, model description and user manual. DKRZ Report, No. 10, Hamburg, 47 pp.
- Hein, R., Crutzen, P.J., Heimann, M. (1997) An inverse modeling approach to investigate the global atmospheric methane cycle. *Global Biogeochemical Cycles*, 11, 43-76.
- Jacob, D.J., Prather, M.J., Wofsy, S.C., McElroy, M.B. (1987) Atmospheric distribution of <sup>85</sup>Kr simulated with a general circulation model. *J. Geophys. Res.*, 92, 6614-6626.
- Jacob, D., Prather, M.J., Rasch, P.J., Shea, R.-L., et al. (1997) Evaluation and intercomparison of global transport models using <sup>222</sup>Rn and other short-lived tracers. *J. Geophys. Res.* 102, D5, 5953-5970.
- Kritz, M.A., Le Roulley, J.-C., Danielsen, E.F. (1990) The China Clipper, Fast advective transport of radon-rich air from the Asian boundary layer to the upper troposphere near California. *Tellus*, 42B, 46-61.
- Lambert, G., Polian, G., Ardouin, B., Renault, J., Balkanski, Y. (1995) CFR Database of <sup>222</sup>Rn, <sup>220</sup>Rn and <sup>210</sup>Pb in Subantarctic and Antarctic atmosphere. Centre des Faibles Radioactiv., Gif-sur-Yvette, France.
- Law, R., Rayner, P., Denning, A.S., Erickson, D., et al. (1996) Variations in the modelled atmospheric transport of carbon dioxide and its consequences for CO<sub>2</sub> inversions. *Global Biogeochem. Cycles*, 10, 783-796.
- Law, R.M., Transcom3 modellers (2003) TransCom 3 CO<sub>2</sub> inversion intercomparison: 2. Sensitivity of annual mean results to data choices. *Tellus*, 55B, 580-595.
- Law, R.M., Peters, W., Rödenbeck, C. (2006) Protocol for TransCom continuous data experiment, Purdue Clim. Change Res. Center Tech. Rep., ([www.purdue.edu/path:/transcom/pdf/transcom/protocol\\_v5.pdf](http://www.purdue.edu/path:/transcom/pdf/transcom/protocol_v5.pdf)).

- Le Quéré, C., Rödenbeck, C., Buitenhuis, E.T., Conway, T.J., Langenfelds, R., Gomez, A., Labuschagne, C., Ramonet, M., Nakazawa, T., Metz, N., et al. (2007) Weakening of the Southern Ocean sink of CO<sub>2</sub>. *Science*, 316.
- Levin, I., Hesshaimer, V. (1996) Refining of atmospheric transport model entries by the globally observed passive tracer distributions of <sup>85</sup>Kr and sulfur hexafluoride (SF<sub>6</sub>). *J. Geophys. Res.*, 101, 16745-16755.
- Maiss, M., Steele, L.P., Francey, R.J., Fraser, P.J., Langenfelds, R.L., Trivett, N.B.A., Levin, I. (1996) Sulfur hexafluoride – a powerful new atmospheric tracer. *Atmos. Environ.*, 30, 1621-1629.
- Mahowald, N.M., Prinn, R.G., Rasch, P.J. (1997) Deducing CCl<sub>3</sub>F emissions using an inverse method and a chemical transport model with assimilated winds. *J. Geophys. Res.*, 102, 28127-28138,
- Maksyutov, S. (1994) Short-term simulations of atmospheric methane concentrations with a global tracer transport model. In: International Symposium on Global Cycles of Atmospheric Greenhouse Gases, Sendai, Japan, 333-336.
- Maksyutov, S., Inoue, G. (2000) Vertical profiles of radon and CO<sub>2</sub> simulated by the global atmospheric transport model. In: CGER Supercomputer activity report, CGER-I039-2000, CGER NIES, Tsukuba, Japan, 7, 39-41.
- Maksyutov, S., Fujita, D., Saeki, T., Nakazawa, T. (2000) Tracer transport model validation and model-simulated CO<sub>2</sub> cycle over continents. *EOS Trans.*, v.81, n.48, AGU Fall Meet. Suppl., abstract B21F-08.
- Maksyutov, S., Patra, P.K., Inoue, G. (2003a) Pseudo-data inversion of column-CO<sub>2</sub> observations by remote sensing using a high resolution inverse model. *Int. Archives of Photogrammetry, Remote Sensing and Spatial Inform. Sci.*, Vol.XXIV, Part. 7/W14.
- Maksyutov, S., Machida, T., Mukai, H., Patra, P.K., Nakazawa, T., Inoue, G., TransCom-3 modelers (2003b) Effect of recent observations on Asian CO<sub>2</sub> flux estimates with transport model inversions. *Tellus*, 55B(2), 522-529.
- Marland, G. (1989) Fossil fuels CO<sub>2</sub> emissions: Three countries account for 50% in 1986 - In: CDIAC Communications, Winter 1989, 1-4.
- McKinley, G.A., et al. (2006) North Pacific carbon cycle response to climate variability on seasonal to decadal timescales. *J. Geophys. Res.*, 111, C07S06.
- Patra, P.K., Maksyutov, S. (2002) Incremental approach to the optimal network design for CO<sub>2</sub> surface source inversion. *Geophys. Res. Lett.*, 29(10), 1459.
- Patra, P.K., Maksyutov, S., TransCom-3 modelers (2003a) Sensitivity of Optimal Extension of CO<sub>2</sub> Observation Networks to Model Transport. *Tellus*, 55B(2), 498-511.
- Patra, P.K., Maksyutov, S., Sasano, Y., Nakajima, H., Inoue, G., Nakazawa, T. (2003b) An evaluation of CO<sub>2</sub> observations with Solar Occultation FTS for Inclined-Orbit Satellite sensor for surface source inversion. *J. Geophys. Res.*, 108(D24), 4759.
- Patra, P.K., Ishizawa, M., Maksyutov, S., Nakazawa, T., Inoue, G. (2005a) Role of biomass burning and climate anomalies for land-atmosphere carbon fluxes based on inverse modeling of atmospheric CO<sub>2</sub>. *Global Biogeochem. Cycles*, 19, GB3005.
- Patra, P.K., Maksyutov, S., Ishizawa, M., Nakazawa, T., Takahashi, T., Ukita, J. (2005b) Interannual and decadal changes in the sea-air CO<sub>2</sub> flux from atmospheric CO<sub>2</sub> inverse modelling. *Global Biogeochem. Cycles*, 19, GB4013.
- Patra, P.K., Maksyutov, S., Nakazawa, T. (2005c) Analysis of atmospheric CO<sub>2</sub> growth rates at Mauna Loa using inverse model derived CO<sub>2</sub> fluxes. *Tellus*, 57B, 357-365.
- Patra, P.K., Transcom3 modellers (2006a) Sensitivity of inverse estimation of annual mean CO<sub>2</sub> sources and sinks to ocean-only sites versus all-sites observational networks. *Geophys. Res. Lett.*, 33, L05814.
- Patra, P.K., Mikaloff-Fletcher, S.E., Ishijima, K., Maksyutov, S., Nakazawa, T. (2006b) Comparison of CO<sub>2</sub> fluxes estimated using atmospheric and oceanic inversions, and role of fluxes and their interannual variability in simulating atmospheric CO<sub>2</sub> concentrations. *Atmos. Chem. Phys. Discuss.*, 6, 6801-6823.

- Patra, P.K., Moore, J.K., Mahowald, N., Uematsu, M., Doney, S.C., Nakazawa, T. (2007) Exploring the sensitivity of basin-scale air-sea CO<sub>2</sub> fluxes to interannual to decadal variability in atmospheric dust deposition using ocean carbon models and atmospheric CO<sub>2</sub> inversions. *J. Geophys. Res.*, 112, G02012.
- Philips, N.A. (1957) A coordinate system having some special advantages for numerical forecasting. *J. Meteorol.*, 14, 184-185.
- Pochanart, P., Akimoto, H., Maksyutov, S., Staehelin, J. (2001) Surface ozone at the Swiss alpine site Arosa: the hemispheric background and the influence of the large scale atmospheric emissions. *Atmos. Environ.*, 35, 5553-5566.
- Prather, M., McElroy, M., Wofsy, S., Russel, G., Rind, D. (1987) Chemistry of the global troposphere: Fluorocarbons as tracers of air motion. *J. Geophys. Res.*, 92, 6579-6613.
- Rasch, P.J., Boville, B.A., Brasseur, G.P. (1995) A three-dimensional general circulation model with coupled chemistry for the middle atmosphere. *J. Geophys. Res.*, 100, 9041-9071.
- Ravishankara, A.R., Solomon, S., Turnispeed, A.A., Warren, R.F. (1993) Atmospheric lifetimes of long-lived halogenated species. *Science*, 259, 194-199.
- Rayner, P.J., Enting, I.G., Francey, R.J., Langenfelds, R. (1999) Reconstructing the recent carbon cycle from atmospheric CO<sub>2</sub>,  $\delta^{13}\text{C}$  and O<sub>2</sub>/N<sub>2</sub> observations. *Tellus*, 51B, 213-232.
- Rödenbeck, C. (2005) Estimating CO<sub>2</sub> sources and sinks from atmospheric mixing ratio measurements using a global inversion of atmospheric transport. Tech. Rep. 6, Max-Planck-Institute for Biogeochemistry, P.O. Box 100164, 07701 Jena, Germany, ([http://www.bgc-jena.mpg.de/path:/mpg/websiteBiogeochemie/Publikationen/Technical\\_Reports/tech\\_report6.pdf](http://www.bgc-jena.mpg.de/path:/mpg/websiteBiogeochemie/Publikationen/Technical_Reports/tech_report6.pdf)).
- Schubert, S., Rood, R., Pfendtner, J. (1993) An assimilated dataset for Earth science applications. *Bull. Am. Met. Soc.*, 74, 2331-2342.
- Taguchi, S. (1996) A three-dimensional model of atmospheric CO<sub>2</sub> transport based on analyzed winds: model description and simulation results for TRANSCOM. *J. Geophys. Res.*, 101, 15099-15109.
- Takahashi, T., Sutherland, S.C., Sweeney, C., Poisson, A., Metzl, N., Tilbrook, B., Bates, N., Wanninkhof, R., Feely, R.A., Sabine, C., Olafsson, J., Nojiri, Y. (2002) Global sea-air CO<sub>2</sub> flux based on climatological surface ocean pCO<sub>2</sub>, and seasonal biological and temperature effects. *Deep-Sea Research Part II*, 49, 1601-1622.
- Tans, P., Fung, I., Takahashi, T. (1990) Observational constraints of the global atmospheric CO<sub>2</sub> budget. *Science*, 247, 1431-1438.
- Tiedtke, M. (1989) A comprehensive mass flux scheme for cumulus parameterization in large-scale models. *Mon. Wea. Rev.*, 117, 1779-1800.
- Tohjima, Y., Mukai, H., Maksyutov, S., Takahashi, Y., Machida, T., Utiyama, M., Katsumoto, M., Fujinuma, Y. (2000) Variations in atmospheric nitrous oxide observed at Hateruma monitoring station. *Chemosphere Global Change Science*, 2, 435-443.
- Tohjima, Y., Machida, T., Utiyama, M., Katsumoto, M., Fujinuma, Y., Maksyutov, S. (2002) Analysis and presentation of in situ atmospheric methane measurements from Cape Ochi-ishi and Hateruma Island. *J. Geophys. Res.*, 107(D12), 4148.
- van der Werf, G.R., Randerson, J.T., Giglio, L., Collatz, G.J., Kasibhatla, P.S., Arellano, A.F. Jr, (2006) Interannual variability in global biomass burning emissions from 1997 to 2004. *Atmos. Chem. Phys.*, 6, 3423-3441.
- WDCGG (2007) WMO World Data Centre for Greenhouse Gases, Japan Meteorological Agency, Tokyo (<http://gaw.kishou.go.jp>).
- Washington, W.M., Parkinson, C.L. (1986) An introduction to three-dimensional climate modeling. Oxford University Press, New York, 422 pp.
- Williamson, D.L., Rasch, P.J. (1989) Two-Dimensional Semi-Lagrangian Transport with Shape Preserving Interpolation. *Mon. Wea. Rev.*, 117, 102-129.

- Williamson, D.L., Laprise, R. (2000) Numerical approximations for global atmospheric GCMs – In: Numerical modeling of global atmosphere in the climate system. Ed. P. Mote and A. O’Neil. NATO Science Series, Kluwer Academic Publishers, Series C, 550, 127- 220.
- Zimmermann, P.H., Feichter, J., Rath, H.K., Crutzen, P.J., Weiss, W. (1989) A global three-dimensional source-receptor model investigation using  $^{85}\text{Kr}$ . Atmos. Environ., 23, 25-35.

## **Chapter 2**

### **Optimization of the seasonal cycles of simulated CO<sub>2</sub> flux by fitting simulated atmospheric CO<sub>2</sub> to observed vertical profiles**

(Published in Biogeosciences, Vol. 6, 2733-2741, 2009. Reproduced by permission of authors.)

Yumiko Nakatsuka<sup>1</sup> and Shamil Maksyutov<sup>1\*</sup>

1. Center for global Environmental Research, National Institute for Environmental Studies, Tsukuba, Ibaraki 305-8506, Japan

\*Corresponding author: Dr. Shamil Maksyutov, Center for Global Environmental Research, National Institute for Environmental Studies, 16-2 Onogawa Tsukuba Ibaraki 305-8506, Japan. E-mail: shamil@nies.go.jp

## Abstract

An inverse of a combination of atmospheric transport and flux models was used to optimize the Carnegie-Ames-Stanford Approach (CASA) terrestrial ecosystem model properties such as light use efficiency and temperature dependence of the heterotrophic respiration separately for each vegetation type. The method employed in the present study is based on minimizing the differences between the simulated and observed seasonal cycles of CO<sub>2</sub> concentrations. In order to compensate for possible vertical mixing biases in a transport model we use airborne observations of CO<sub>2</sub> vertical profile aggregated to a partial column instead of surface observations used predominantly in other parameter optimization studies. Effect of the vertical mixing on optimized net ecosystem production (NEP) was evaluated by carrying out 2 sets of inverse calculations: one with partial-column concentration data from 15 locations and another with near-surface CO<sub>2</sub> concentration data from the same locations. We confirmed that the simulated growing season net flux (GSNF) and net primary productivity (NPP) are about 14% higher for northern extra-tropical land when optimized with partial column data as compared to the case with near-surface data.

***Keywords: CO<sub>2</sub> flux optimization, Net ecosystem production, Net primary production, CASA model***



## 2.1 Introduction

Accurate estimation of the global distribution of CO<sub>2</sub> flux is important not only for making a basis for imposing the emission restriction of CO<sub>2</sub> gases on each country under international agreement, but also for understanding both natural and anthropogenic processes controlling the CO<sub>2</sub> fluxes. One common approach for estimation of CO<sub>2</sub> flux is to use atmospheric transport inversions (Gurney et al., 2002; Rödenbeck et al., 2003). With increasing number of CO<sub>2</sub> observation data becoming available recently, the use of atmospheric transport inversion will produce more reliable results (Maksyutov et al., 2003). Equally important in increasing the reliability of the atmospheric transport inversions is to increase the reliability of the background CO<sub>2</sub> fluxes that are used to derive the a-priori values of CO<sub>2</sub> concentration fields for solving the inverse problems.

Fluxes of CO<sub>2</sub> due to net ecosystem production (NEP) of terrestrial ecosystem, fossil fuel combustions, biomass burning, and exchange with ocean are major contributors to the seasonal cycle of CO<sub>2</sub> in atmosphere. Among all of these fluxes, NEP makes the largest contribution to variability in CO<sub>2</sub> in the atmosphere although it is very close to neutral over the course of a year (Tucker et al., 1986). To better understand the carbon cycle in the terrestrial ecosystem, several models have been developed to date. For example, Potsdam Model Intercomparison study compared a total of 17 global terrestrial biogeochemistry models, and analyzed these models from several aspects such as the simulated net primary productivities (NPP), using the common input data (Cramer et al., 1999).

Methods to optimize terrestrial ecosystem models with atmospheric CO<sub>2</sub> seasonal cycle vary from a model to model. One way is to adjust the model parameters one by one until a simulated physical quantity is close enough to the observed value. On the other hand, statistical approaches are commonly used to adjust model parameters. Fung et al. (1987) optimized temperature sensitivity of the ecosystem respiration globally to get a better fit of the simulated northern hemispheric CO<sub>2</sub> seasonality to the observations, and achieved quite reasonable results for the amplitude of seasonal cycle although with some problems in the phase. Later, Randerson et al. (2002) simultaneously optimized parameters of the Carnegie-Ames-Stanford Approach (CASA) terrestrial ecosystem model by incrementally varying the values of two parameters and constructing a three-dimensional plot of a cost function describing the weighted difference between modeled and observed CO<sub>2</sub> concentrations. In their study, they used the Goddard Institute for Space Studies tracer transport model to simulate the atmospheric CO<sub>2</sub> concentrations from CASA fluxes with different values of parameters (Randerson et al., 2002). Kaminski et al. (2002) simultaneously optimized 24 parameters of the Simple Diagnostic Biosphere Model (SDBM) by assimilating seasonal cycles of CO<sub>2</sub> concentrations from 41 observing sites. Further, Rayner et al. (2005) elaborated on the carbon cycle data assimilation system developed by Kaminski et al. (2002) and simultaneously optimized 57 parameters of Biosphere Energy Transfer Hydrology Scheme (BETHY) using the observed data of CO<sub>2</sub> for 1979 to 1999.

To our knowledge, these studies which used the observed CO<sub>2</sub> concentrations to optimize parameters of terrestrial ecosystem model relied upon available CO<sub>2</sub> data which are dominated by surface level measurements. However, more recent studies have revealed that the vertical mixing biases in transport models result in bias in the optimized fluxes. For example, Stephens et al. (2007) revealed that a number of transport models compared in the TransCom-3 study (Gurney et al., 2002) do have vertical mixing biases which were revealed by comparing optimized concentration fields with observed vertical profiles not used in the



inversion. Models with both too steep and too shallow vertical gradients were present. Similarly, Yang et al. (2007) used ground-based FTS and aircraft measurements to suggest that use of CO<sub>2</sub> concentration data in boundary layer in the atmospheric inversions can bias the estimated fluxes, and pointed to a weak vertical mixing bias on average in a number of the transport models of TransCom-3. They implied that the use of CO<sub>2</sub> column data could be more relevant for the reliable optimization of terrestrial ecosystem models. Mean weak mixing bias in TransCom-3 models by (Gurney et al., 2002) can be attributed to using mostly offline models with missing or simplified physical process parameterizations such as shallow and penetrative cloud convection and boundary layer turbulence. Some of more recent transport models, such as compared by Law et al. (2008) involve complete online transport schemes and are expected to do better in vertical mixing.

In the present study, we optimized CASA with partial column data of CO<sub>2</sub> obtained by aircraft measurements, and separately, with near-surface data of CO<sub>2</sub> for comparison. We applied the atmospheric transport inversion method, which is widely used to estimate regional fluxes of CO<sub>2</sub> (e.g. (Gurney et al., 2004)), to estimate two parameters of the CASA flux model (light use efficiency and temperature dependence of the heterotrophic respiration) independently for each of the 11 vegetation types. By analyzing the vertical profiles of simulated and observed CO<sub>2</sub>, it was found that the transport model used in this study has a weak vertical mixing especially in the northern mid latitude during winter and this inaccuracy of the mixing led to the underestimation of NEP seasonality when near-surface data was used exclusively. The optimization with partial column data of CO<sub>2</sub>, on the other hand, is less affected by mixing scheme of a transport model and expected to result in more accurate optimization of seasonal cycles of NEP field.

## 2.2 Methods

In this section, we first present the overall description of the inversion method used for the CASA parameter optimization, followed by the detailed description of each part of the optimization process as well as the models used in this study.

### 2.2.1 Carbon cycle model

We used the Carnegie-Ames-Stanford Approach (CASA) to simulate terrestrial biosphere. Specifically, the CASA described by van der Werf et al. (2003) was used with following modifications. The fire activities in CASA were turned off by setting the burned fraction to zero at every grid cell of CASA for all times. This is because we are only interested in the seasonal cycle of NEP in the present study, and the inter-annual variability of the forest fire activities is too erratic to account for in the average seasonal cycle (van der Werf et al., 2006). As input data for CASA, we used the same dataset as described by van der Werf et al. (2003) except for monthly normalized difference vegetation index (NDVI). We used NDVI data from Pathfinder AVHRR Land dataset (Agbu and James, 1994) for 1981 to 2001, and derived the monthly climatology of NDVI following the method described by Randerson et al. (1997). Figure 2.1 shows the distributions of the vegetation types in CASA as well as the abbreviation for each vegetation type of CASA used throughout the rest of this paper. We used CASA with spatial resolution of 1° latitude × 1° longitude and monthly time step. In the rest of this sub section, the algorithms of CASA used to derive NPP and flux of carbon due to heterotrophic respiration  $R_h$  are briefly introduced since the parameters that control these two quantities were optimized in this study.

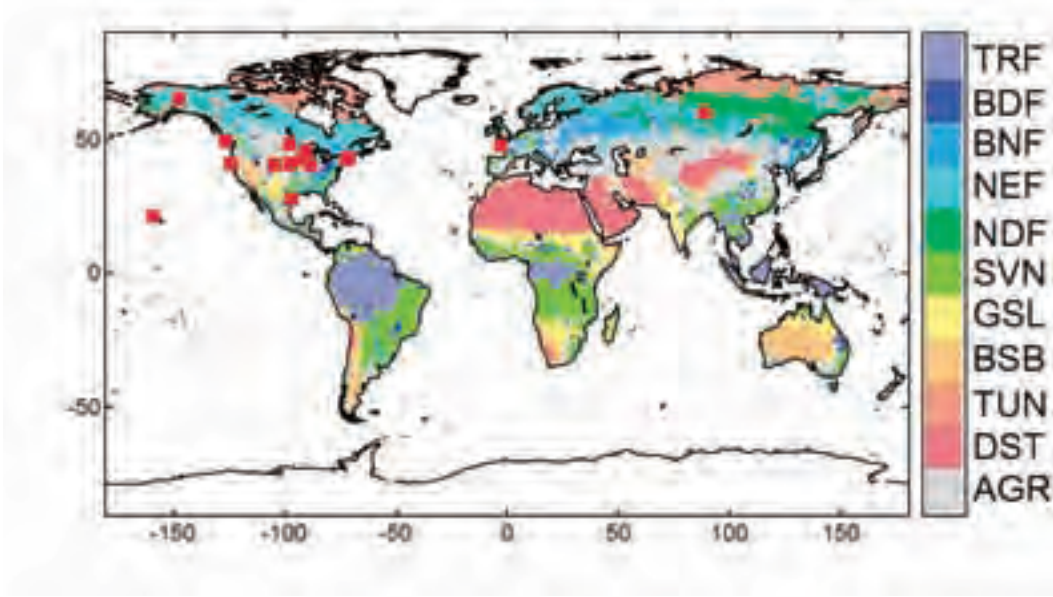


**Figure 2.1 Map of vegetation types in CASA.** TRF: tropical rainforests, BDF: broadleaf deciduous forests; BNF: broadleaf and needleleaf forests; NEF: needleleaf evergreen forests; NDF: needleleaf deciduous forests; SVN: savannas, GSL: perennial grasslands, BSB: broadleaf shrubs with bare soil, TUN: tundra, DST: desert, AGR: agriculture. Red squares on the map indicate the locations of the vertical profile data used for this study (see Table 2.1).

The net ecosystem exchange (NEE) in CASA is obtained as a difference between the net primary productivity (NPP) and the sum of fluxes due to  $R_h$ , fuel wood burnings, and consumptions of plants by herbivores. In CASA, the NPP at a grid cell  $g$  and time  $t$  is given by

$$\text{NPP}(g, t) = \text{IPAR}(g, t) \varepsilon(g, t) \quad (1)$$

where IPAR is intercepted photosynthetically active radiation and  $\varepsilon$  is light use efficiency. The value of IPAR in Eq (6) is a function of NDVI and proportional to photosynthetically active radiation PAR (Bishop and Rossow, 1991). On the other hand,  $\varepsilon$  is a production efficiency of an ecosystem for a given IPAR and is expressed as

$$\varepsilon(g, t) = F_T(g, t) F_W(g, t) E_{\max} \quad (2)$$

where factors  $F_T$  and  $F_W$  are dependent on temperature and soil moisture and account for stresses induced by temperature and soil water availability, respectively, and  $E_{\max}$  is a maximum light use efficiency. To our knowledge,  $E_{\max}$  has been taken as a universal constant common to all ecosystem types in the original CASA (e.g.  $0.5 \text{gC (MJ PAR)}^{-1}$  as used by van der Werf et al. (2003)).

Likewise, conditions of soil moisture and temperature dominate the control over  $R_h$ . The effect of temperature on  $R_h$  is expressed as  $F_R$  which is an exponential function of a factor  $Q_{10}$ :

$$F_R(g, t) = Q_{10}^{\{T(g, t) - 30\}/10} \quad (3)$$

where  $T(g, t)$  is a surface temperature. In this study, we simultaneously optimized  $E_{\max}$  and  $Q_{10}$  of each vegetation type; that is, the size of parameter vector  $\mathbf{p}$  is 22 (i.e. 2 parameters  $\times$  11 vegetation types). Furthermore, we used  $0.5 \text{ gC (MJ PAR)}^{-1}$  and 2.00 as the initial values of

$E_{max}$  and  $Q_{10}$ , respectively, and 0.25 gC (MJ PAR)<sup>-1</sup> and 0.30 as the prior uncertainty of  $E_{max}$  and  $Q_{10}$ , respectively.

### 2.2.2 Formalism of the parameter optimization

In this study, we optimized a set of the CASA parameters,  $\mathbf{p}$ , using the Bayesian inversion in which the weighted mismatches between the modeled and observed concentrations of atmospheric CO<sub>2</sub> concentrations are minimized. This is equivalent to minimizing the cost function  $\mathbf{J}$

$$\mathbf{J} = (\mathbf{x} - \mathbf{M}(\mathbf{p}))^T \mathbf{C}_x^{-1} (\mathbf{x} - \mathbf{M}(\mathbf{p})) + (\mathbf{p} - \mathbf{p}_0)^T \mathbf{C}_{p0}^{-1} (\mathbf{p} - \mathbf{p}_0) \quad (4)$$

where  $\mathbf{x}$  is a matrix consisting of the observed CO<sub>2</sub> concentrations,  $\mathbf{M}$  is a transport model which maps  $\mathbf{p}$  to simulated concentrations of CO<sub>2</sub>,  $\mathbf{p}_0$  is the initial values of  $\mathbf{p}$ , and  $\mathbf{C}_x$  and  $\mathbf{C}_{p0}$  are the covariance matrices of  $\mathbf{x}$  and  $\mathbf{p}_0$ , respectively. The operator  $\mathbf{M}$  consists of atmospheric transport model ( $\mathbf{A}$ ) and CASA ( $\mathbf{B}$ ), i.e.  $\mathbf{M}(\mathbf{p}) = \mathbf{A} \mathbf{B}(\mathbf{p})$ . As shown in the following section,  $\mathbf{B}$  is nonlinear while  $\mathbf{A}$  is linear, so in order to minimize Eq. (4) we expanded  $\mathbf{B}$  around  $\mathbf{p}_0$  in Taylor series and approximated it up to the 1<sup>st</sup>-order term:

$$\mathbf{M} = \mathbf{A}[\mathbf{B}(\mathbf{p}_0) + \mathbf{G}(\mathbf{p} - \mathbf{p}_0)]. \quad (5)$$

where  $\mathbf{G}$  is the first derivative of  $\mathbf{B}(\mathbf{p})$  with respect to  $\mathbf{p}$  at  $\mathbf{p} = \mathbf{p}_0$ . We evaluated  $\mathbf{G}(\mathbf{p} - \mathbf{p}_0)$  numerically assuming a linear relationship between the first derivative and  $\mathbf{p}$  for a small change in  $\mathbf{p}$ . Furthermore, the solutions of  $\mathbf{p}$  which minimizes Eq. (1) is

$$\mathbf{p} = \mathbf{p}_0 + [\mathbf{G}^T \mathbf{C}_x^{-1} \mathbf{G} + \mathbf{C}_{p0}^{-1}]^{-1} \mathbf{G}^T \mathbf{C}_x^{-1} [\mathbf{x} - \mathbf{G} \mathbf{p}_0] \quad (6)$$

and the associated covariance matrix of  $\mathbf{p}$  is

$$\mathbf{C}_p = [\mathbf{C}_{p0}^{-1} + \mathbf{G}^T \mathbf{C}_x^{-1} \mathbf{M}]^{-1}. \quad (7)$$

The detailed derivations of Eqs.(6) and (7) were previously shown, for example, by Enting (2002) and Bousquet et al. (1999). In this study, the minimization of  $\mathbf{J}$  was done iteratively since we used the linear approximation in Eq. (5). Throughout the iterative process, the values of  $\mathbf{p}_0$  and  $\mathbf{C}_{p0}$  were fixed at the values described in the following section. Note that, because Eq. (5) is not exact, neither  $\mathbf{p}$  nor  $\mathbf{C}_p$  obtained by Eqs. (6) and (7) are exact solutions to minimize  $\mathbf{J}$ . Thus, to assign the measure of the improvements in the simulation, we calculated  $\chi^2$  which is the mean-square mismatch between the observed and simulated concentrations:

$$\chi^2 = N_{obs}^{-1} \sum_n^{N_{obs}} (\mathbf{x}_{nn} - (\mathbf{M}(\mathbf{p})_{nn})^T \mathbf{C}_x^{-1} (\mathbf{x}_{nn} - (\mathbf{M}(\mathbf{p})_{nn})) \quad (8)$$

where  $N_{obs}$  is the number of observations (i.e. the size of  $\mathbf{x}$ ), and  $\mathbf{M}(\mathbf{p})$  is in its exact form.

### 2.2.3 Atmospheric transport model

The NIES transport model (Maksyutov and Inoue, 2000) was used to simulate the global distributions of CO<sub>2</sub> resulting from a given surface CO<sub>2</sub> flux. It is an off-line model and uses National Centers for Environmental Prediction (NCEP) reanalysis meteorology (Kalnay et al., 1996). The model has a resolution of 2.5° latitude × 2.5° longitude, 15 vertical levels (from ~0.15 to 20 km in altitude), and the time step of 15 minutes. The advection scheme is semi-Lagrangian with tracer mass adjustment for the conservation of tracer. The monthly climatological day-time mean planetary boundary layer (PBL) height, derived from the GEOS-1 reanalysis (Schubert et al., 1995), was used to define the PBL height in the model.

The detailed description of the model's scheme for vertical mixing can be found in Appendix A of Ishizawa et al. (2006). For this study, the transport model was run for 3 model-years with the meteorology of 1997-1999 and appropriate background fluxes (described below), and the result from the 3<sup>rd</sup> year was used to represent the seasonal cycle of the CO<sub>2</sub> concentration for a given surface flux. Annual anthropogenic carbon fluxes for 1990 (Andres et al., 1996) and 1995 (Brenkert, 1998) and monthly oceanic flux (Takahashi et al., 2002) were used as the background fluxes. The linear trend of the simulated CO<sub>2</sub> concentration at each station was subtracted from each station data to prepare a detrended seasonal cycle at each station. The propagation of response function  $G$  (see Eq. (5)) in the atmosphere was simulated with the NIES transport model and used to evaluate Eqs. (6) and (7).

## 2.2.4 Observed data of CO<sub>2</sub>

We used data of vertical profiles of CO<sub>2</sub> concentration from GLOBALVIEW-CO<sub>2</sub> (2007). The locations of the 15 vertical profiles used in this study are shown in Figure 2.1, and the vertical coverage at each data point is listed in Table 2.1. The error of each seasonal cycle was obtained using the method described by Kaminski et al. (2002). The discrete vertical profiles were converted to a partial column concentration, assuming that the each data point represents a concentration of CO<sub>2</sub> in a column of atmosphere having a thickness of 1000 m centered at the altitude at which the data was taken (see Table 2.1). We used weighted mean of the uncertainty of each data point in the vertical profile to obtain the uncertainty of the partial column concentration. In addition to the dataset of partial column concentrations, the CO<sub>2</sub> concentrations at the lowest level of each vertical profile were collected to prepare the “near-surface” dataset of the CO<sub>2</sub> concentrations.

**Table 2.1 Locations and amplitudes of the CO<sub>2</sub> vertical profile data used for this study.** The data were obtained from GLOBALVIEW-CO<sub>2</sub> (2007).

Code	Descriptive Name	Latitude	Longitude	Altitudes (m)
BNE	Beaver Crossing, Nebraska (USA)	40.80 °	97.10° W	500, 1500, 2500, 3500, 4500, 5500, 6500
CAR	Carr, Colorado (USA)	40.37°	104.30° W	3000, 4000, 5000, 6000, 7000, 8000
DND	Dahlen, North Dakota	48.38°	97.77° W	500, 1500, 2500, 3500, 5000
ESP	Estevan Point, Canada	49.58 °	126.37 ° W	500, 1500, 2500, 3500, 4500, 5500
HAA	Hawaii (USA)	21.23 °	158.95 ° W	500, 1500, 2500, 3500, 4500, 5500, 6500, 7500
HFM	Harvard Forest, Massachusetts (USA)	42.54 °	72.17 ° W	1500, 2500, 3500, 4500, 5500, 3500, 7500
EPT	Estevan Point, Canada	49.38 °	126.55 ° W	500, 1500, 2500, 3500, 4500, 5500
HFM	Harvard Forest, Massachusetts (USA)	42.54 °	72.17 ° W	500, 1500, 2500, 3500, 4500, 5500, 3500, 7500
HIL	Homer, Illinois (USA)	40.07°	87.91 ° W	500, 1500, 2500, 2500, 3500, 4500, 5500
LEF	Park Falls, Wisconsin (USA)	45.93 °	90.27 ° W	500, 1500, 2500, 2500, 3500, 4500, 5500
NHA	Worcester, Massachusetts (USA)	42.95 °	70.63 ° W	500, 1500, 2500, 2500, 3500, 4500, 5500
ORL	Orleans, France	47.80 °	2.50 ° W	500, 1500, 2500, 3500
PFA	Poker Flat, Alaska (USA)	65.07 °	147.29 ° W	1500, 2500, 3500, 4500, 5500, 6500, 7500
RIA	Rowley, Iowa (USA)	42.40 °	91.84 ° W	1000, 3000, 5000, 7000
TGC	Sinton, Texas (USA)	27.73 °	96.86 ° W	50, 1500, 2500, 3500, 4500, 5500, 6500, 7500
THD	Trinidad Head, California (USA)	41.05 °	124.15 ° W	500, 1500, 2500, 3500, 4500, 5500, 6500, 7500
ZOT	Zotino, Russia	60.00°	89.00° E	500, 1500, 2500, 3500

## 2.3 Results and discussions

In this section, we first describe the values of optimized parameters and the changes in their uncertainties. Then, the results of the seasonal cycles obtained from the partial column data and near surface data will be compared from several aspects.

### 2.3.1 Optimized parameters

The values of both  $Q_{10}$  and  $E_{max}$  stabilized after five iterative calculations to minimize Eq. (4) with the observed seasonal cycles of partial column data. However, the values of  $Q_{10}$  and  $E_{max}$  fluctuated quite significantly throughout the optimization with near-surface data. Thus, we chose to use the results which resulted in the smallest value of  $\chi^2$  since we derived  $\chi^2$  without any approximations. We found that the value of  $\chi^2$  decreased from 1.84 to 0.60 after optimization with the partial-column data, while it decreased from 2.60 to 1.67 after optimization with the near-surface data.

The optimization with partial-column data resulted in an average  $E_{max}$  of 0.54 gC (MJ PAR)<sup>-1</sup> and  $Q_{10}$  of 1.81 for 11 vegetation types with standard deviations of  $\pm 0.20$  gC (MJ PAR)<sup>-1</sup> and 0.29, respectively; while the optimization with near-surface data resulted in average  $E_{max}$  of 0.49 gC (MJ PAR)<sup>-1</sup> and  $Q_{10}$  of 1.81 with standard deviations of  $\pm 0.27$  gC (MJ PAR)<sup>-1</sup> and 0.27, respectively. The optimized values of  $E_{max}$  and  $Q_{10}$  for each vegetation type are shown in Figure 2.2. The value of  $E_{max}$  optimized with partial-column CO<sub>2</sub> were greater than or approximately equal to the  $E_{max}$  optimized with the near-surface CO<sub>2</sub> data for all vegetation types except for BNF. Moreover,  $E_{max}$  of BNF was more tightly constrained by the near-surface data than by the partial-column data (Figure 2.3). On the other hand, near-surface and partial-column inversions resulted in the values of  $Q_{10}$  that are significantly different from each other for AGR and NEF, although these two vegetation types had the opposite trends in  $E_{max}$  and  $Q_{10}$  (Figure 2.2). Interestingly, near-surface data of CO<sub>2</sub> used in this study constrained  $E_{max}$  more than partial-column CO<sub>2</sub> data while the trend was vice versa for  $Q_{10}$  of all vegetation types except for AGR (Figure 2.3).

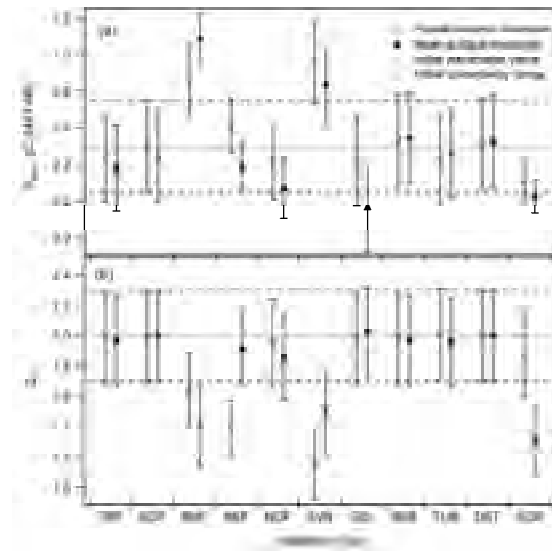


**Figure 2.2 (a)  $E_{max}$  (b)  $Q_{10}$  and of each vegetation type optimized with partial column concentrations of CO<sub>2</sub> and near-surface CO<sub>2</sub> concentration. The dotted and dashed lines represent the initial value and its uncertainty of respective parameter, respectively.**



At the same time, it has to be emphasized that the optimizations of other parameters could have led to the comparable reduction in  $\chi^2$  and thus the physical meanings of the optimized parameters shown in Figure 2.2 need to be carefully interpreted. Moreover, the available data on seasonal cycles of vertical profiles of CO<sub>2</sub> are quite limited at this point, and thus the results of this study are strongly biased toward the location of the available data as shown in Figure 2.3 which shows that some of the vegetation types which have no nearby observation points have no significant reduction in the parameter's uncertainty. Therefore, increasing the number of the reliable vertical profile data is expected to improve the confidence level of the resulting parameters.

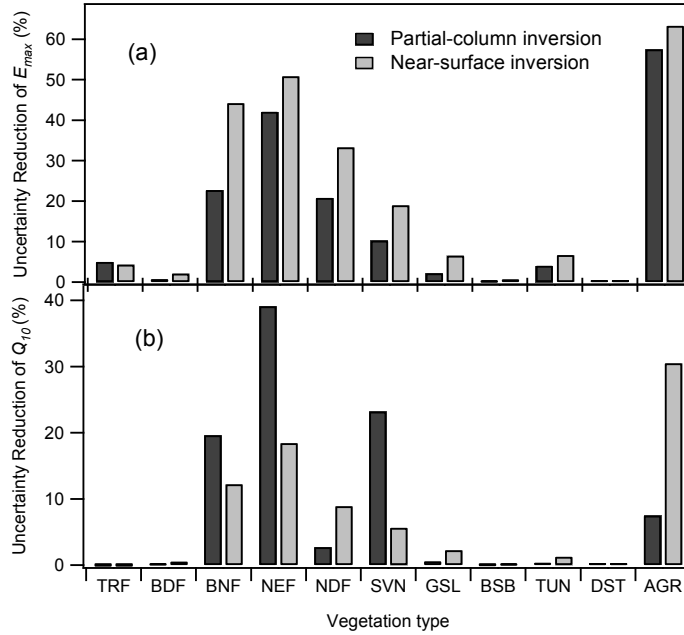


**Figure 2.3** Uncertainty reduction (%) of (a)  $E_{max}$  and (b)  $Q_{10}$ . Note that here, we defined the “uncertainty reduction” as  $\{1 - C_p C_{p0}^{-1}\}$ .

### 2.3.2 Growing season net flux and NPP

To analyze the amplitude of seasonality of NEP of CASA optimized in this study, we calculated growing season net flux (GSNF) which is defined as the sum of NEP for the months when NEP is positive (Randerson et al., 1997). The use of GSNF is valuable in this study since CASA is designed to have no annual net flux (i.e. zero annual NEP) for each model grid, and so we can use GSNF as a measure of the productivity of ecosystem in CASA. The values of GSNF were higher when CASA was optimized with the partial-column CO<sub>2</sub> data than with the near-surface data at almost all latitudes except for around 40° to 45° (Figure 2.4). We compared the values of GSNF and NPP for each vegetation type (Table 2.2), and found that GSNF decreased notably for BNF when we changed the CO<sub>2</sub> data for inversion from the near-surface to partial-column data which account for the low value of GSNF from partial-column inversion between 40° and 45°. Except for BNF, GSNF and NPP of all vegetation types obtained by inversion with the partial column data were either approximately equal to or greater than those obtained with the near-surface data, accumulating to 15.8% and

17.0% increases in the total annual NPP and GSNF, respectively, upon changing the data choice from near-surface to partial column concentrations (Table 2.2). At the same time, Randerson et al. (1997) predicted that the global sums of NPP and GSNF for 1990 were 54.9 PgC y<sup>-1</sup> and 13.6 PgC y<sup>-1</sup>, respectively, and both of these values are slightly larger than corresponding values obtained in this study (see Table 2.2). Correctly identifying the cause of this discrepancy is out of scope of the present study, since the datasets used for CASA in their study are different from those in the present study. Thus, directly comparing the results of these two studies is difficult, and so we limit our discussion to the comparison of our own results in this paper. Furthermore, using column concentrations of CO<sub>2</sub> observed by a ground-based FTS, Yang et al. (2007) found that the actual GSNF north of 30° is approximately 28% larger than the GSNF predicted by Randerson et al. (1997) using CASA. However, in their study, Yang et al. (2007) did not directly evaluate the effects of utilizing column or partial column concentrations of CO<sub>2</sub> instead of boundary concentration data, and so no conclusion was made on how much of this 28% is due to the weak vertical mixing in transport models. In the present study, we can directly compare these two cases. For example, our analysis indicates that the use of near-surface data of CO<sub>2</sub> resulted in GSNF that was 14% less than the case with partial-column data for north of 30°N. At the same time, we note here that this value (14%) can be expected to be slightly larger when total column concentrations (e.g. from ground-based FTS measurements) are used instead of partial columns used in this study.

**Table 2.2 NPP and GSNF of each vegetation type after CASA optimizations with near-surface and partial columns of CO<sub>2</sub>.** The global totals are also shown (note the unit change).

Vegetation type	NPP, gC m <sup>-2</sup> y <sup>-1</sup>		GSNF, gC m <sup>-2</sup> y <sup>-1</sup>	
	Near-surface	Partial-column	Near-surface	Partial-column
TRF	434.4 (±14.7)	492.4 (±14.6)	82.1 (±1.6)	92.2 (±1.6)
BDF	295.9 (±14.7)	332.1 (±14.9)	80.9 (±2.7)	90.7 (±2.7)
BNF	919.9 (±5.9)	728.9 (±8.1)	328.1 (±2.7)	229.6 (±2.24)
NEF	238.2 (±1.9)	378.2 (±2.2)	66.2 (±0.6)	147.6 (±1.0)
NDF	183.8 (±3.5)	278.5 (±4.2)	55.2 (±1.2)	78.1 (±1.4)
SVN	698.5 (±6.7)	802.2 (±7.3)	185.8 (±1.1)	223.3 (±1.2)
GSL	49.3 (±4.9)	126.5 (±5.2)	18.2 (±1.1)	45.9 (±1.1)
BSB	55.4 (±1.5)	54.2 (±1.5)	19.6 (±0.4)	19.2 (±0.4)
TUN	112.3 (±1.5)	103.5 (±1.6)	29.9 (±0.6)	26.8 (±0.6)
DST	5.4 (±0.2)	5.2 (±0.2)	2.2 (±0.1)	2.2 (±0.1)
AGR	108.1 (±1.4)	148.4 (±1.6)	52.7 (±0.5)	54.9 (±0.5)
Global total (PgC y <sup>-1</sup> )	36.7 (±0.6)	42.5 (±0.6)	10.6 (±0.1)	12.4 (±0.1)

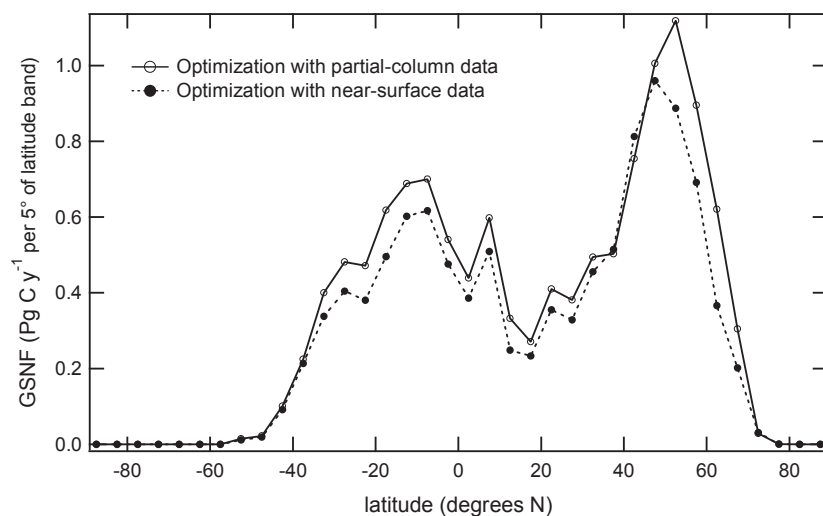


**Figure 2.4** Latitudinal distributions of GSNF obtained with partial-column  $\text{CO}_2$  and near-surface  $\text{CO}_2$ .

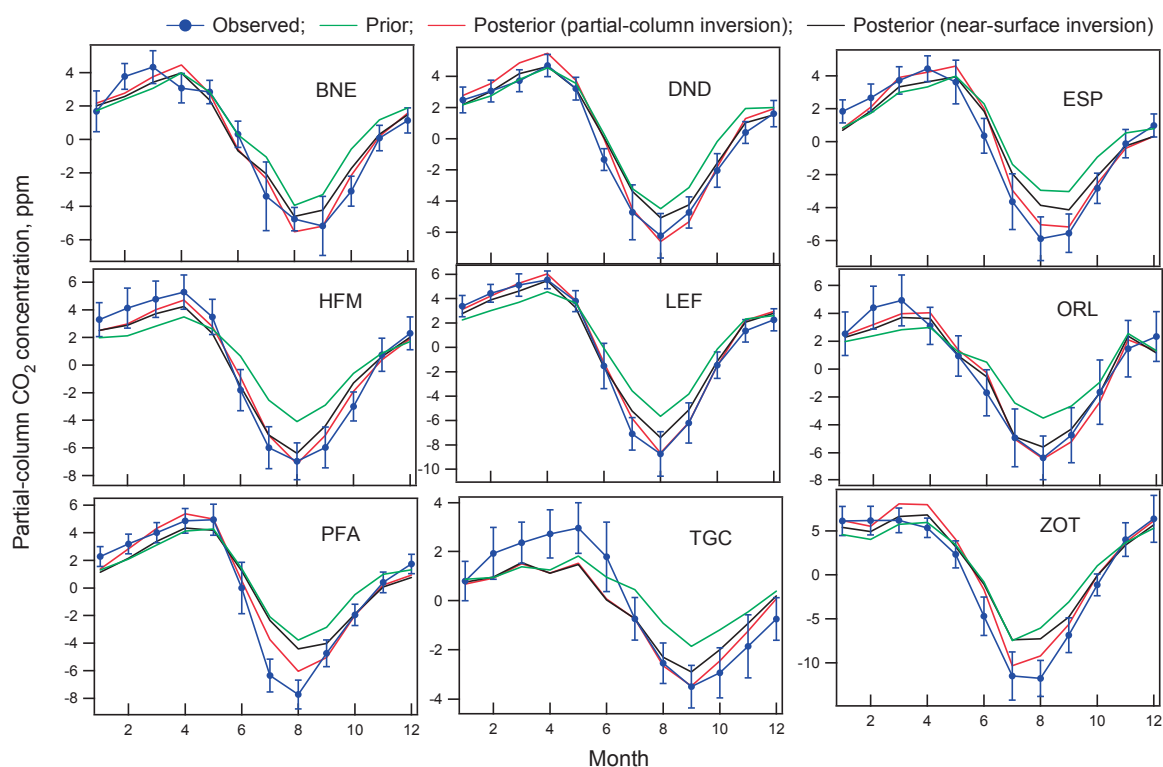


**Figure 2.5** Seasonal cycles of  $\text{CO}_2$  partial column concentrations. Observed values are plotted with the results of 2 cases of CASA optimizations, as well as their prior values.

### 2.3.3 Seasonal cycle and vertical profiles of $\text{CO}_2$ with optimized CASA NEP

Using two sets of optimized  $\text{CO}_2$  flux field from CASA along with background fluxes, we simulated seasonal cycle of global  $\text{CO}_2$  concentration field. Figure 2.5 shows that the



optimized seasonal cycles of partial-column concentrations resulted in the better fits to observations of partial column concentrations than those simulated with prior values of  $E_{max}$  and  $Q_{10}$ , for both cases of optimizations. Furthermore consistent with the trend of GSNF and NPP, the seasonal cycle of CO<sub>2</sub> partial-column concentrations simulated with CASA optimized with near-surface data had a smaller amplitude than those optimized with partial-column data (Figure 2.5; results for only selected locations are shown). We also compared the vertical profiles of the observed and simulated CO<sub>2</sub> concentrations, by averaging vertical profiles for northern hemisphere summer (July, August, and September) and winter (January, February, and March) (Figure 2.6). By comparing the vertical profiles simulated with 2 cases of optimized CASA, we found that the vertical gradients of their CO<sub>2</sub> concentrations are almost identical while the amplitude of seasonal cycle at a given altitude is greater for the CO<sub>2</sub> concentration simulated with CASA optimized with partial column data. On the other hand, for both of these simulated vertical profiles of many locations, the simulated vertical gradients are too strong compared with the observed vertical gradients especially in winter (Figure 2.6). This indicates that the vertical mixings in the transport model at these locations are not sufficient. Moreover, similarly to what was suggested by Yang et al. (2007) for the average of 12 transport models used in TransCom-3, NIES transport model has insufficient rates of vertical mixing both between the planetary boundary layer and upper troposphere (Figure 2.6). This weak vertical mixing in the transport model is attributed as a cause of the GSNF and NPP of CASA that was underestimated when CASA was optimized with the near-surface data. That is, low (in summer) and high (in winter) concentrations of CO<sub>2</sub> in boundary layer, caused by the net flux of CO<sub>2</sub> due to activities of terrestrial ecosystem (i.e. photosynthesis and respiration), are not effectively propagated to the higher altitudes due to the insufficient vertical mixing in the transport model, and this results in artificially high amplitudes of seasonal cycle of CO<sub>2</sub> concentration near surface even when the correct amount of CO<sub>2</sub> flux from CASA is given to a transport model. Thus, when only near-surface data of CO<sub>2</sub> concentrations are used to optimize CASA, the amplitudes of seasonal cycles of NEP in CASA are underestimated. On the other hand, when column concentrations of CO<sub>2</sub> are used, the optimization of CASA is affected less by the inaccuracy of vertical mixing in the transport model and more reliable results can be obtained although other problems in the transport model as well as other parameters of CASA may bias the results. Furthermore, since the method described in this paper can correct the seasonality of CASA NEP without being much affected by a scheme of vertical mixing in a transport model, it can be used to prepare flux fields of CO<sub>2</sub> which can be used as a reference for tuning vertical mixing processes in a transport model, and could be complementary to other widely used vertical mixing tracers such as radon.

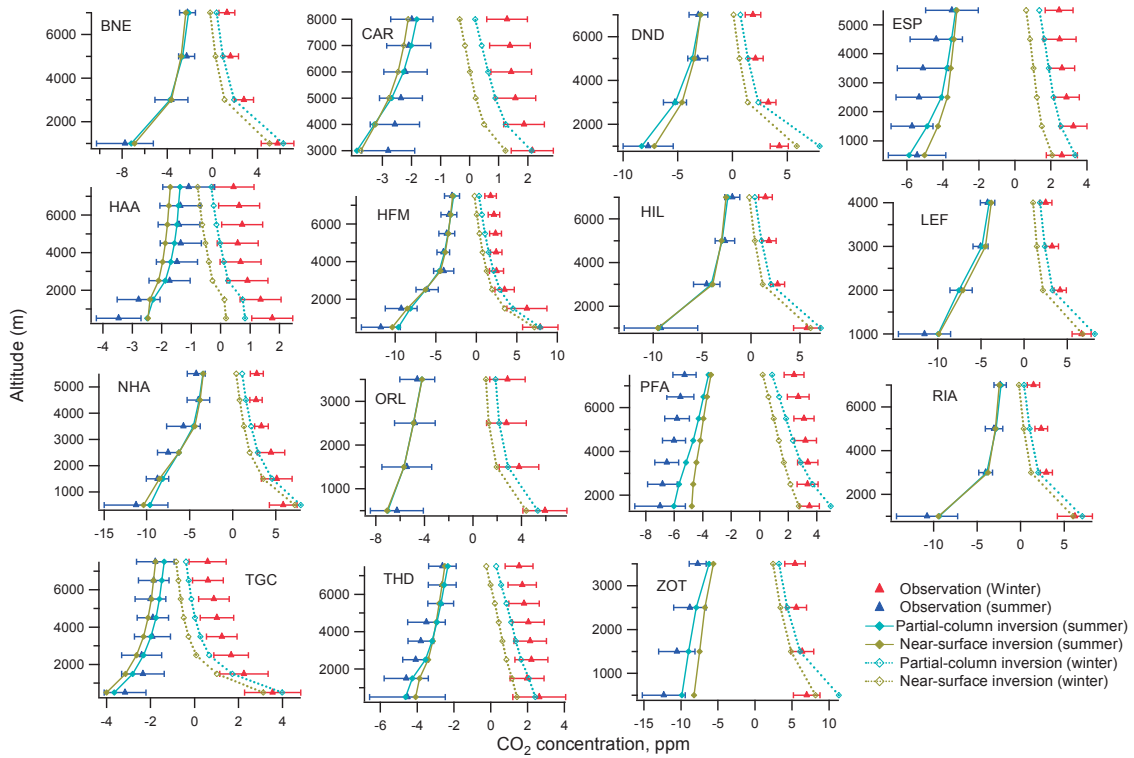


**Figure 2.6 Vertical profiles of the simulated and optimized CO<sub>2</sub> concentrations at each location.** The simulated profiles were made using the CASA parameters obtained with partial column of CO<sub>2</sub> and near surface CO<sub>2</sub> data.

## 2.4 Summary

The seasonality of the CASA ecosystem model was optimized using the vertical profiles of the observed CO<sub>2</sub> concentrations and the inverse of transport model with CASA. We found that the method employed in this study can effectively optimize the seasonality of CASA NEP. Moreover, we found that the CASA NEP simulated with the partial column concentrations of CO<sub>2</sub> has larger seasonal amplitude than that simulated with the near-surface data. Our analysis showed that annual GSNF predicted with the partial column data was 14% larger than that predicted with the near-surface data. Furthermore, the analysis of the vertical profiles showed that the low GSNF predicted with near-surface data is due to the weak vertical mixing in the transport model used in this study. In conclusion, optimization of an ecosystem model for CO<sub>2</sub> flux in conjunction with an atmospheric transport model can be more reliably achieved with CO<sub>2</sub> column concentrations than only with the near-surface data, especially when a vertical mixing scheme in a transport model is not accurate enough. As a result, we arrived at the CO<sub>2</sub> flux model which fits CO<sub>2</sub> column observations better and is less dependent on the mixing properties of the transport model used in the parameter optimization process. Better fit to the partial column average concentration can potentially improve a fit of the forward model simulations to the observations of the CO<sub>2</sub> by ground based and space based remote sensing instruments. Transport model tuning is left beyond a scope of this study because the main purpose of producing correct NEP seasonality is achieved by using partial CO<sub>2</sub> column observations, although it would be even more efficient to simultaneously tune transport and surface fluxes, that would allow including surface-only observation sites data consistently with vertical profiles.

## Acknowledgements

Authors wish to thank Drs. J. T. Randerson and G. van der Werf for generously providing us with the CASA code written in MATLAB and its input data. Additionally, data used by the authors in this study include data produced through funding from Earth Observing System Pathfinder Program of NASA's Mission to Planet Earth in cooperation with National Oceanic and Atmospheric Administration. The data were provided by the Earth Observing System Data and Information System, Distributed Active Archive Center at Goddard Space Flight Center which archives, manages, and distributes this data set. This work was partly supported by the Grants-in-Aid for Creative Scientific Research (2005/17GS0203) of the Ministry of Education, Science, Sports and Culture, Japan, and funding by Global Environment Research Fund of the Ministry of Environment, Japan.

## References

- Agbu, P.A., James, M.E. (1994) The NOAA/NASA Pathfinder AVHRR land data set user's manual. in: Goddard Distributed Active Archive Center, NASA, Goddard Space Flight Center, Greenbelt.
- Andres, R.J., Marland, G., Fung, I., Matthews, E. (1996) A  $1^\circ \times 1^\circ$  distribution of carbon dioxide emissions from fossil fuel consumption and cement manufacture, 1950-1990. *Global Biogeochem. Cy.*, 10(3), 419-429.
- Bishop, J.K.B., Rossow, W.B. (1991) Spatial and temporal variability of global surface solar irradiance. *J. Geophys. Res.*, 96(C9), 16839-16858.
- Bousquet, P., Ciais, P., Peylin, P., Ramonet, M., Monfray, P. (1999) Inverse modeling of annual atmospheric CO<sub>2</sub> sources and sinks 1. Method and control inversion. *J. Geophys. Res.*, 104(D21), 26161-26178.
- Brenkert, A.L. (1998) Carbon dioxide emission estimates from fossil fuel burning, hydraulic cement production, and gas flaring for 1995 on a one degree grid cell basis. Oak Ridge National Laboratory - Carbon Dioxide Information Analysis Center, <http://cdiac.esd.ornl.gov/ndps/ndp058a.html>.
- Cramer, W., Kicklighter, D.W., Bondeau, A., Moore, B., Churkina, C., Nemry, B., Ruimy, A., Schloss, A.L. (1999) Comparing global models of terrestrial net primary productivity (NPP): Overview and key results. *Glob. Change Biol.*, 5, 1-15.
- Enting, I. (2002) Inverse problems in atmospheric constituent transport. Cambridge University Press, Cambridge, U.K.
- Fung, I.Y., Tucker, C.J., Prentice, K.C. (1987) Application of advanced very high-resolution radiometer vegetation index to study atmosphere-biosphere exchange of CO<sub>2</sub>. *J. Geophys. Res.*, 92(D3), 2999-3015.
- GLOBALVIEW-CO<sub>2</sub> (2007) Cooperative atmospheric data integration project - carbon dioxide. in, CD-ROM, NOAA ESRL, Boulder, Colorado [Also available on Internet via anonymous FTP to <ftp.cmdl.noaa.gov>, Path: [ccg/co2/GLOBALVIEW](#)].
- Gurney, K.R., Law, R.M., Denning, A.S., Rayner, P.J., Baker, D., Bousquet, P., Bruhwiler, L., Chen, Y.H., Ciais, P., Fan, S., et al. (2002) Towards robust regional estimates of CO<sub>2</sub> sources and sinks using atmospheric transport models. *Nature*, 415, 626-630.
- Gurney, K.R., Law, R.M., Denning, A.S., Rayner, P.J., Pak, B.C., Baker, D., Bousquet, P., Bruhwiler, L., Chen, Y.H., Ciais, P., et al. (2004) Transcom-3 inversion intercomparison: Model mean results for the estimation of seasonal carbon sources and sinks. *Global Biogeochem. Cy.*, 18, GB1010, doi:10.1029/2003GB002111.
- Ishizawa, M., Chan, D., Higuchi, K., Maksyutov, S., Yuen, C.W., Chen, J., Worthy, D. (2006) Rectifier effect in an atmospheric model with daily biospheric fluxes: Impact on inversion calculation. *Tellus*, 58B, 447-462.

- Kalnay, E., Kanamitsu, M., Kistler, R., Collins, W., Deaven, D., Gandin, L., Iredell, M., Saha, S., White, G., Woollen, J., et al. (1996) The NCEP/NCAR 40-year reanalysis project. *Bull. Amer. Met. Soc.*, 77, 437-471.
- Kaminski, T., Knorr, W., Rayner, P.J., Heimann, M. (2002) Assimilating atmospheric data into a terrestrial biosphere model: A case study of the seasonal cycle. *Global Biogeochem. Cy.*, 16 (4), 1066, doi:10.1029/2001GB001463.
- Law, R., Peters, W., Rödenbeck, C., Aulagnier, C., Baker, I., Bergmann, D.J., Bousquet, P., Brandt, J., Bruhwiler, L., Cameron-Smith, P.J., et al. (2008) Transcom Model simulation of hourly atmospheric CO<sub>2</sub>: experimental overview and diurnal cycle results for 2002. *GBC*, 22, GB3009, doi:10.1029/2007GB003050.
- Maksyutov, S., Inoue, G. (2000) Vertical profiles of radon and CO<sub>2</sub> simulated by the global atmospheric transport model. CGER's supercomputer activity report, CGER NIES, Tsukuba, Japan, 39-41.
- Maksyutov, S., Machida, T., Mukai, H., Patra, P.K., Nakazawa, T., Inoue, G. Transcom-3 Modelers (2003) Effect of recent observations on Asian CO<sub>2</sub> flux estimates by transport model inversions. *Tellus*, 55B, 522-529.
- Randerson, J.T., Thompson, M.V., Conway, T.J., Fung, I.Y., Field, C.B. (1997) The contribution of terrestrial sources and sinks to trends in the seasonal cycle of atmospheric carbon dioxide. *Global Biogeochem. Cy.*, 11, 535-560.
- Randerson, J.T., Collatz, G.J., Fessenden, J.E., Munoz, A.D., Still, C.J., Berry, J.A., Fung, I.Y., Suits, N., Denning, A.S. (2002) A possible global covariance between terrestrial gross primary production and C-13 discrimination: Consequences for the atmospheric C-13 budget and its response to ENSO. *Global Biogeochem. Cy.*, 16(4), 1136, doi:10.1029/2001GB001845.
- Rayner, P.J., Scholze, M., Knorr, W., Kaminski, T., Giering, R., Widmann, H. (2005) Two decades of terrestrial carbon fluxes from a carbon cycle data assimilation system (CCDAS). *Global Biogeochem. Cy.*, 19, GB2026, doi:10.1029/2004GB002254.
- Rödenbeck, C., Houweling, S., Gloor, M., Heimann, M. (2003) CO<sub>2</sub> flux history 1982-2001 inferred from atmospheric data using a global inversion of atmospheric transport. *Atmos. Chem. Phys.*, 3, 1919-1964.
- Schubert, S., Park, C.-K., Wu, C.-Y., Higgins, W., Kondratyeva, Y., Molod, A., Takacs, L., Seablom, M., Rood, R. (1995) A multiyear assimilation with the GEOS-1 system: Overview and results. in: NASA Technical Memorandum 104606, Goddard Space Flight Center, 182.
- Stephens, B.B., Gurney, K.R., Tans, P.P., Sweeney, C., Peters, W., Bruhwiler, L., Ciais, P., Ramonet, M., Bousquet, P., Nakazawa, T., et al. (2007) Weak northern and strong tropical land carbon uptake from vertical profiles of atmospheric CO<sub>2</sub>. *Science*, 316, 1732-1735.
- Takahashi, T., Sutherland, S.C., Sweeney, C., Poisson, A., Metzl, N., Tilbrook, B., Bates, N., Wanninkhof, R., Feely, R.A., Sabine, C., et al. (2002) Global sea-air CO<sub>2</sub> flux based on climatological surface ocean pCO<sub>2</sub>, and seasonal biological and temperature effects. *Deep-Sea Res., Part II*, 49, 1601-1622.
- Tucker, C.J., Fung, I.Y., Keeling, C.D., Gammon, R.H. (1986) Relationship between atmospheric CO<sub>2</sub> variations and a satellite-derived vegetation index. *Nature*, 319, 195-199, doi:10.1038/319195a0.
- van der Werf, G.R., Randerson, J.T., Collatz, G.J., Giglio, L. (2003) Carbon emissions from fires in tropical and subtropical ecosystems. *Glob. Change Biol.*, 9, 547-562.
- van der Werf, G.R., Randerson, J.T., Giglio, L., Collatz, G.J., Kasibhatla, P.S., Arellano, A.F. (2006) Interannual variability in global biomass burning emissions from 1997 to 2004. *Atmos. Chem. Phys.*, 6, 3423-3441.
- Yang, Z., Washenfelder, R.A., Keppel-Aleks, G., Krakauer, N.Y., Randerson, J.T., Tans, P.P., Sweeney, C., Wennberg, P.O. (2007) New constraints on northern hemisphere growing season net flux. *Geophys. Res. Lett.*, 34, L12807, doi:10.1029/2007GL029742.



## **Chapter 3**

### **Design, simulation and validation of an ocean carbon cycle system using an offline Ocean Tracer Transport Model (OTTM)**

Vinu Valsala<sup>1\*</sup>, Shamil Maksyutov<sup>1</sup>, and Motoyoshi Ikeda<sup>2</sup>

1. Center for global Environmental Research, National Institute for Environmental Studies, Tsukuba, Ibaraki 305-8506, Japan
2. Graduate School of Earth System Sciences, Hokkaido University, Sapporo 060-0810, Japan

\*Corresponding author: Dr. Vinu Valsala, Center for Global Environmental Research, National Institute for Environmental Studies, 16-2 Onogawa Tsukuba Ibaraki 305-8506, Japan. E-mail: [vinu.valsala@nies.go.jp](mailto:vinu.valsala@nies.go.jp)

## Abstract

This paper describes the design and implementation of an ocean carbon cycle modeling system that uses an offline ocean tracer transport model. The offline ocean tracer transport model was devised and applied to simulating a conservative tracer, and the results obtained were validated. This model is coupled to a simple biogeochemical model. Air-sea CO<sub>2</sub> fluxes were simulated. The first two sections of this chapter were reproduced from Valsala et al. (2008) with permission, and the third section describes the coupling of the simple biogeochemical model to the ocean tracer transport model.

***Keywords:*** *Transport models, Offline models, OTTM, Ocean biogeochemistry, pCO<sub>2</sub> modeling, Air-sea CO<sub>2</sub> flux modeling*

### 3.1 Design of an offline Ocean Tracer Transport Model (OTTM)

#### 3.1.1 Motivation for OTTM development

The ocean tracer transports are an order of magnitude slower than that of atmospheric transports. It requires relatively longer runs to investigate the life cycle of trace materials in oceans such as chlorofluorocarbon (CFC) or dissolved inorganic carbon (DIC). A typical example of such a slow transport is an intrusion of anthropogenic atmospheric CO<sub>2</sub> in the ocean. Observations show that anthropogenic CO<sub>2</sub> is intruded as deep as 3000 m in the North Atlantic, to date, and this is the deepest penetration of postindustrial CO<sub>2</sub> perturbations in the world's oceans (see Key et al., 2004 for the first climatological maps of carbonaceous tracers in the World Ocean). Simulation of such a slow transport needs thousands of years of model runs, preferably on eddy-resolving configurations, which is still a difficult task for many modeling groups. In this aspect, an offline transport simulation is always preferred.

An offline transport model makes use of precalculated three-dimensional model transport vectors, mixing coefficients, and diffusion tensors from an online run, which is recorded at a regular interval of time. Here, the word offline means that we do not model the ocean currents or stratification explicitly. Instead, they are borrowed from some other model outputs (say, from a reanalysis product), which we refer to as “online data.” These online variables are archived and interpolated into an adequate time step to evolve the prognostic passive tracer. The advantages of solving passive tracers in this manner are manifold. The numerical stability constraints for the momentum equation solving [e.g., Courant-Friedrichs-Lewy (CFL) limits] can be relaxed in an offline passive tracer simulation because oceanic velocities are an order of magnitude smaller than the wave speed (here, concern is given to internal modes resolved in the numerical solutions for momentum equations) associated with the momentum evolution. Therefore, model time steps can be increased and computational time can be saved efficiently. With the advantage of saving computational time, the offline models can thus be more focused on higher-resolution configurations. High resolution is necessary to account for the subgrid-scale transport of the passive tracers. The candidate models of the Ocean Carbon-Cycle Model Intercomparison Project Phase-2 (OCMIP-2) have shown a value range of  $\pm 30\%$  from the mean oceanic uptake of CFC-11, and such large discrepancies among models are mainly associated with their inadequate resolution to resolve the subgrid-scale processes realistically (Dutay et al., 2002). Thus, by using an offline transport model at a high resolution, there is a possibility to improve the predictions of oceanic uptake of anthropogenic chemicals.

A passive tracer, such as the CFC-11 or bomb C-14, does not affect the ocean dynamics, unlike temperature or salinity; thus, a full online simulation by solving all dynamical equations is not a strict constraint for passive tracer evolution. A counter argument may be that tracers such as anthropogenic CO<sub>2</sub> may affect the dynamics because of their coupling with biogeochemical loops, and an offline model cannot be a suitable candidate for research on a carbon cycle in the ocean (the biological production may affect the light penetration in the surface layers, which potentially could alter the dynamics). However, anthropogenic CO<sub>2</sub> can still be treated as “inactive” to the ocean dynamics, arguably, by assuming that a natural balance exists between ocean biology and natural CO<sub>2</sub> in the ocean (Mikaloff Fletcher et al., 2006).

Another advantage of offline models is that they can be used with transport vectors of different online simulations. For example, the assimilated ocean currents that have recently become available from different modeling groups facilitate us finding more reliable passive



tracer transports compared to their online simulations. In addition, such offline transport models can be effectively used to find the adjoint of a forward simulation (Hourdin and Talagrand 2002; Hourdin et al., 2002). This adjoint calculation is useful to track the water masses in the reverse direction in the Eulerian frame, as is being done in the Lagrangian backward trajectories (Valsala and Ikeda, 2007). In this aspect, the offline models can be used to find the reverse pathways of a passive tracer by flipping the sign of precalculated three-dimensional velocities (i.e., eastward velocity is changed to westward velocity of the same magnitude and runs the offline model backward from the end point of archived online circulation), assuming that the influence of mixing, which is of course an irreversible mechanism, is less sensitive in the study concerned (see, e.g., Fukumori et al., 2004).

In addition to the abovementioned uses, the transport model becomes trivial when it comes to the inverse estimate of CO<sub>2</sub> fluxes from DIC inventories (Mikaloff Fletcher et al., 2006, 2007). This method is commonly used in the atmosphere. The method is to find the CO<sub>2</sub> fluxes using Gaussian-basis functions derived from a transport model in its response to a surface dye injection from discrete regions. Later, each transport function from each injection will be fitted to observations of DIC (after removing its “biological component”) in a least square sense with a Bayesian inversion technique (Enting, 2002). This new method of ocean inversion is promising in its ability to give a reliable CO<sub>2</sub> estimation compared to that of the atmospheric inversions, because DIC varies slowly in the ocean, and thus the observations of several years can be squeezed together to obtain data-covariance matrices for Bayesian inversions (Gloor et al., 2003; Mikaloff Fletcher et al., 2006, 2007). Moreover, DIC observations are a thousand times larger in number than those of atmospheric CO<sub>2</sub> observations, which facilitate to minimize the mismatch between observations and transport calculations. Thus, developing an offline transport model is timely and can serve several purposes.

There are additional offline tracer transport models other than the conventional online simulations. For example, Khatiwala et al. (2005) and Khatiwala (2007) have proposed a novel strategy for efficient simulation of geochemical tracers in ocean models. The essence of their approach is the utilization of the property that the discretized advection–diffusion equation of a tracer can be written as a linear matrix equation, which yields a “transport matrix” that contains results from the discretization of the advection–diffusion operators including the effects of various subgrid-scale processes. The decoupling of the transport matrix from the source term makes this approach flexible to any ocean general circulation model (OGCM). In this method, however, the transport matrix is obtained using an OGCM forced by surface fluxes and boundary conditions. On the other hand, our approach utilizes the accuracy present in the assimilated ocean currents to estimate the tracer transport, and the method is still flexible to a family of input products because of the diagnostic mixing and subgrid-scale processes incorporated into the model.

Offline simulation of tracer transports is often practiced with OGCM outputs such as circulation and mixing coefficients. For example, a coupled offline transport and biogeochemistry model was used by McKinley et al. (2004) to simulate the interannual variability of air-sea CO<sub>2</sub> flux in the Pacific. The accuracy of such simulations is largely dependent on the circulation and mixing coefficients that are borrowed from the parent models. On the other hand, our model depends on assimilated ocean currents, which we will show to be efficient. In addition, the diagnostics for mixing and other subgrid-scale processes make this model flexible to a family of input assimilated ocean currents. Gupta and England (2004) have also developed a similar offline model with input data derived from the Parallel

Ocean Climate Model (POCM\_4C). A detailed comparison of this model with our model will be given in the next section.

This article describes the design and validation experiments of an offline tracer transport model. In this version of model, the tracer is assumed as conservative in the ocean as is the case for CFC or anthropogenic CO<sub>2</sub>. The design philosophy is described in the following two sections. A validation is done by simulating the CFC-11 cycle in the oceans, and results are described in section 3.3.

### 3.1.2 Design

In this section, we will see the basic structure of the model, such as its numerical discretization, diagnostic-mode parameterizations, and parallel implementation on the computer. The data inputs used in this study are described in section 3.3. Later, we will use this model to simulate the CFC-11 cycle in the ocean. The evolution of any conservative tracer concentration  $C$  can be written as

$$\partial C / \partial t + \mathbf{U} \cdot \nabla_H C + W \partial C / \partial z = \partial / \partial z K_z \partial / \partial z C + \nabla_H \cdot (K_h \nabla_H C) + \phi \quad (1)$$

where  $\nabla_H$  is the horizontal gradient operator,  $\mathbf{U}$  is the horizontal velocity,  $W$  is the vertical velocity,  $K_z$  is the vertical mixing coefficient, and  $K_h$  is the two-dimensional diffusion tensor. A term  $\phi$  is added to the RHS of Eq. (1) to represent any sink or source, which can be interpreted as internal consumption or production of the tracer as well as the surface intake and efflux. However, this version of the model deals with passive conservative tracers, and thus any internal production or consumption is inhibited with only one source term for the surface fluxes.

In this version of the model, we parameterize the vertical mixing and horizontal diffusion completely from the offline transport vectors (i.e., three-dimensional circulation), temperature ( $T$ ), and salinity ( $S$ ). We chose this parameterization because the offline fields are mostly available as circulation and hydrography; mixing or diffusion coefficients are seldom available. In most of the offline tracer experiments, the coefficients of subgrid-scale mixing and diffusion are borrowed from the parent online runs instead of estimating them from offline fields. However, a general tool such as our model, which is flexible to any online field irrespective of its sources, is desirable to devise self-operating routines for subgrid-scale parameterization. From a physical point of view, this attempt is justifiable because passive tracers seldom affect the dynamics or stability of the ocean (see section 3.1). Thus, borrowing these coefficients from an online archive or recalculating afterward within the offline runs does not make any physical difference. However, a more serious consideration should be given to the frequency of updating the online fields in the offline runs (i.e., time interval of archived offline fields), which is critical in eddy-induced tracer transports, unless they are parameterized explicitly.

#### 3.1.2a Vertical mixing

We have opted for a  $K$ -profile parameterization (KPP; see Large et al., 1994) for the vertical mixing after a selection carried out over a number of several other schemes, which are normally practiced in ocean modeling. In particular, we have tested the second-order level-2 turbulent closure schemes (Mellor and Yamada, 1982) and the more simple slab mixed-layer schemes in our offline model. We found that the KPP yields the most reasonable simulation

compared to the other schemes. In KPP, the vertical mixing is resolved by generating a nonlocal  $k$  profile, which falls within the mixed layer and yields a depth-dependent mixing coefficient ( $K_x$ ), as follows:

$$K_x(\sigma) = h w_x(\sigma) G(\sigma) \quad (2)$$

where  $(\sigma = d/h)$  is the scaling of depth within the mixed layer ( $h$ ) whose value ranges from zero at the surface to one at the bottom of the mixed layer. Here,  $G(\sigma)$  is a cubic polynomial shape function:

$$G(\sigma) = a_0 + a_1\sigma + a_2\sigma^2 + a_3\sigma^3 \quad (3)$$

where  $a_0$ ,  $a_1$ ,  $a_2$ , and  $a_3$  are the coefficients that control the diffusivities and their derivatives at both the top and the bottom of the mixed layer. The values for these coefficients are chosen from Large et al. (1994). In a stable condition, the turbulent velocity scale  $w_x$  in Eq. (2) has two key forms:

$$w_x = k(a_x u^{*3} + c_x k \sigma w^{*3})^{1/3} \quad \text{if } \sigma < \varepsilon \quad (4)$$

$$w_x = k(a_x u^{*3} + c_x k \sigma w^{*3})^{1/3} \quad \text{if } \varepsilon \leq \sigma < 1 \quad (5)$$

The  $\varepsilon$  is the nondimensional extent of the surface layer, which we have chosen to be  $\varepsilon = 0.1$  as in Large et al. (1994). The  $\kappa$  is the von Kármán's constant (0.40). The  $a_x$  and  $c_x$  are the coefficients of nondimensional flux profiles for the tracers whose values are chosen as  $a_x = -28.86$  and  $c_x = 98.96$ . The turbulent friction velocity ( $u^*$ ) and convective velocity ( $w^*$ ) are produced by surface momentum flux (wind stress) and heat flux, respectively, for which we have used the monthly climatological values derived from Hellerman and Rosenstein (1983) and Josey et al. (1999). Below the mixed layer, the vertical convection is controlled by three processes: vertical shear, internal wave breaking, and double diffusion. These are defined from Large et al. (1994).

In addition to the KPP, we have provided a depth-dependent, background vertical diffusion as suggested in Bryan and Lewis (1979; hereafter BL79). This varies from  $0.3 \times 10^{-4} \text{ m}^2 \text{ s}^{-1}$  in the upper ocean to  $1.3 \times 10^{-4} \text{ m}^2 \text{ s}^{-1}$  at depth. This is to compensate for any loss of sporadic convection, especially outside the mixed layer, which cannot be accounted for by a coarse temporal resolution of offline archives.

There are several reasons that can be given as to why the offline fields fail to parameterize a reasonable amount of mixing with schemes that generally perform appreciably well in the online runs. In the offline runs, the frequency of data feeding into the model is crucial. For example, the sporadic convections and mixing that occur on time scales of a few days, or even a subinertial period, may be missing by the time the offline fields are incorporated into the model. Most often, the reanalysis products or some control runs from other modeling groups are available on monthly scales. Any subsampling below monthly (e.g., daily or hourly) fields needs an enormous amount of data storage for the simulation carried on global scales in fine resolution (e.g., studies like the CFC or DIC cycle in the ocean). In addition, the unpacking of such a huge offline data storage affects the computational speed of the integration, and thus the offline models will be losing computational time, resulting in any practical gain over online models.

An optimum choice for parameterization of vertical mixing needs to be devised before applying the model to a particular application. Thus, our approach has two parts: (i) first, an optimal configuration with KPP + BL79 is found to yield a realistic performance, and then (ii)

we map the offline mixed layer depth (MLD) from the parent model, and KPP profiling is carried within it instead of estimating our own mixed layer depth. The main cause for this adaptation is so that we can use the maximum amount of information provided by the assimilated ocean offline data field. This parameterization is, however, to some extent equivalent to adopting a spatially varying “slab mixed layer.” But our choice is more realistic because it accounts for a variable mixing within the mixed layer. The material properties in the ocean are found stratified within the mixed layer, whose parameterization is the essence of KPP. In addition, there is a possibility of improving the below mixed layer ventilation process in the model by taking advantage of a high vertical resolution in the surface layers and a variable vertical mixing profile.

### 3.1.2b Horizontal mixing

The  $K_h$  and  $K_z$  collectively represent the three-dimensional tensor. The diffusion tensor incorporates diffusion fluxes rotated tangential to the local isopycnals, the so-called isopycnal diffusion, an important process for ocean ventilation in the high latitude. A tracer in the ocean mixes mainly along the isopycnals rather than across the isopycnal (i.e., diapycnal). Redi (1982) rotated the diapycnal diffusion fluxes tangential to the local density gradient and achieved advancement in ocean tracer diffusion modeling. However, the Redi fluxes will be zero in the case of density evolution. In a Boussinesq ocean, the divergence of density due to mean currents is locally balanced by the divergence due to the eddy-induced currents. Thus, in noneddy-resolving models (i.e., a coarse-resolution model), eddy-induced divergence of density should be parameterized to cascade the tracer variance from mean transport to a turbulent transport as in reality. In Gent and McWilliams (1990), the eddy-induced “bolus” velocities are shown equivalent to layer thickness diffusion appearing as an eddy-induced advection and are added to the mean advection fluxes. Thus, by combining the Redi fluxes and GM fluxes, a realistic tracer mixing is achieved in present-day OGCMs (Pacanowski and Griffies, 1999). In our version of the offline model, we incorporate both Redi fluxes and GM fluxes in the tracer equation, as follows:

$$\frac{\partial C}{\partial t} + \mathbf{U} \cdot \nabla C + \nabla_z \cdot [C \partial / \partial z (K_h \nabla_z \rho / \rho_z)] - \partial / \partial z [C \nabla_z \cdot (K_h \nabla_z \rho / \rho_z)] = R(C) + (\text{other terms}) \quad (6)$$

where  $\rho$  is the isopycnal surface, with its prefix meaning its gradient, and  $R(C)$  is the isopycnal Redi fluxes (Redi, 1982). The “other terms” stand for the vertical mixing and horizontal diffusion as given in Eq. (1). This is a reasonable alternative for coarse-resolution models to mimic eddy-induced mass convergence (Pacanowski and Griffies, 1999). Although the eddy-induced transport can be an unnecessary addition to fine-resolution models, we incorporated it in our model because it can be used with different offline fields, which come in various resolutions. The contribution of GM fluxes to total transport fluxes will be feeble in fine-resolution cases because the difference in the slope of the density surface between adjacent grids becomes negligible as the resolution becomes finer; thus, it seldom overestimates the advective fluxes. Instead, its contribution becomes significant in coarse-resolution cases where it accounts for the loss of turbulent cascading of tracer variances in the form of eddy-induced transports.

Apart from the isopycnal mixing (Redi, 1982), a weak Laplacian diffusion is provided to give computational stability where a sharp concentration gradient occurs. The effect of this Laplacian diffusion is minimal because such lateral diffusion results in unrealistic mixing and smeared ventilations (Dutay et al., 2002). The coefficient for Laplacian mixing is taken as a

function of latitude ( $\theta$ ) as  $Ah_{(\theta)} = Ah_{\text{back}} \cos(\theta)^{1/5}$ , in which  $Ah_{\text{back}}$  is set at  $5.0 \times 10^2 \text{ m}^2 \text{ s}^{-1}$ . This yields a diffusion coefficient tapered to a minimum value of  $20 \text{ m}^2 \text{ s}^{-1}$  at the polar region in the converging meridian.

### 3.1.2c Grids

The offline model takes the velocity fields and stratification from a precalculated archive. Thus, the grid design depends on the parent model from which the offline fields are borrowed. In most of the general circulation models, the volume is conserved in every grid cell locally because water is incompressible (a Boussinesq approximation is made) and velocities can be interpolated into the desired grid; thus, the choice of grid becomes nonmandatory. However, this assumption is not applicable in a nonrigid lid model in which surface volume is changing with rainfall and evaporation. In this article, we describe the model in a B-grid structure, as done in the parent online model, in which the velocities are at the corners of the tracer grids. The tracer Eq. (1) is solved using the flux form, where the velocities at the cell faces are multiplied by the tracers at the same location and are found to be a gradient of the fluxes. This guarantees the conservation of tracer in the incompressible Boussinesq ocean (S. M. Griffies 2006, personal communication).

The horizontal grids are designed in a spherical coordinate, and vertical grids are  $z$  level as in the parent model. In the spherical coordinate, the longitudinal grid cells converge as they reach the poles, and to attain stability with a uniform time step everywhere in the domain, the high-frequency fluctuations due to numerical instabilities are filtered on every time step in the northern latitude (i.e., poleward of  $80^\circ\text{N}$ ) using a Fourier filter (Pacanowski and Griffies, 1999). However, in this study, the model domain is limited to  $80^\circ\text{N}$  so that poleward filtering is not effective in the results shown here.

A centered-in-space and centered-in-time (CSCT) time-space finite difference scheme is adopted. We prefer this scheme mainly because the offline transport vectors used in this study are configured in CSCT. Although it is possible to attain mass conservation in a different finite difference form than the parent model, we opt for CSCT because it gives second-order accuracy compared to several upstream with first-order accuracy. Hecht et al. (1995) have compared the passive tracer simulation of the CSCT scheme with several upstream schemes and found that for any given magnitude of circulation, the resolutions of the grids are more crucial than a preference on particular finite difference schemes.

The numerical diffusion in CSCT (i.e., the artificial diffusion due to the limitation of finite difference) damps the solutions, especially at a high wavenumber, while the low wavenumbers are unaffected (Kantha and Clayson, 2000). This may have an impact on eddy-induced tracer transport, especially in the western boundary current regions such as the Kuroshio, Gulf stream, and Agulhas. An Asselin–Robert filter (Asselin, 1972) is applied to regulate any ripples in the CSCT scheme with a coefficient of  $\alpha = 0.1$ , and all diffusion tensors are calculated at one time step behind advection. At the land boundaries, no-normal flux is applied. On the surface, the tracer flux enters or leaves the models' surface level [see Eq. (1)]. The model is solved in explicit time stepping, except for the vertical mixing, which is solved implicitly using matrix inversion by LU decomposition (Kantha and Clayson, 2000). The vertical mixing solution cannot be integrated forward explicitly with a large diffusion coefficient demanded by the offline fields (artificial exaggeration of coefficients to account for loss of convections in a smoothed monthly offline fields by adopting a KPP + BL79



scheme; see section 3.1.2a). In addition, the implicit vertical mixing is unconditionally stable and it can adopt a large time step even in a very fine vertical resolution.

A similar offline ocean model with high resolution has recently been developed at the University of New South Wales, Australia, by Gupta and England (2004), and it has achieved a remarkable improvement on CFC-11 simulation over the coarse-resolution OCMIP-2 candidate models. Our model, although in many ways similar to their model, has a major difference in the vertical mixing parameterization. In the Gupta and England (2004) model, a direct implementation of mixed layer depth is used, which they obtained from the density criteria into the tracer evolution. However, our model depends on the physical mechanism to find the vertical mixing, which is still possible to extract from the offline fields, and is parameterized using KPP. We found that with a high vertical resolution [we use 50 levels, which is double the number of levels of Gupta and England (2004)], vertical mixing can still be resolved from the offline fields. We have tested our KPP scheme in a very coarse vertical resolution case (18 vertical levels) and found that KPP performance is not appreciable. Furthermore, their model does not parameterize the isopycnal mixing and GM eddy-induced transport because of the high resolution they use. However, our model also incorporates these schemes that make the model flexible for very fine to moderate coarse-resolution cases.

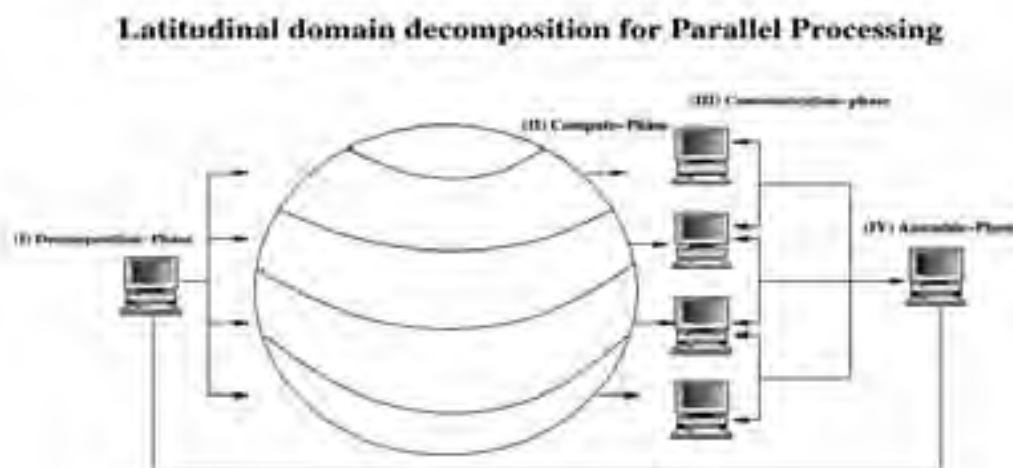


**Figure 3.1 A schematic presentation of the model domain decomposition.** The master node splits the model domain into approximately equal latitudinal strips and assigns to each compute node. The MPI phase communicates the boundary values across the neighboring nodes. The assemble phase combines the output from each nodes and write to the disk.

### 3.1.3 Numerical implementation

The model is written in FORTRAN-77 with a parallel implementation using Message Passing Interface (MPI) protocols. The model possesses a modular structure with each parameterization linked as “ifdef-endif” preprocessor which can be controlled externally using a Makefile. The model can be compiled in either Intel parallel compiler (mpif90) or Portland Group Compiler (pgf90).

Figure 3.1 shows how the model domain is split for the parallel computation. The entire globe is divided into latitudinal strips and each computer node will be assigned to each strip of the globe. The boundary values between two consecutive strips are shared as shown in

Figure 3.2. The size of the memory window sharing at the strip boundaries are 2 and 4 for the Laplacian and biharmonic tracer diffusion, respectively.

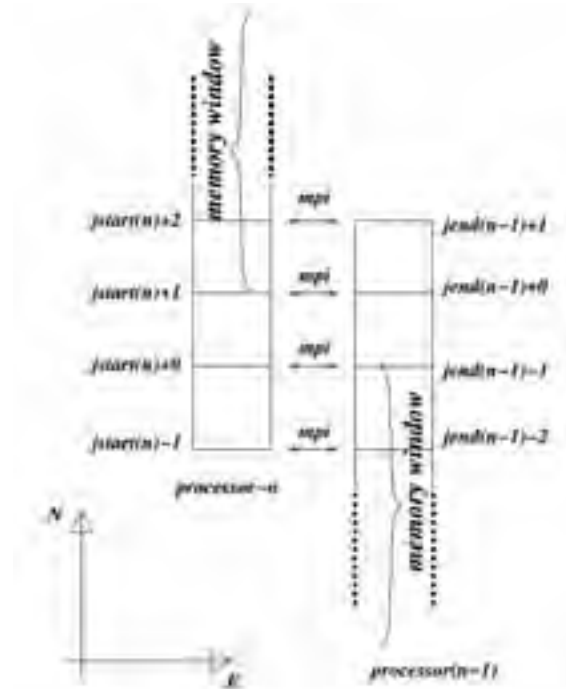


Figure 3.2 Memory window sharing at strip boundaries. Three memory windows are shared.



Figure 3.3 The model flow chart showing the sequence of operations in OTTM.

Figure 3.3 shows the model flow chart. The model starts with invoking the parallel environment needed for the MPI parallel computation. The model possesses a common array of global circulation and other parameters which contain all the offline data accessible for all

the computer nodes. However, the offline archive is interpolated into the model time steps only for necessary partitions of the array within each processor. At each integration time step, the data is interpolated into the model time step within each processor. The model is flexible in choosing independent time steps for the data update from the offline archive and model integration using a time split method. In the present version of the model, monthly archives of the offline data are used and they are interpolated into one-day time steps. The time-split method will operate the integration in every two hours.

## 3.2 Validation of OTTM with CFC-11 simulations

### 3.2.1. Data and model experiments

We use the flow vectors and stratification (i.e., temperature and salinity) derived from the ocean assimilation product of the Geophysical Fluid Dynamics Laboratory (GFDL). The model configuration of assimilated products contains the Modular Ocean Model-4 (MOM4-SIS) ocean–ice component coupled to the Climate Model (CM2.1) with assimilation of in situ temperature profiles from the National Oceanographic Data Center (NODC) archives using a 3D variational scheme. (The data is obtained from <http://data1.gfdl.noaa.gov/nomads/forms/assimilation.html>.) This dataset has a resolution of  $1^\circ$  zonally, with 360 grid points. Latitudinal resolution is  $1^\circ$  at the poles, with a high resolution ( $0.8^\circ$ ) in the tropics containing a total of 200 grid points. With this horizontal resolution, the input solutions do not resolve mesoscale features explicitly, and hence we parameterized it in our offline model. The model contains 50 vertical levels with a 10-m resolution in the upper 225 m and stretched vertical intervals below the depth by including 30 levels in the upper 500 m. With this high vertical resolution, the entrainment and vertical velocities might be resolved explicitly in the data, while vertical mixing has to be parameterized. The mixed layer depth is borrowed from the same assimilation data. The assimilated currents, stratification, and mixed layer depth are obtained for 15 yr. A monthly average value from the 15 yr is constructed. For the atmospheric forcing, wind stress from Hellerman and Rosenstein (1983) and surface heat flux from Josey et al. (1999; both are monthly climatology) are used. Note that these surface boundary conditions are used only to parameterize the vertical mixing in the model, and the same boundary condition as that in OCMIP-2 experiments is used to force the CFC-11 in the surface (see Dutay et al. 2002 for OCMIP-2 CFC-11 surface flux protocols). The model is then used for the following set of experiments and run in parallel across 32 vector processors using the Message Passing Interface (MPI) communication protocols.

CFC-11 and CFC-12 are anthropogenic carbonaceous substances emitted to the atmosphere by increased human activity since the Industrial Revolution during the early twentieth century (Dutay et al., 2002). Although the atmospheric concentration of CFC-11 is increasing exponentially, only 30% remains there and the rest is absorbed by the ocean and transported downwards. The CFC-11 enters the ocean mainly at high latitudes where large-scale oceanic sinks are located because of the ocean ventilation processes. To find the air–sea exchange of this atmospheric CFC-11, we need information on the partial pressure difference between CFC-11 in the ocean surface and the immediate atmosphere.

The model is forced with a surface concentration of CFC-11 in the atmosphere provided by OCMIP-2 flux protocol. The surface CFC-11 flux is calculated as  $F = K_w(C_{\text{sat}} - C_{\text{surf}})$ , where the  $K_w$  is the piston velocity ( $\text{m s}^{-1}$ ) with which the CFC is injected into the ocean,



depending on the wind variance and sea surface temperature. The  $C_{\text{sat}}$  ( $\text{mol m}^{-3}$ ) is the saturation level of CFC in the surface of the ocean, which depends on the atmospheric pressure, solubility for water vapor saturated air, and partial pressure of CFC in dry air at one atmosphere total pressure. The  $C_{\text{surf}}$  ( $\text{mol m}^{-3}$ ) is the model surface concentration of CFC-11. This is the standard OCMIP-2 flux protocol for the CFC calculation, and we kept the same forcing as that of candidate models that participated in OCMIP-2 (Dutay et al., 2002). This facilitates the direct comparison of our results with other candidate models of OCMIP-2. The model starts with initial zero concentration of CFC-11 and is integrated from 1938 to 1998 with the anthropogenic perturbation of the observed atmospheric CFC-11.

### 3.2.2 CFC-11 cycle in the ocean

The model performance is compared with CFC-11 observations of the Global Ocean Data Analysis Project (GLODAP) dataset (Key et al., 2004). Notice that the GLODAP product is compiled from a number of cruise observations, which are mainly derived from the World Ocean Circulation Experiment (WOCE), Joint Global Ocean Flux Study (JGOFS), and Ocean Atmosphere Carbon Exchange Program (OACES) carried out during the 1990s (see Key et al., 2004 for the time periods of these cruises). In addition, several other historical cruise observations from the 1970s and 1980s are also included in the GLODAP data. The sampling population consists of 9618 global observation stations (from 95 cruises) during the period 1985–99, and 2393 global observation stations during the period 1972–90 (21 cruises). There are very few observation stations that were used from historical cruises that date back to 1972. In GLODAP, all these observations are combined into one dataset, and thus they do not exactly represent the scenario of a particular year. However, the majority of samples used in the GLODAP dataset is collected between the period 1990 and 1999 during WOCE cruises, which consist of 80% of the total sampling from 78% of the total cruises. Thus, it is possible to represent the data as a scenario of 1993 or 1995. In this study, we compare the model year 1995 with the observations, unless otherwise specified. This is true especially in the Atlantic Ocean, where the majority of observations included in GLODAP are carried out during the early 1990s.

Before proceeding into real-time runs, we optimize a suitable model configuration from a number of test experiments carried out with different choices of vertical mixing configurations. The results of these test experiments are then compared with CFC-11 observations and an optimum configuration is found. In these test experiments, the main focus is given to tuning the vertical mixing. Such test experiments to find a best configuration is necessary because the offline transport models are operating on some parent model outputs with variable periodicities of input data. In this case, the performance of transport models is sensitive to the frequency of input data, and so the model behaves slightly different for different sets of input feeding. Thus, before getting into application runs, the model performance must be tested with different sets of configurations and a best case should be found.

A number of test experiments are conducted, among which a suite of six are mentioned here. In these runs, the variable parameters are either one or a combination of (i) mixed layer depth, (ii) monthly climatology of wind stress or a globally constant wind stress for KPP, and (iii) inclusion or exclusion of subgrid-scale parameterizations. The mixed layer depth of the GFDL product that we used in this study is somewhat “weaker” than the observations of Kara et al. (2000). Thus, the MLD is multiplied by a factor of 1, 1.5, and 2 for individual test runs.

These three cases are then combined with or without GM subgrid-scale parameterizations and with monthly wind stress climatology or a constant wind stress of  $0.03 \text{ N m}^{-2}$ . Table 3.1 summarizes the experiment cases. Note that all these sensitivity experiments have the same CFC-11 forcing as in OCMIP-2.

**Table 3.1 Test experiments.** GM = Gent and McWilliams's (1990) parameterization; MLD = mixed layer depth; Clim = monthly climatological wind stress.

	1×MLD	1.5×MLD	2×MLD
Clim	1_MDL_GFM_Clim	1.5_MDL_GM_Clim	2_MDL_GM_Clim
0.03	1_MDL_GFM_0.03	1.5_MDL_GFM_0.03	2_MDL_GM_0.03

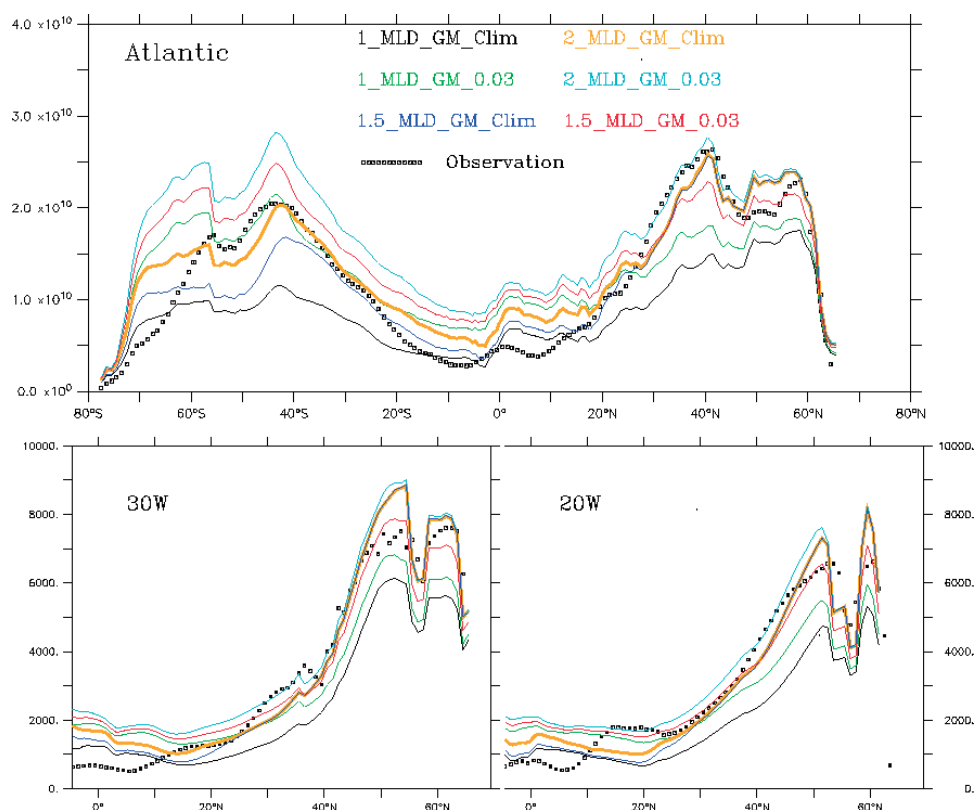


**Figure 3.4** CFC-11 concentration integrated zonally and vertically over (top) the Atlantic Ocean and inventories along (bottom left) 30°W and (bottom right) 20°W. Units are (top)  $\text{pmol m}^2 \text{ kg}^{-1}$  and (bottom)  $\text{pmol m kg}^{-1}$ .

Figure 3.4 shows the CFC-11 simulations of six runs and compares them with the corresponding observations. The plots represent the zonal integral of Atlantic CFC-11 column inventories during 1995. The units are picomole meters squared per kilogram. It is evident

that the model's performance varies considerably among different combinations of configurations. A large difference in the model performance is obvious in the Southern Hemisphere deep convection regions (between 60° and 40°S). The best match with the observation is obtained by the run 2\_MLD\_GM\_Clim (2 times the MLD adopted from GFDL product, with GM parameterization and a climatological stress). The prediction statistical skill and error estimates for each of these test runs are shown in Table 3.2; the correlation between observations and each of these test runs gives us a quantitative evaluation of the cases presented here.

**Table 3.2. Statistical summary of test-run simulations shown in Figure 3.3.** Acronyms are same as those given in Table 3.1.

Data stdv =0.69	1_MLD_ GM_Clim	1_MLD_ GM_0.03	2_MLD_ GM_Clim	2_MLD_ GM_0.03	1.5_MLD_ GM_Clim	1.5_MLD_ GF_0.03
Corr.	0.88	0.87	0.94	0.91	0.92	0.89
Stdv.	0.39	0.46	0.60	0.64	0.62	0.56
Skill	0.69	0.80	0.95	0.94	0.94	0.87
RMS	0.39	0.37	0.23	0.28	0.28	0.32

The discrepancy in the Southern Hemisphere among the different model configurations is mainly due to the difference in the vertical mixing. It is obvious from the figure that the mapping of the same MLD as that of the input data underestimates the vertical mixing in the Southern Hemisphere. However, a constant wind stress of 0.03 N m<sup>-2</sup> erodes the mixing further and deeper, although this is not satisfactory in the Northern Hemisphere. A choice of 1.5 times the MLD gives a better simulation in the Northern Hemisphere, while that in the Southern Hemisphere is still weaker. Column inventories along 20° and 30°W in the Atlantic are shown separately in the bottom panels. It is obvious that the vertical mixing is sensitive to the choice of MLD.

The standard deviation of CFC-11 from the mean inventories in the Atlantic Ocean is 0.69 pmol m<sup>2</sup> kg<sup>-1</sup> (Figure 3.4, top; Table 3.2). Although the standard deviation of three test simulations are close to this value, a high correlation coefficient of 0.95 leads us to prefer the case 2\_MLD\_GM\_Clim as being more suitable (Table 3.2). For this particular case, the statistical skill score (as suggested in Taylor 2001) has a maximum value of 0.95, and a centered pattern of the root-mean-square (RMS) difference has a minimum value of 0.23. Thus, we opt for a choice of 2 times MLD with climatological surface wind stress forcing as the best case, and we consider only this case for the rest of our experiments. We note, however, that this configuration does not imply the ultimate choice for this model; instead, it only means that it is the best-suited configuration for the input data used in this study.

### 3.2.2a Comparison with observations

The deepest penetration of CFC-11 in the global ocean is found in the North Atlantic, where the deep-water formation sites are located. Thus, the deep-water formation process should be simulated well in the model to capture this deep penetration of CFC-11. Therefore,

we concentrate our discussion more on the model's Atlantic Ocean transports and its comparison with observations.

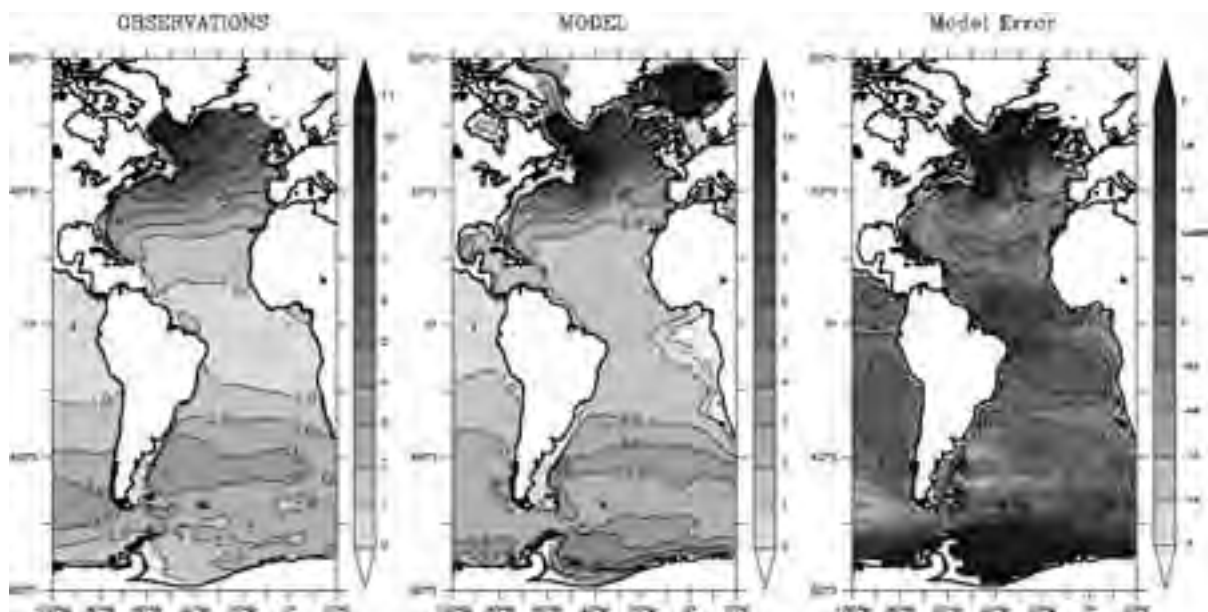


**Figure 3.5** Column inventory of CFC-11 from (left) observations and (middle) model during 1995. The model error is shown as the difference from the (right) observations. Units are  $10^3 \text{ pmol m kg}^{-1}$ .

Figure 3.5 shows the column inventory of CFC-11 (vertically integrated) during 1995 obtained from our model and the corresponding observations obtained from GLODAP. The units are picomole meters per kilogram. Although the column inventories do not represent the deep penetration of tracers explicitly, we begin our comparison for a large-scale model simulation and then proceed to a more detailed comparison of regional vertical profiles. A remarkable similarity in the column inventories of CFC-11 is noticeable in the Atlantic. The deepest convection in the North Atlantic is located in the Labrador Sea, where the mixed layer extends as deep as 800–1300 m (Canuto et al., 2004). Observations show that maximum CFC-11 column inventories are located in the Labrador Sea. The model captures this maximum appreciably well with a magnitude of  $11 \times 10^3 \text{ pmol m kg}^{-1}$  as in the observations. A second maximum inventory is located north of  $70^\circ\text{N}$  in the Greenland and Norwegian Seas. However, there is no available observation of CFC-11 to validate these sites.

The meridional gradient of the CFC-11 column inventory in the model is remarkably similar to that of observations. The North Atlantic water mass is subducted at various locations, such as the Labrador Sea, Denmark Strait, and Iceland-Scotland Overflow regions. CFC-11 in these deep regions is advected southward mainly along with the deep western boundary currents. This southward advection along the western boundary is visible by coastally elongated contours in the observations. It is appreciably represented in the model with a good agreement in magnitude compared to the observations. Further, this southward component of CFC-11 is advected eastward in the deep ocean, which makes a meridional gradient of CFC-11. It is noted that the model has a steeper north-south gradient of CFC-11 than those in the observations.

In the Southern Hemisphere, the high CFC-11 inventory is located between  $40^\circ$  and  $50^\circ\text{S}$ . This is the region where deep convection in the Southern Hemisphere is observed. The maximum penetration of CFC-11 in this belt is found near the South American continent. This

deeply convected water is advected horizontally to the east at a depth of 1000 m and marks a high-concentration belt between 40° and 50°S. This region demarcates the boundary of the subtropical gyre with the polar front, and the water mass is ventilated from the depth below the mixed layer to the deep ocean. This water is referred to as the South Atlantic Mode Water (SAMW), which is a key portion in the southern Atlantic where oceanic uptake of CO<sub>2</sub> is prominent (Dutay et al., 2002). In the Antarctic Ocean, the model shows a mismatch with the observation at 40°W. This may be due to a limitation in the ice-water formation in the model circulations.

The large-scale transport of the model is in good agreement with the observations. This is further evaluated by estimating the error in the model column inventory, which is due to either one or a combination of uncertainties in large-scale circulations and diagnostics used in the model. The error estimates are shown in Figure 3.5 (bottom). Here, the error represents the model drift from the observations. It can be seen that the predictions fall within an overall error bar of  $\pm 0.4 \times 10^3$  pmol m kg<sup>-1</sup> in the Atlantic. This is within a range of  $\pm 10\%$  of the observations. However, the meridional error difference is as large as the maximum error of  $1.5 \times 10^3$  pmol m kg<sup>-1</sup>. In the subtropics, at midlatitude and high latitude, the error bar is within  $\pm 10\%$ , while in the equatorial region, the error is projected as high as 30%. Simulating an accurate meridional transport of tracers is a real challenge in transport models. For example, the atmospheric transport model has large error bars in the interhemispheric gradient. Given the values of  $9 \times 10^3$  pmol m kg<sup>-1</sup> meridional difference of CFC-11 observed in the North Atlantic, an error gradient of  $1.5 \times 10^3$  pmol m kg<sup>-1</sup> reasons an error of 16% in the simulated meridional gradient of CFC-11. The model-centered RMS difference of CFC-11 uptake in the entire Atlantic is 0.23 pmol m<sup>2</sup> kg<sup>-1</sup>, which is  $\pm 5\%$  of the observed mean (Figure 3.4 and Table 3.2). The detailed examination of the vertical profile of the model CFC-11 will further explain this error behavior in the model.

Although the column inventory of CFC-11 in the Atlantic Ocean is well simulated in the model, a detailed vertical structure should be assessed with the observations because the inventories do not provide exact information about the vertical profile. To assess the model's ability to simulate deep convection and ventilation, we compare a few vertical sections in the Atlantic Ocean with the observations. Figure 3.6 shows the North Atlantic cross section along 30°W. The examination of the North Atlantic sections provides the ventilation pathways of the CFC. The key water masses forming in the North Atlantic consist of North Atlantic Deep Water (NADW), which is composed of Lower North Atlantic Deep Water (LNADW) and Upper North Atlantic Deep Water (UNADW). The elevated contours below 1000 m in the deep ocean are due to the renewal of NADW. This is reproduced reasonably well in the model. The elevated contours in the observations show a deep-core maximum between 1500 and 2000 m, which is the UNADW subducted from the base of the mixed layer. The subducted water is shown to be carried farther eastward by the deep ocean currents at this depth. In the model, this core is found above 1500 m. This is partially due to the relatively limited supply of UNADW eastward, which is subducted at the western coast. It is noted that the contour of 0.5 in the model stretches to a depth of 3000 m, as in the observations.

We can assess in more detail the NADW ventilation characteristics from the zonal section at 24°N (Figure 3.7, as shown in Dutay et al. (2002)). The classical 24°N section shows an obvious double core of high concentration at the western boundary, each located between 3000 and 4000 m and between 1500 and 1800 m. The former is the LNADW, which is supplied from the Denmark Strait Overflow Water (DSOW) and Iceland–Scotland Overflow Water (ISOW), which is then carried south along with the deep western boundary currents.



However, there is no obvious deep core reproduced in the model. It should be noted that a high-resolution version of the offline model by Gupta and England (2004) also didn't resolve this double-core structure. Moreover, none of the OCMIP-2 models (most of them are online models) reproduced this double-core structure of CFC. Thus, a comparison between the previous results of OCMIP-2, Gupta and England (2004), and our results shows that the resolution is not the reason for the absence of such a double-core system. Also, our results show that the shallow core (between 1500 and 1800 m) elongates further down to 3000 m. One possibility for the absence of an obvious double-core system in the models may be because of the increased diapycnal mixing that occurs at the region with an intense western boundary current, which smears the cores and mixes each other (although a deep western boundary current exists as distinct cores). It is also noteworthy that the only candidate in OCMIP-2 to resolve this feature reasonably well is Germany's Alfred Wegener Institute for Polar and Marine Research (AWI) model, which was originally an adjoint model that derived circulation from hydrographic and geochemical data (Dutay et al., 2002).

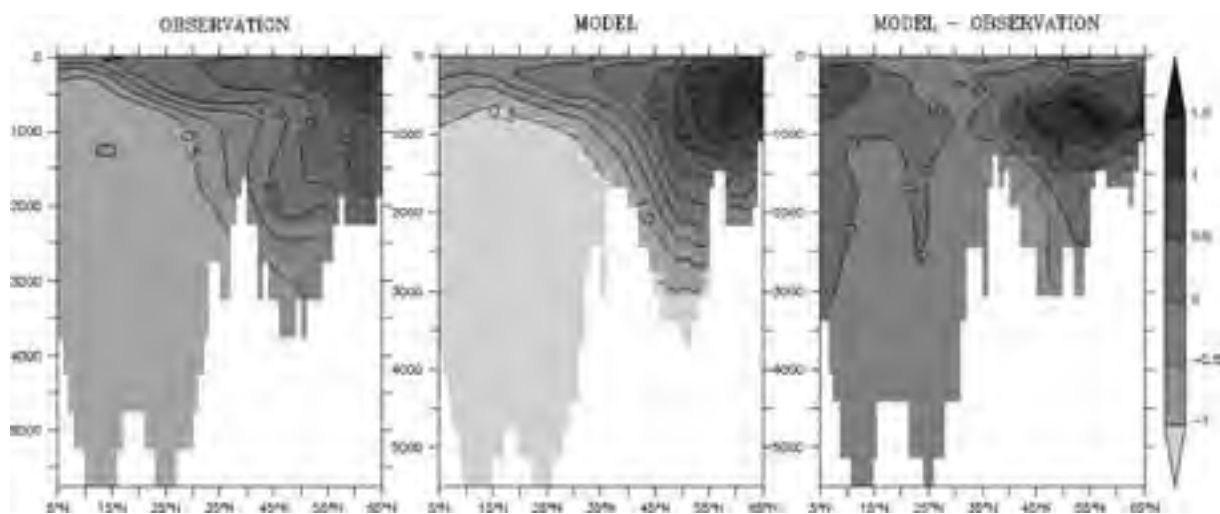


**Figure 3.6** Model-simulated CFC-11 in the North Atlantic (middle) along 30°W during 1995, (left) corresponding observations, and (right) model error. Units are  $\text{pmol kg}^{-1}$ .

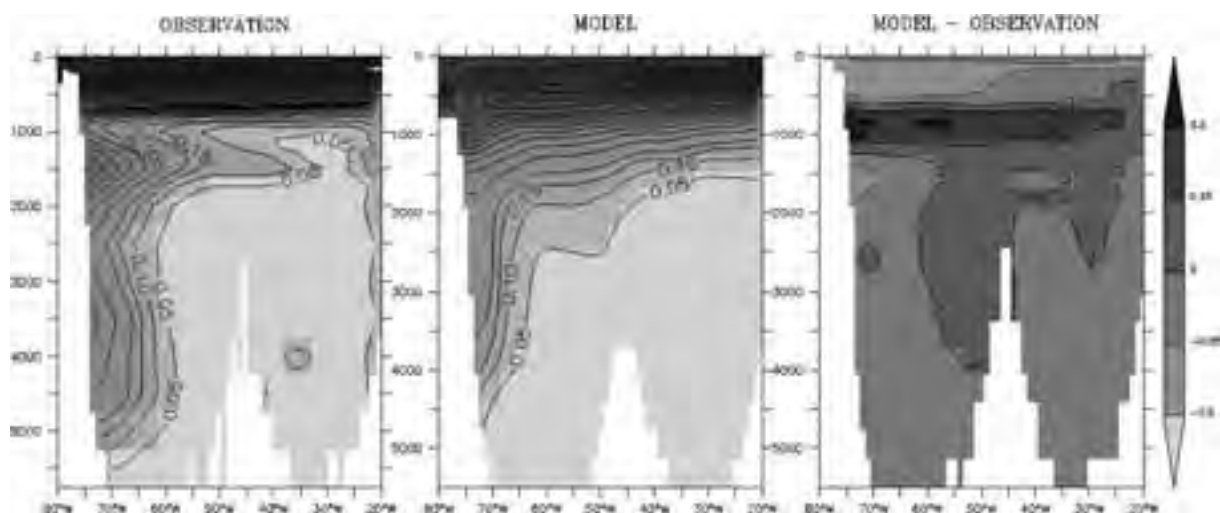


**Figure 3.7** Model-simulated CFC-11 in the North Atlantic (middle) along ~24°N during 1995, (left) corresponding observations, and (right) model error. Units are  $\text{pmol kg}^{-1}$ .

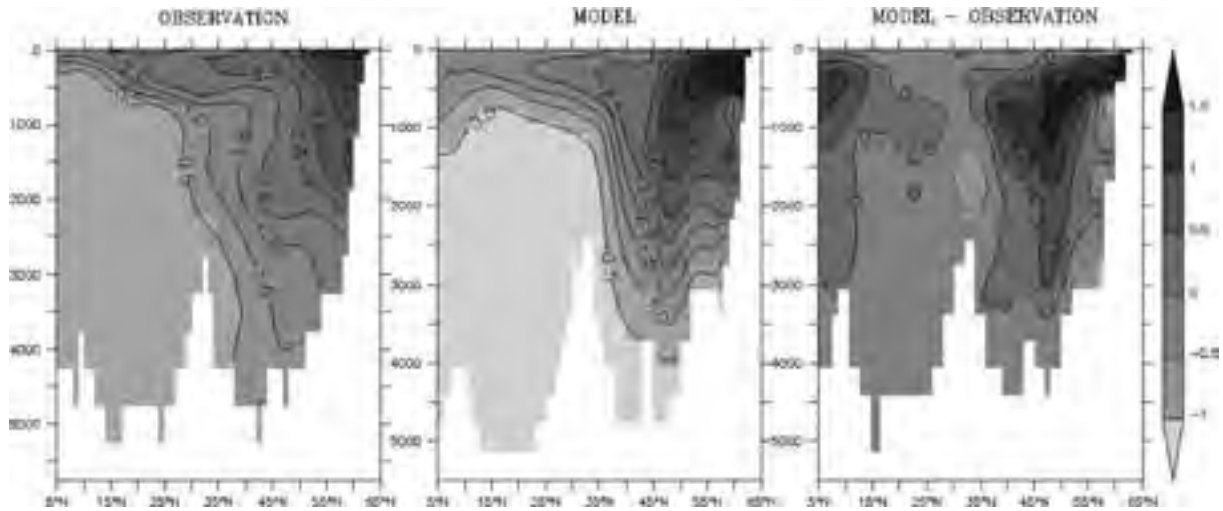


**Figure 3.8** Model-simulated CFC-11 in the North Atlantic (middle) along 40°W during 1995, (left) corresponding observations, and (right) model error. Units are  $\text{pmol kg}^{-1}$ .

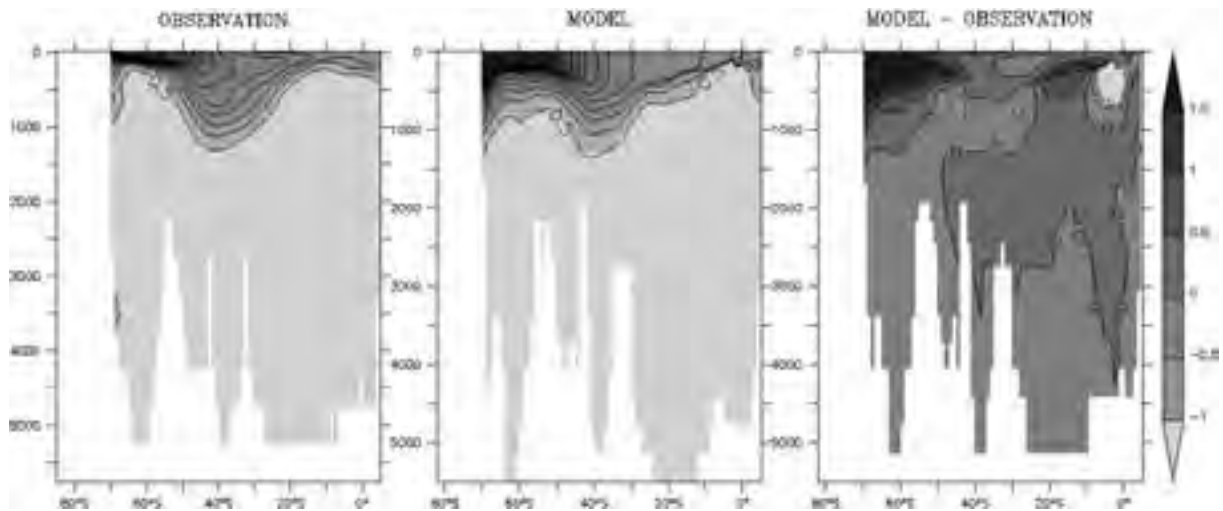


**Figure 3.9** Model-simulated CFC-11 in the South Atlantic (middle) along  $\sim 0^\circ$  during 1995, (left) corresponding observations, and (right) model error. Units are  $\text{pmol kg}^{-1}$ .

Another section along the North Atlantic we have examined is the 40°W section (Figure 3.8), which passes through the “mouth” of the Labrador Sea where it opens to the Atlantic. This is the location where deep penetration of CFC-11 is noted in both the observation and the model. The section shows a reasonable similarity between the observation and the model. The deepest penetration is 4000 m for the contour of  $0.5 \text{ pmol kg}^{-1}$  in both the observation and the model. The tonguelike shape in the model near 55°N shows the mode water formation and subduction at the base of the mixed layer. This is in close agreement with the observation.

A meridional section from the South Atlantic is shown in Figure 3.6. The location of the section is 0°W, which is close to the AJAX section as shown in Dutay et al. (2002). The SAMW formation is reasonable in the model with a maximum penetration depth of nearly 1500 m. This is in good agreement with the observations. The maximum near the southern boundary is somewhat overestimated in the model and elongated deeper. The observation data

in GLODAP didn't show enough concentration in the deep southern boundary as seen from the AJAX section, and the model didn't show any high concentration deep in the southern boundary.

In all the cross sections we presented here, an enhanced vertical mixing in the equatorial region is found in the model, especially at the section close to the American continent (or western part of the Atlantic Ocean). This is not obvious in the observations. The modeled equatorial mixing is relatively stronger than in reality, especially in the western boundary. This is equally reflected in the equatorial region column inventory and resulted in a large error there (Figure 3.5, bottom). However, the relative concentration below the observed limit in the equatorial region is smaller and will not contribute much to the total CFC-11 uptake in the models.

### 3.2.2b Comparison with OCMIP-II participant models

In this section, we compare our results with models that participated in OCMIP-2. This comparison will help us to demonstrate the advantages of using high-resolution offline models to improve the accuracy in transport calculations. This comparison is possible even though the models of OCMIP-2 have a wide range of resolution and vary in their behavior according to the physics included in each model. Any appreciable differences we see among these models and our offline solutions may be attributable to a number of reasons related to the difference in the circulation field resolved in each of these models. The ideal way to compare our result with an OCMIP-2 candidate would be to begin with a comparison of physical fields (i.e., circulation and mixing details) and then move to CFC-11. However, obtaining such fields and a detailed comparison with assimilated circulation that we used in our simulation is impractical and out of our topic. At the same time, a comparison of our offline solutions with CFC-11 observations has shown good agreement, which in turn shows that a comparison of our model results with candidate models of OCMIP-2 will provide a performance assessment in CFC-11 simulation without having a one-to-one detailed comparison of the circulation field between OCMIP-2 candidates and the offline input that we used in our simulation. Moreover, we have used the same surface forcing for CFC-11 as that of OCMIP-2 experiments, which enables us to make a direct comparison.

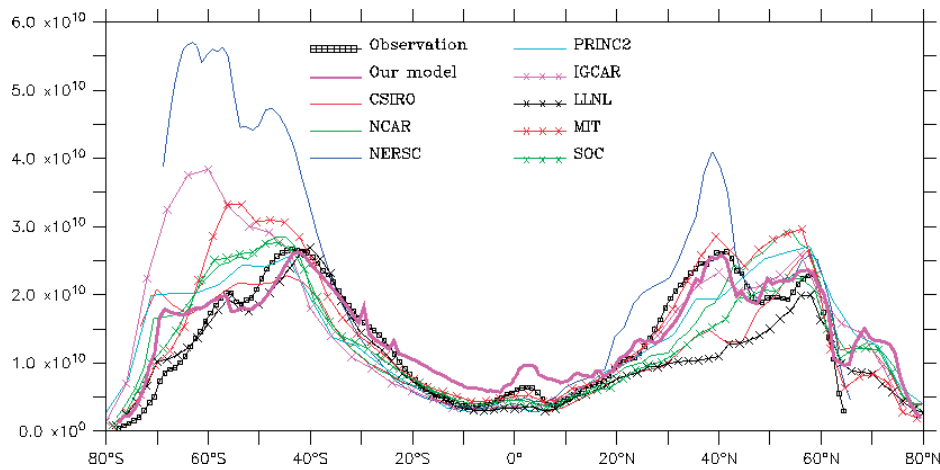
We chose eight models from OCMIP-2 participants for the comparison here. This selection is based on referring to Dutay et al. (2002). Only those candidates that show a reasonable agreement with the observations are included here: Commonwealth Scientific and Industrial Research Organisation (CSIRO), Institute for Global Change Research, Tokyo, Japan (IGCR), L'Institut Pierre-Simon Laplace Coupled Model (IPSL), Lawrence Livermore National Laboratory (LLNL), Massachusetts Institute of Technology (MIT), National Energy Research Scientific Computing Center (NERSC), Princeton University experiment-2 (PRINCE2), and Southampton Oceanography Centre (SOC; see Dutay et al., 2002). All of these models had been run based on the OCMIP-2 CFC-11 flux protocol from 1938 to 1997. We will present a quantitative comparison between our model and these models in the Atlantic.

Figure 3.10 shows the zonally integrated CFC-11 column inventories in the entire Atlantic (100°W ~20°E), as simulated by the candidate models of OCMIP-2, our model, and the corresponding observations. This provides a quantitative comparison of CFC-11 simulated by each of these models. The northern Atlantic ventilation process is captured by participating models of OCMIP-2, although the majority underestimates it. A close examination indicates



that our model has excellent agreement with the observations in the subduction zone of the northern Atlantic. The model spread is relatively larger in the northern Atlantic than in the Southern Ocean. Among the OCMIP-2 candidates, a double peak in the North Atlantic is captured only in MIT, IGCR, and NERSC, although the amplitude is almost double in NERSC. The other candidates do not have an obvious double peak. It is noticeable that our model captures these two maxima remarkably well compared to the observations.

In the Southern Ocean, all models have reasonable performance. Also in this case, our model reproduces both the phase and amplitude of the observed CFC-11 inventory appreciably well. A minimum in CFC-11 inventories around 51°S and a secondary maximum around 57°S are well captured only in our model and LLNL. All other models have a wide range of CFC-11 inventory in the Southern Hemisphere. The deviation of NERSC from the mean state is too large, and the IGCR model also overestimates CFC-11 inventory in the Southern Ocean.



**Figure 3.10** Zonally integrated column inventories of CFC-11 in the entire Atlantic from the candidate models of OCMIP-2, our model, and corresponding observations. Units are  $\text{pmol m}^2 \text{kg}^{-1}$ .

None of the models (including ours) maintains a shallow penetration of CFC-11 that is bound to 70°S, except LLNL. This may be due to the inconsistent ice parameterizations included in the models. The NERSC model shows extremely localized high concentrations in the subduction zone of the SAMW region. In the equatorial region, our model overestimates vertical mixing as compared to the observations as well as the other candidate models of OCMIP-2. However, it is noteworthy that the equatorial pattern is captured by our model even though the mixing is exaggerated. The other candidate models of OCMIP-2 underestimate the vertical mixing in the equatorial region, except MIT, which shows an appreciable match of phase and amplitude with the observations.

The comparison with the other models of OCMIP-2 shows that our model's performance falls within the range achieved by the candidate models of OCMIP-2. These models have varying levels of agreement and disagreement with the observation at various parts of the ocean. For example, IGCR and MIT perform reasonably well in the North Atlantic but have a poor performance in the South Atlantic. LLNL exhibits excellent performance in the South Atlantic but is biased toward underestimation in the northern Atlantic. Some candidates exaggerate the amplitude, while others have different phases. Our model has a good

agreement in both amplitude and phase at the northern as well as the Southern Ocean, while it is exaggerated in amplitude in the equatorial region. By this way of comparison, it is difficult to conclude which model can most accurately simulate the observations.

To achieve a more quantitative comparison among these models as well as with the observations and also to find the skill of these models to simulate a scenario close to reality, we opt for a representation of model statistics as provided in Taylor (2001). Figure 3.11 shows the standard deviations and correlations (with the observations) of the plots given in Figure 3.10. The radial distance from the origin is proportional to the standard deviation and the cosine of the angle between the radial line, and the abscissa is the correlation between each model and the observations. To compare the model's performance in this way, we need a reference point that represents the standard deviation of observations (as seen in Figure 3.11) and a correlation coefficient of 1. Any point in the map is thus defined by a combination of standard deviation and correlation. The models with the best performance in simulating both amplitude and phase of observations will thus lie close to the reference point. A statistical skill score based on standard deviation and correlation of each model is found as that given in Taylor (2001), with a maximum expectation correlation coefficient of  $R_0 = 0.99$ .

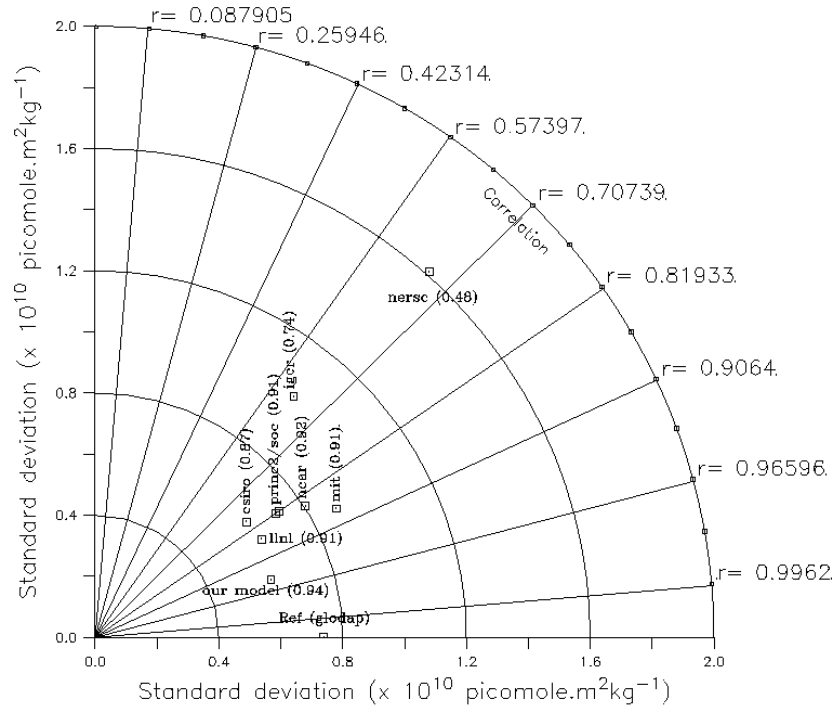


**Figure 3.11 Model std dev and correlation with reference data (GLODAP) are displayed as in Taylor (2001).** The radial lines are labeled by the cosine of the angle made with the abscissa. The reference data have a std dev of 0.74. Our model has a std dev of 0.60 and a correlation coefficient of 0.95. Skill values are given in brackets.

The observation has a standard deviation of  $0.74 \text{ pmol m}^2 \text{ kg}^{-1}$ . The OCMIP-2 candidate models spread in a standard deviation band of 0.60 to 1.62, a correlation band of 0.89 to 0.67, and a skill band of 0.92 to 0.48. Our model has a standard deviation of 0.60 and a skill value of 0.94, which is the highest skill score compared to other models shown here. However, some of the OCMIP-2 models have a standard deviation that is closer to the observations than

that of our model. For example PRINCE2, SOC, and National Center for Atmospheric Research (NCAR) models have better standard deviations, but their correlations are low compared to our model. This shows that these models simulated a more accurate amplitude of the north-south column inventory, but the phase mismatches. On the other hand, in our model, the good correlation and relatively weaker standard deviation (compared to PRINCE2, SOC, and NCAR) mean that the phase of the north-south Atlantic CFC-11 inventory is good, but the amplitude is affected. From Figure 3.10, it is obvious that the equatorial exaggeration of vertical mixing is the reason for this amplitude mismatch in our model. However, the skill measure (which is a collective measure of standard deviation and correlation) shows that our model outperforms the OCMIP-2 candidate models in the Atlantic with a skill score of 0.94, which is the highest among the models compared here.

### 3.2.2c Error comparison with OCMIP-II participant models

The Taylor (2001) diagram explicitly shows the correlation coefficient between the observed field and the model as well as their centered RMS differences, along with the ratio of the standard deviations of the two patterns. The centered RMS difference between the model and the observations is proportional to their distance apart in the same units as the standard deviation. This distance is  $0.14 \times 10^{10} \text{ pmol m}^2 \text{ kg}^{-1}$  in our model. This represents the RMS difference of the model north-south column inventory from the observations. In our model, this corresponds to an error of  $\pm 8\%$  from the observed mean of north-south CFC-11 column inventory. Among the OCMIP-2 participant models, CSIRO and LLNL have the same RMSE difference as ours. The RMSE differences of NCAR and MIT are  $\pm 4\%$  and  $\pm 9\%$ , respectively, which shows that these models (including ours) have error in the amplitude of the north-south column inventory. In our model, this is due to the exaggeration of vertical mixing and the CFC-11 uptake in the equatorial region. The overall error in the tropics in our model is 30%. However, the observations suggest that the tropical Atlantic contains only 18.7% of the total CFC-11 of the entire Atlantic, and thus a model error of 30% in the tropics means only an error of 6% in the total CFC-11 uptake. The minimum RMSE difference of OCMIP-2 participants is found in PRINCE2 and SOC, which have an error of  $\pm 4\%$  from the mean north-south column inventory.

### 3.2.3 Discussion and conclusion

It is evident from Figures 3.10 and 3.11 that our model captures the majority of the column inventory features of CFC-11 remarkably well and has a high skill score compared to the OCMIP-2 participants. Thus, it is useful to point out the reasons for this improved performance in our model compared to that of other candidates of OCMIP-2. The main reason may be the higher resolution of our model compared to the very coarse resolutions used in OCMIP-2. Thus, it is evident that the restriction of resolution because of the cost of computational time in the online models has affected the accuracy in transport, which can be effectively solved by adapting an offline version with reasonable ocean circulation—a real advantage of offline models. This conclusion is consistent with the model results of Gupta and England (2004). Another reason for improvement in our model may be the assimilated oceanic currents that we used to find the transport. Apart from the resolution, the limitations in the model physics also affect the performance of online simulations. Thus, by having an assimilated current as prior information with appreciable periodicity to represent the dominant mode of variability (monthly or weekly), there is a good chance to achieve high accuracy in

transport calculations using offline models.

Our model results show that even though the vertical mixing and horizontal subgrid-scale processes are parameterized in the offline model, the accuracy present in advective components inherited from the assimilated field plays a potential role in improving the transport calculation. Together with the assimilated advection—if it is possible to provide other mixing coefficients from the parent model itself—the offline model could be tuned to get a further and more accurate transport. The accuracy of transport has a critical role in modeling the oceanic uptake of carbonaceous tracers. For instance, the equilibration time scale (time scale to reach an equilibrium between the partial pressures at the ocean–air interface) of CFC-11 is relatively short. Thus, vertical or horizontal transport of surface CFC-11 to any long distances before it equilibrates locally has potential influence on the equilibration time scale of air–sea fluxes and hence the total uptake by the oceans.

Because the ocean acts as a large-scale sink for carbonaceous tracers in the atmosphere, like anthropogenic CO<sub>2</sub>, it is vital to quantify the role of oceans on the life cycle of CO<sub>2</sub> in the hydrosphere and atmosphere. Inadequate observations of parameters that are necessary for the estimation of air–sea exchange of CO<sub>2</sub> and other carbonaceous tracers always force us to depend largely on climate models to assess the fate of these trace materials. However, the climate models that do this job have to undergo several compromises on computational resources and poorly understood carbon physics, mostly resulting in unsatisfactory estimates of carbon fluxes. Thus, the roles of accurate transport calculation have a significant impact on quantifying the oceanic sources and sinks of carbonaceous substances. For the oceans, our study puts forward a suggestion to depend on assimilated ocean currents and other parameters that are mostly close to reality to estimate the transport of trace materials with a cost-effective computation.

Mikaloff Fletcher et al. (2006, 2007) and Gloor et al. (2003) have used inverse methods to find the oceanic sources and sinks of anthropogenic as well as natural CO<sub>2</sub>. The accuracy of the inversion depends solely on the accuracy of transport functions. The comparison of several OCMIP-2 candidate models of coarse resolution [some of these models are also used in inversion experiments of Mikaloff Fletcher et al. (2006, 2007)] showed notable differences in performance as is described in their paper. Comparing our model's results with these models, as well as with the observations, shows that our model has a relatively higher skill score. Therefore, our model is a potential candidate for the inversion studies as used in Mikaloff Fletcher et al. (2006, 2007). We attribute the reasons for this accuracy in our model to the high resolution and to the assimilated ocean currents and hydrography that we used, which are still compatible with cost-effective computation.

Certain shortcomings are present in the current configuration of our model, especially in the equatorial mixing. The mixed layer depth criteria in our best-suited configuration for the set of input data resulted in a stronger vertical mixing in the equatorial region, especially at the western boundary. We have investigated the reason for this behavior in the model in connection with its 2 times the MLD mapping in the present configuration. However, Figure 3.3 shows that even with a scaling factor of 1, the equatorial mixing is exaggerated. The high shear present in the equatorial current may be the reason for the increased mixing resolved in KPP. The numerical diffusion, which is larger in faster current regions, can also be testament to this exaggerated mixing (Kantha and Clayson, 2000).

Another drawback of the present simulation is that we limited our input data to a monthly

periodicity mainly because of unavailability of high-frequency data. Choosing a high-frequency input data such as daily periodicity, if available, could improve the model's performance. The growing availability of reanalysis products for ocean circulation gives us hope to use this model with high-frequency input data in the future. In addition, a comparison of simulations of this model using different assimilated ocean products will give us a clue to the potential biases in the model, such as exaggerated equatorial mixing. A similar intercomparison of transport derived using different assimilated ocean currents is indeed under way. Moreover, our future task is to use this model for coupled ocean-atmosphere inversions for CO<sub>2</sub> fluxes and with OCMIP-2-type biogeochemical modeling experiments by coupling with an ecosystem model.

### 3.2.4 Summary

An offline passive tracer transport model is designed and discussed here. This model was developed at the National Institute for Environmental Studies (NIES) under the carbon cycle research project inside the GOSAT modeling group. The model equations for tracer evolution, vertical mixing, horizontal diffusion, and other subgrid-scale parameterizations are detailed. The model borrows offline fields from precalculated monthly archives of assimilated ocean currents, temperature, and salinity, and evolves a prognostic passive tracer with a prescribed surface forcing. The model's performance is validated by simulating the CFC-11 cycle in the ocean starting from the preindustrial period (1938) with observed anthropogenic perturbations of atmospheric CFC-11 to comply with the OCMIP-2 flux protocol. The model results are compared with ship observations as well as with the results of the candidate models of OCMIP-2 and a performance is assessed. The model simulates the deep ventilation processes in the Atlantic Ocean appreciably well and yields a good agreement in the column inventory of CFC-11 compared to the observation. The error estimates show that the models intake of CFC-11 is within an overall error bar of  $\pm 8\%$  in the Atlantic, while an exaggeration in tropical CFC-11 intake is noted. The spatial pattern of CFC-11 intake is well simulated in the model, with an overall Atlantic correlation of 0.95 compared to the observations. The statistical skill comparison test with the OCMIP-2 participant models shows that our model performs appreciably well in the CFC-11 column inventory simulation. The spatial pattern of CFC-11 inventories in our model has a higher correlation with the observations than the OCMIP-2 participant models. The improvements in performance of our model compared to other models are attributed to its higher resolution and assimilated offline inputs feeding. This shows a potential role in improving transport calculation in the ocean with cost-effective computation.

## 3.3 Coupling of a biogeochemical cycle to OTTM

We have coupled OTTM with a simplified one-component ecosystem model. The physical part of this coupled model is OTTM. In OTTM, the ocean circulation, temperature, and salinity are provided from a pre-calculated data archive. Here, we use forty-year's worth of ocean re-analysis data sets derived from the Geophysical Fluid Dynamics Laboratory (GFDL). The details of the data sources and periodicity are explained in Table 3.3.

**Table 3.3 List of various data sets, periodicity and time-span.** Abbreviations: U and V: Velocities, T: Temperature, S: Salinity, E-P: Evaporation-Precipitation, SSH: Sea surface height TAUX and TAUY: surface wind speed, NHF: Net heat flux, P: Phosphate, U10m and V10m: Surface 10 m wind speed, SSW: Shortwave flux, PAR: Photosynthetically Active Radiation, DIC: dissolved inorganic carbon.

Variables	Data Name	Time-span	Periodicity	Source
U, V, T, S, MLD, E-P SSH	MOM4-SIS- Assimilation	1960-2004	monthly	Delworth et al. (2006) ; Gnanadesikan et al. (2006)
SSW	SOC	Climatology	monthly	Josey et al. (1999)
P	WOA	Climatology	monthly	Conkright et al. (2001)
PAR	SeaWifs	Climatology	monthly	McClain et al. (2004)
U10m, V10m	ERA-40	1960-2001	6-hourly	Uppala et al. (2004)
DIC	GLODAP	Climatology	Annual mean	Key et al. (2004)

### 3.3.1 Carbonate chemistry model

The chemical compartment of the coupled model handles the dissolved inorganic carbon (DIC) as a tracer which is in equilibrium with the atmosphere at the surface through the air-sea gas exchange. Inside the ocean, DIC is composed of  $\text{CO}_3^{2-}$ ,  $\text{HCO}_3^{-}$  and dissolved  $\text{CO}_2$ . All these three components are treated as one tracer of DIC. This model is a solubility pump model as described in the protocols of the Ocean Carbon Cycle Inter Comparison Project-II (OCMIP-II, the document is available at <http://www.ipsl.jussieu.fr/OCMIP/>).

The air-sea gas exchange depends upon a piston velocity  $K_w$  and the difference in partial pressure of  $\text{CO}_2$  ( $p\text{CO}_2$ ) between the surface ocean and the ambient atmosphere above the surface. Since we are primarily interested in the air-sea  $\text{CO}_2$  flux response to changing physical forcing, a constant atmospheric  $p\text{CO}_2$  of 354  $\mu\text{atm}$  (a value observed in 1990) is applied. The air-sea flux is formulated as  $\Phi_{\text{GASEX}} = K_w(p\text{CO}_{2\text{AIR}} - p\text{CO}_{2\text{OCEAN}})$ . The piston velocity  $K_w$  is the turbulent velocity with which the gaseous  $\text{CO}_2$  enters or leaves the surface of the ocean according to the wind speed and  $\text{CO}_2$  solubility conditions as formulated in the Wanninkhof (1992). We use a gas exchange proportionality constant  $a=0.337$ . The surface wind speed is composed of a 10-day average of a 6-hourly squared wind speed which fully accounts for 6-hourly wind speed variance ( $u_{10}^2 + \sigma u_{10}^2$ ) where  $u_{10}$  is the wind speed at 10 meter above the surface. The polar ice caps are used to partially mask the air-sea gas exchange over the sea ice regions by applying a spatial map of ice index ranging from 0.2 to 1 as given in the OCMIP-II.

### 3.3.2 Ecosystem model

The ecosystem model is the same as that used in McKinley et al. (2004). In this model, the net primary production in the euphotic zone is obtained from monthly maps of the



phosphate and light availability, and scaled it by a regional mask which stands for the iron limitation, grazing efficiency, or recycling of the biomass. The export production in the euphotic zone (0-140 m) is formulated as

$$B(z) = -\alpha_{(x,y)} [I_{(x,y,z,t)}/(I_{(x,y,z,t)} + I_0)] [P_{(x,y,z,t)}/(P_{(x,y,z,t)} + P_0)] \quad (7)$$

where,  $\alpha_{(x,y)}$  represents the other controlling factors of the export rates. The values of the maximum export rate,  $\alpha_{(x,y)}$  account for all the processes leading to export which are not represented by the explicit phosphate and light limitation (McKinley et al., 2004). The values of  $\alpha_{(x,y)}$  should be consistent with the model's circulation and climatological nutrient fields. The global ocean is divided into 14 regions and the value of  $\alpha_{(x,y)}$  for each region is defined by following the assumption that a given model flow field will produce an annual mean phosphorous distribution that is consistent with the climatological observations. The ocean regions for  $\alpha$  values are given in McKinley et al. (2004) and further explanation therein. The regions we used is also the same as that of McKinley et al. (2004) while the individual regional values of  $\alpha_{(x,y)}$  are tuned suitably for the circulation used in this study.

The half saturation value for phosphate ( $P_0$ ) is  $0.01 \mu\text{mol kg}^{-1}$  and that for the light ( $I_0$ ) is  $30 \text{ W m}^{-2}$ . The sinking particle flux,  $F(z)$ , is parameterized as in Dutkiewicz et al. (2004). The net export production is converted to an equivalent DIC consumption in the euphotic zone based on the Redfield ratio,  $R_{C:P} = 117:1$ . Within the euphotic zone, the biological source-sink term,  $S_b = B(z) + F(z)$  and below that zone,  $S_b = F(z)$ .

In addition to the surface air-sea gas exchange, dilution of surface water DIC concentration by rainfall and increase in DIC concentration by evaporation are also included in the model. Although the model's kinematic surface boundary conditions incorporate the evaporation and precipitation as vertical velocity at the top model grid cell face, the virtual dilution of the surface layer DIC is provided as a "virtual flux",  $\Phi_{FWEX} = (E-P)DIC_{SURF}$ , where the  $DIC_{SURF}$  is the globally average of the model surface DIC concentration. This is the standard gas exchange formulation of the OCMIP-II protocols. The data for the virtual fluxes are used from the same source of the re-analysis data. The coupled model thus have the following form

$$\partial DIC / \partial Dt = R_{C:P} \cdot S_b(z) + \Phi_{GASEX} + \Phi_{FWEX} \quad (8)$$

where,  $\partial DIC / \partial Dt$  contains the total changes due to advection, mixing, diffusion and eddy induced transport.

### 3.3.3 Data and model setup

The physical parameters borrowed from the data are velocities ( $u, v$ ), temperature, salinity, mixed layer depth, evaporation-precipitation, surface heat flux, surface wind stress (to drive vertical mixing), and sea surface height. (see Section 3.2.1).

The data of surface wind speed for the air-sea gas exchange calculation are taken from the ECMWF surface wind data product (ERA-40 6-hourly, 10 m above the surface, Uppala et al., 2004). The initial condition for DIC is taken from the Global Ocean Data Analysis Project (GLODAP) (Key et al., 2004). Table 3.3 summarizes all of the data sets used in this study and their periodicity, time-span, and respective sources.

The model is run for the mean state of DIC (pre-run) using a monthly mean circulations and other physical parameters derived from the ten-year period between 1975 and 1984. This



data period represents the middle time of the total span of the re-analysis data. We choose this period for deriving the mean circulation and other physical parameters for the pre-run mainly because our interannual DIC simulation starts from 1980. Moreover, the mean circulation, temperature and salinity over a longer span (40 years) will have offsets due to climate change which occurred during the last few decades. Thus, a monthly mean circulation derived from 1975 to 1984 will give us a reasonable mean state of DIC.

The pre-run of the model is initialized with an annual mean values of DIC derived from the GLODAP data (Key et al., 2004). For the pre-run, the surface wind speeds and variances for the air-sea gas exchange are kept as monthly means that are originally taken from the OCMIP-II forcing data sets (available at <http://www.ipsl.jussieu.fr/OCMIP/>). These data are derived from a 5-year average of SSMI satellite monthly-squared wind speed and a variance of the instantaneous wind speed from the corresponding monthly period (see also README.satdat provided by OCMIP-II, available at <http://www.ipsl.jussieu.fr/OCMIP/>).

The pre-run is carried out for 20 years using a monthly mean circulations and the surface gas exchange forcing that are repeated every year. The surface DIC concentration and air-sea CO<sub>2</sub> flux of the model reach quasi-equilibrium states at the end of the first 10 years of the pre-run, and the evolution of DIC and the flux continue with a minimum departure from the mean state thereafter. However, deeper adjustments (below 2000 m) still continue at the end of the 20-year pre-run, because of the deep convections and remineralized DIC from the export production which communicates much slowly with the surface.

The average of the last five year simulation of the pre-run is taken as the restart condition for the interannual simulation. The model starts from the restart condition and passes through the monthly data fields of the year 1980 once and then continue the run from 1980 to 1999 using the real-time data. The model state deviates from the restart condition as soon as the data of 1980 is introduced and a near steady state is reached by the time model passes one time through the data fields of the year 1980.

Our model setup is essentially the same as that of McKinley et al. (2004) except for a few points. Our model circulations and other physical parameters are taken from a re-analysis data set whereas in McKinley et al. (2004) those were taken from the MIT GCM simulations. Our physical model contains real time variability of the ocean constrained with the observations in the assimilation processes. The second and an important difference is that we use a full depth ocean whereas McKinley et al. (2004) have restored their below-1100 m DIC to the initial conditions. Thus our model has reasons to represents more realistic deep ventilation processes which might not be represented, especially in the interannual scale, in the work of McKinley et al. (2004). Another minor factor of difference is that our model domain extends to 85° to the north and south whereas it was only up to 73° in McKinley et al. (2004).

### 3.3.4 The model air-sea CO<sub>2</sub> flux

The global mean CO<sub>2</sub> flux of the model is calculated from 1980 to 1999. The global mean has a net sink of  $1.42 \pm 0.40 \text{ PgCyr}^{-1}$ . This value is less than that of the McKinley et al. (2004) by  $0.36 \text{ PgCyr}^{-1}$ , partially because their model domain ranges only from 73°S to 73°N. Within that domain, our model shows a net sink of  $1.58 \text{ PgCyr}^{-1}$ . The global estimate of the mean sink generally agrees with other modeling efforts (for example Le Quéré et al. (2000), Wetzel et al. (2005) and observations of Takahashi et al. (2002)).

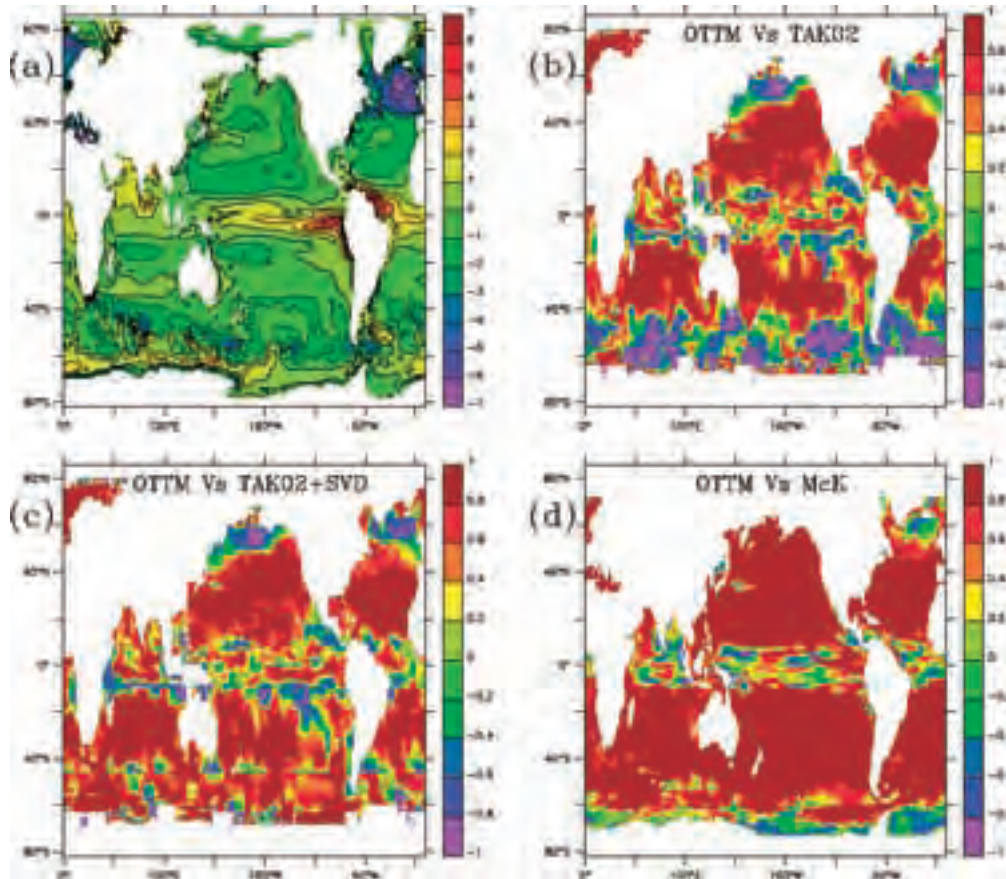


**Figure 3.12 Mean air-sea  $\text{CO}_2$  fluxes of the model over the 1980-1999 period ( $\text{molm}^{-2}\text{yr}^{-1}$ ).** The positive values denote the sources. Correlation of model climatological seasonal cycle with (a) Takahashi (2002), (b) Takahashi (2002) corrected with SVD and (d) McK (McKinley et al. (2004)). A value above 0.71 and 0.58 are above 99% and 95% level of significance, respectively.

The model captures the major features of the global  $\text{CO}_2$  flux such as the eastern tropical Pacific emissions and the high-latitude sinks with maximum amplitude in the northern Atlantic. Figure 3.12 shows twenty-year mean  $\text{CO}_2$  fluxes estimated by the model. The spatial pattern of the annual mean fluxes closely resemble with those by Takahashi et al. (2002) and McKinley et al. (2004). The interannual variability of the global  $\text{CO}_2$  flux in our model (figure not shown) follows the tropical Pacific variability associated with ENSO which is consistent with the observations of Feely et al. (1999) and other biogeochemistry general circulation models of Le Quéré et al. (2000), Obata and Kitamura (2003), McKinley et al. (2004), and Wetzel et al. (2005). The peak-to-peak maximum amplitudes of interannual variability of the global ocean and equatorial Pacific in our model are  $-0.35$  to  $0.45$  and  $-0.25$  to  $0.35$   $\text{PgCyr}^{-1}$ , respectively. These are slightly less than the model results of Le Quéré et al. (2000) where the corresponding amplitudes are  $0.4$  to  $-0.4$  and  $-0.2$  to  $0.4$   $\text{PgCyr}^{-1}$ , respectively. The standard deviation of the global  $\text{CO}_2$  flux in our model is  $0.40$   $\text{PgCyr}^{-1}$  while the equatorial Pacific has a standard deviation of  $0.36$   $\text{PgCyr}^{-1}$ . The correlation of the equatorial Pacific interannual variability with the global variability is  $0.77$  and shows that 60% of the global variability is explained by the variability in the Pacific alone. The corresponding variance explained in the modeling results of Le Quéré et al. (2000) is 70%. The seasonal correlation of our model global  $\text{CO}_2$  flux with that by Takahashi (2002) is shown in Figure 3.12b. The correlation is

above 95% level of significance in the low-latitude and in the tropical oceans. However, there is a significant miss-match in the seasonal cycle in the high-latitude oceans such as the Southern Ocean, northern Pacific, and northern Atlantic. The correlations of these regions have significantly improved, especially in the case of Southern Ocean, when inverse correction of atmospheric CO<sub>2</sub> data is incorporated to the Takahashi (2002) data. The result is shown in Figure 3.12c. The corresponding correlation of our model with McKinley et al. (2004) shows a very good agreement in the global seasonal cycle of CO<sub>2</sub>, although a poor correlation is found in the equatorial region, a region south of 70° S and east of 150° E, and in the northern Atlantic. The equatorial variabilities in the flux correlation might have an origin related to the equatorial dynamics, which are quite expectable because we use a different ocean circulation than that used in McKinley et al. (2004).

### 3.3.5 Summary

OTTM is coupled to a simple ecosystem model and a carbonate chemistry model, and the coupled model is used to simulate interannual air-sea CO<sub>2</sub> flux from 1980 to 1999. The multiyear mean CO<sub>2</sub> flux by the model has a net sink and is consistent with the observations. The seasonal correlation of CO<sub>2</sub> flux by the model to the observation is statistically significant although a relatively poor correlation is found in some regions especially in the Southern Ocean. The model simulations can be constrained with observations using assimilation techniques and such work is ongoing.

## References

- Asselin, R. (1972) Frequency filters for time integrations. *Mon. Wea. Rev.*, 100, 487-490.
- Bryan, K., Lewis, L.J. (1979) A watermass model of the World ocean. *J. Geophys. Res.*, 84, 2503-2517.
- Canuto, V.M., Howard, A., Hogan, P., Cheng, Y., Dubovikov, M.S., Montenero, L.M. (2004) Modeling ocean deep convection. *Ocean Modelling*, 7, 75-95.
- Conkright, M.E., Locamini, R.A., Gracia, H.E., O'Brien, T.D., Boyer, T.P., Stephens, C., Antonov, J.J. (2001) World Ocean Atlas 2001: Objective analyses, Data statistics and figures, CD-ROM Documentation. National Oceanographic Data Center, M. D., 17 pp.
- Delworth, T.L., et al. (2006) GFDL's CM2 Global coupled climate models. Part I: Formulation and simulation characteristics. *J. Climate*, 19, 643-674.
- Dutay, J.C., et al. (2002) Evaluation of ocean model ventilation with CFC-11; comparison of 13 global ocean models. *Ocean Modelling*, 4, 89-120.
- Dutkiewicz, S., Marshall, M.F.J., Gregg, W.W. (2001) Interannual variability of phytoplankton abundances in the north Atlantic. *Deep-Sea Res.*, 48, 2323-2344.
- Enting, I.G. (2002) Inverse problems in Atmospheric constituent transport. Cambridge niversity Press, 392 pp.
- Feely, R.A., et al. (2002) Seasonal and interannual variability of CO<sub>2</sub> in the equatorial pacific. *Deep-Sea Res.*, 14, 2443-2469.
- Fukumori, I., Lee, T., Cheng, B., Menemenlis, D. (2004) The origine, pathway and destination of Nino-3 water estimated by a simulated passive tracer and its adjoint. *J. Phys. Oceanogr.*, 34, 582-604.
- Gent, P.R., McWilliams, J.C. (1990) Isopycnal mixing in Ocean circulation models. *J. Phys. Oceanogr.*, 20, 150-155.
- Gloor, M., Gruber, N., Sarmiento, J., Sabine, C.L., Feely, R.A., Rödenbeck, C. (2003) A first estimate of present

- and preindustrial air-sea CO<sub>2</sub> flux patterns based on ocean interior carbon measurements and models. *Geophys. Res. Lett.*, 30, 1010, doi:10.1029/2002GL015594.
- Gnanadesikan, A. et al. (2006) GFDL's CM2 Global coupled climate models. Part II: The baseline ocean simulation. *J. Climate*, 19, 675-697.
- Gupta, A.S., England, M. (2004) Evaluation of Interior Circulation in a high-resolution global Ocean model. Part I: Deep and bottom waters. *J. Phys. Oceanogr.*, 34, 2592-2614.
- Hecht, M.W., Holland, W.R., Rasch, P.J. (1995) Upwind-weighted advection schemes for ocean tracer transport: An evaluation in a passive tracer context. *J. Geophys. Res.*, 100, 20763-20778.
- Hellerman, S., Rosenstein, M.J. (1983) Normal monthly windstress over the world ocean with error estimates. *J. Phys. Oceanogr.*, 13, 1093-1104.
- Hourdin, F., Talagrand, O. (2002) Eulerian backtracking of atmospheric tracers: I adjoint derivation and parametrization of subgrid-scale transport. *Quart. J. Roy. Meteor. Soc.*, 132, 567-583, doi:10.1256/qj.yy.n.
- Hourdin, F., Talagrand, O., Idelkadi, A. (2002) Eulerian backtracking of atmospheric tracers: II Numerical aspects. *Quart. J. Roy. Meteor. Soc.*, 132, 585-603, doi:10.1256/qj.yy.n.
- Josey, S.A., Kent, E.C., Taylor, P.K. (1999) New insights into the ocean heat budget closure problem from analysis of the soc air-sea flux climatology. *J. Climate*, 12, 2856-2880.
- Kantha, L.H., Clayson, C.A. (2000) Numerical Models of Oceans and Oceanic Processes, 66. International Geophysics Series, 940 pp.
- Kara, B.A., Rochford, P.A., Hulburt, E. (2000) An optimal definition for ocean mixed layer. *J. Geophys. Res.*, 105, 16803-16821.
- Key, R.M., Kozyr, A., Sabine, C.L., Lee, K., Wanninkhof, R., Bullister, J.L., Feely, R.A., Millero, F.J., Mordy, C., Peng, T.-H. (2004) A global ocean carbon climatology: Results from Global Ocean Data Analysis Project (GLODAP). *Global Biogeochem. Cycles*, 18, GB4031, doi:10.1029/2004GB002247.
- Khatiwala, S. (2007) A computational framework for simulation of biogeochemical tracers in the ocean. *Global Biogeochem. Cycles*, 21, GB3001, doi:10.1029/2007GB002923.
- Khatiwala, S., Visbeck, M., Cane, M.A. (2005) Accelerated simulation of passive tracers in ocean circulation models. *Ocean Modelling*, 9, 51-69.
- Large, W.G., McWilliams, J.C., Doney, S.C. (1994) Ocean vertical mixing: A review and a model with a nonlocal boundary layer parameterization. *Rev. Geophys.*, 32, 363-403.
- Le-Quéré, C., Orr, J.C., Monfray, P., Aumont, O., Madec, G. (2000) Interannual variability of the oceanic sink of CO<sub>2</sub> from 1979 through 1997. *Global Biogeochem. Cycles*, 14, 1247-1265.
- McClain, C.R., Feldman, G.C., Hooker, S.B. (2004) An overview of the SeaWiFs project and strategies for producing a climate research quality global ocean bio-optical time series. *Deep-Sea Res.*, 51, 5-42.
- McKinley, G.A., Follows, M.J., Marshall, J. (2004) Mechanism of air-sea CO<sub>2</sub> flux variability in the equatorial Pacific and North Atlantic. *Global Biogeochem. Cycles*, 18, GB2011, doi:10.1029/2003GB002179.
- Mellor, G.L., Yamada, T. (1982) Development of a turbulent closure model for geophysical fluid problems. *Rev. Geophys.*, 20, 851-875.
- Mikaloff Fletcher, S.E., Gruber, N., Jacobson, A.R., Doney, S.C., Dutkiewicz, S., Gerber, M., Follows, M., Joos, F., Lindsay, K., Menemenlis, D., et al. (2006) Inverse estimate of anthropogenic CO<sub>2</sub> uptake, transport and storage by the ocean. *Global Biogeochem. Cycles*, 20, GB2002, doi:10.1029/2005GB002530.
- Mikaloff Fletcher, S.E., Gruber, N., Jacobson, A.R., Gloor, M., Doney, S.C., Dutkiewicz, S., Gerber, M., Follows, M., Joos, F., Lindsay, K., et al. (2007) Inverse estimates of the oceanic sources and sinks of natural CO<sub>2</sub> and the implied oceanic carbon transport, *Global Biogeochem. Cycles*, 21, GB1010, doi: 10.1029/2006GB002751.
- Obata, A., Kitamura, Y. (2003) Interannual variability of the air-sea exchange of CO<sub>2</sub> from 1961 to 1998 simulated with a global ocean circulation-biogeochemistry model. *J. Geophys. Res.*, 108(C11), 3337, doi:10.1029/2001JC001088.

- Pacanowski, R.C., Griffies, S.M. (1999) Users guide for MOM 3.0. Geophysical Fluid Dynamics Laboratory, Princeton University, NJ, 668 pp.
- Redi, M. (1982) Oceanic isopycnal mixing by coordinate rotation. *J. Phys. Oceanogr.*, 12, 1154-1158.
- Taylor, K.E. (2001) Summarizing multiple aspects of model performance in a single diagram. *J. Geophys. Res.*, 106, 7183-7192.
- Takahashi, T., Sutherland, S.C., Sweeney, C., Poisson, A., Metzl, N., Tilbrook, B., Bates, N., Wanninkhof, R., Feely, R.A., Sabine, C., Olafsson, J., Nojiri, Y. (2002) Global sea-air CO<sub>2</sub> flux based on climatological surface ocean pCO<sub>2</sub> and seasonal biological and temperature effect. *Deep-Sea Res.*, 49, 1601-1622.
- Uppala, S., Kallberg, P., Hernandez, A., Saarinen, S., Fiorino, M., Li, X., Onogi, K., Sokka, N., Andrea, U., Bechtold, V.C. (2004) ERA-40: ECMWF 45-year reanalysis of the global atmosphere and surface conditions 1957-2002. *ECMWF newsletter*, 101, 2-21.
- Valsala, V., Ikeda, M. (2007) Pathways and effects of the Indonesian Throughflow water in the Indian Ocean using Particle trajectory and Tracers in an OGCM. *J. Climate*, 20, 2994-3017.
- Valsala, V., Maksyutov, S., Ikeda, M. (2008) Design and Validation of an Offline Oceanic Tracer Transport Model for a Carbon Cycle Study. *J. Climate*, 21, 2752-2769.
- Wanninkhof, R. (1992) Relationship between wind speed and gas exchange over the ocean. *J. Geophys. Res.*, 97, 7373-7382.
- Wetzel, P., Winguth, A., Maier-Reimer, E. (2005) Sea to air CO<sub>2</sub> flux from 1948 to 2003: A model study. *Global Biogeochem. Cycles*, 19, GB2005, doi:10.1029/2004GB002339.





## Chapter 4

### **An empirical model simulating diurnal and seasonal CO<sub>2</sub> flux for diverse vegetation types and climate conditions**

(Published in Biogeosciences, Vol. 6, 585-599, 2009. Reproduced by permission of authors.)

Makoto Saito<sup>1\*</sup>, Shamil Maksyutov<sup>1</sup>, Ryuichi Hirata<sup>2</sup>, and Andrew D. Richardson<sup>3</sup>

1. Center for Global Environmental Research, National Institute for Environmental Studies, Tsukuba, Ibaraki 305-8506, Japan
2. National Institute for Agro-Environmental Sciences, Tsukuba, Ibaraki 305-8604, Japan
3. Complex Systems Research Center, University of New Hampshire, Durham, NH, USA

\*Corresponding author: Dr. Makoto Saito, Center for Global Environmental Research, National Institute for Environmental Studies, 16-2 Onogawa Tsukuba Ibaraki 305-8506, Japan. E-mail: [saito.makoto@nies.go.jp](mailto:saito.makoto@nies.go.jp)



## Abstract

We present an empirical model for the estimation of diurnal variability in net ecosystem CO<sub>2</sub> exchange (NEE) in various biomes. The model is based on the use of a simple saturated function for photosynthetic response of the canopy, and was constructed using the AmeriFlux network dataset that contains continuous eddy covariance CO<sub>2</sub> flux data obtained at 24 ecosystems sites from seven biomes. The physiological parameters of maximum CO<sub>2</sub> uptake rate by the canopy and ecosystem respiration have biome-specific responses to environmental variables. The model uses simplified empirical expression of seasonal variability in biome-specific physiological parameters based on air temperature, vapor pressure deficit, and annual precipitation. The model was validated using measurements of NEE derived from 10 AmeriFlux and four AsiaFlux ecosystem sites. The predicted NEE had reasonable magnitude and seasonal variation and gave adequate timing for the beginning and end of the growing season; the model explained 83–95% and 76–89% of the observed diurnal variations in NEE for the AmeriFlux and AsiaFlux ecosystem sites used for validation, respectively. The model however worked less satisfactorily in two deciduous broadleaf forests, a grass land, a savanna, and a tundra ecosystem sites where leaf area index changed rapidly. These results suggest that including additional plant physiological parameters may improve the model simulation performance in various areas of biomes.

**Keywords:** *Empirical model, Net ecosystem exchange, Diurnal variability, Seasonal variability, AmeriFlux, AsiaFlux*

## 4.1 Introduction

Simulation of atmospheric CO<sub>2</sub> variability by atmospheric transport modeling depends critically on the use of terrestrial ecosystem models to accurately simulate diurnal and seasonal variations in terrestrial biospheric processes. Comparisons of seasonal cycles and their amplitudes between observed atmospheric CO<sub>2</sub> variability and that simulated by several terrestrial ecosystem models based on simplified assumptions of biospheric processes have often shown poor agreement (e.g., Nemry et al., 1999). Often model parameter adjustment is necessary to improve fit with the atmospheric observations. Fung et al. (1987), for example, adjusted the seasonal cycle amplitude by modifying the value of the Q<sub>10</sub> temperature coefficient for ecosystem respiration.

Successful simulations of seasonal cycle have been made with more recent and sophisticated models, e.g., CASA (Potter et al., 1993; Randerson et al., 1997). Process-based models differ in their parameterization of primary production. Models based on light-use efficiency, such as CASA and TURC (Ruimy et al., 1996), assume a linear relationship between monthly net primary production (NPP) and monthly solar radiation (Monteith, 1972) that is limited by water availability and temperature. Although these models appear to be successful in seasonal cycle simulation as a whole, their extension to cover diurnal cycles should be accompanied by the introduction of a more realistic, non-linear relationship between CO<sub>2</sub> uptake by terrestrial vegetation and solar radiation at an hourly time scale. The biochemical model proposed by Farquhar et al. (1980) describes the dependence of photosynthesis on solar radiation, with CO<sub>2</sub> uptake rate limited by maximum photosynthetic capacity. This concept is used widely in land-surface schemes for meteorology and hydrology, such as SiB (Sellers et al., 1986) and LSM (Bonan, 1996; 1998), but is less successful in carbon cycle studies because of a lack of empirical data or models for describing the seasonal and spatial variability of the necessary parameters, such as maximum photosynthetic capacity. Alternative ways of evaluating biospheric processes are therefore required for the estimation of diurnal cycles in CO<sub>2</sub> variability. In some cases, empirical models can fit the data more closely than mechanistic models (Thornley, 2002).

For studies of the diurnal cycle of CO<sub>2</sub> variability, long-term field measurement studies using the eddy covariance method have been conducted in recent years at many sites, covering various ecosystems around the world (Baldocchi, 2008). These sites are now organized into a global network, FLUXNET, and a large body of observation data is being accumulated. The eddy covariance method routinely provides direct measurements of net ecosystem CO<sub>2</sub> exchange (NEE) between the atmosphere and the biosphere. The data obtained from these field measurements can be useful, especially for constructing models to predict the diurnal cycle of CO<sub>2</sub> variability associated with biospheric processes, since they provide direct information on turbulence and scalar fluctuations at time scales from seconds to hours over the local vegetation canopy.

In the present work, our focus is on constructing a model that simulates the diurnal variability of NEE in various ecosystems based solely on environmental forces. For this work, we used data from the AmeriFlux and AsiaFlux networks.

## 4.2 Materials and methods

### 4.2.1 Input data

All half-hourly or hourly CO<sub>2</sub> flux data used were obtained from the AmeriFlux network (Hargrove et al., 2003). Sixty-two years' worth of eddy covariance flux data taken from 24 AmeriFlux ecosystem sites and covering seven major biomes in the latitudes from Alaska to Brazil were analyzed. The biomes consisted of six evergreen needle-leaf forests (ENF), two evergreen broadleaf forests (EBF), four deciduous broadleaf forests (DBF), four mixed forests (MF), three grasslands (GRS), two savannas (SVN), and three tundra ecosystems (TND) (Table 4.1). Each site was equipped with an eddy covariance system consisting of an open- or closed-path infrared gas analyzer and a three-dimensional sonic anemometer/thermometer. AmeriFlux Level 2 products, which contain non-gap-filled CO<sub>2</sub> flux data, were used as input data to avoid contamination associated with gap-filling procedures. The periods analyzed for each ecosystem site are listed in Table 4.1.

**Table 4.1 List of AmeriFlux eddy covariance measurement sites analyzed in this study.** Annual mean temperature (AMT) and annual precipitation (AP) are mean values for the period indicated.

Site, country	Year	Latitude, longitude	AMT (°C)	AP (mm)	Reference
<b>Evergreen needle leaf forest (ENF)</b>					
UCI-1930 burn site, Canada	2002–2004	55.91°N, 98.53°W	-2.7	412	Wang et al. (2003)
UCI-1850 burn site, Canada	2002–2004	55.88°N, 98.48°W	-2.7	412	McMillan et al. (2008)
Duke Forest loblolly pine, USA	2002–2004	35.98°N, 79.09°W	17.3	1140	Katul et al. (1999)
Holland forest, USA	2002–2004	45.20°N, 68.74°W	6.8	836	Hollinger et al. (2004)
Metolius, USA	2004–2005	44.45°N, 121.56°W	9.1	405	Schwarz et al. (2004)
Slashpine-Donaldson, USA	2002–2004	29.76°N, 82.16°W	20.4	1072	Gholz and Clark (2002)
<b>Evergreen broadleaf forest (EBF)</b>					
Santarem-Km67-Primary Forest, Brazil	2002–2004	2.86°S, 54.96°W	25.3	1591	Martens et al. (2004)
Florida-Kennedy Space Center, USA	2004–2006	28.61°N, 80.67°W	21.6	1123	Dore et al. (2003)
<b>Deciduous broadleaf forest (DBF)</b>					
Duke Forest hardwoods, USA	2003–2005	35.97°N, 79.10°W	15.1	1091	Katul et al. (2003)
Harvard Forest EMS Tower, USA	2001–2003	42.54°N, 72.17°W	7.5	1023	Goulden et al. (1996)
Missouri Ozark Site, USA	2005–2006	38.74°N, 92.20°W	13.5	878	Gu et al. (2006)
Bartlett Experimental Forest, USA	2004–2005	44.07°N, 71.29°W	7.1	1402	Jenkins et al. (2007)
<b>Mixed forest (MF)</b>					
Intermediate hardwood, USA	2003	46.73°N, 91.23°W	5.3	625	—
Mature red pine, USA	2003–2005	46.74°N, 91.17°W	5.6	706	—
Mixed young jack pine, USA	2004	46.65°N, 91.09°W	5.0	649	—
Park Falls/WLFF, USA	1997, 1999	45.95°N, 90.27°W	5.2	842	Yi et al. (2001)
<b>Grassland (GRS)</b>					
Duke Forest open field, USA	2003–2004	35.97°N, 79.09°W	14.9	1144	Katul et al. (2003)
Brookings, USA	2005–2006	44.35°N, 96.84°W	7.2	608	Gilmanov et al. (2005)
Walnut River Watershed, USA	2002–2004	37.52°N, 96.86°W	13.7	1046	LeMone et al. (2002)
<b>Savanna (SVN)</b>					
Santa Rita Mesquite, USA	2004–2006	31.82°N, 110.87°W	19.1	303	Scott (2008) <sup>†</sup>
Audubon Research Ranch, USA	2004–2006	31.59°N, 110.51°W	15.8	361	—
<b>Tundra (TND)</b>					
Atkasuk, USA	2004–2006	70.47°N, 157.41°W	-10.6	108	—
Barrow, USA	2000–2002	71.32°N, 156.63°W	-11.3	172	Eugster et al. (2000)
Ivotuk, USA	2004–2006	68.49°N, 155.75°W	-9.3	241	Epstein et al. (2004)

<sup>†</sup> personal communication

Half-hourly or hourly air temperature (°C), vapor pressure deficit (VPD; kPa), incident photosynthetic photon flux density (PPFD;  $\mu\text{mol photon m}^{-2} \text{s}^{-1}$ ), and precipitation (mm) for

individual sites were also obtained from the AmeriFlux network. For all sites, air temperature and precipitation data that were missing because of instrument malfunction were filled using the Global Surface Summary of Day (GSOD) data sets to compute annual mean temperature and annual precipitation. The GSOD is a product of the Integrated Surface Data provided by the National Climate Data Center, and includes 13 daily summary parameters over 9000 global stations.

#### 4.2.2 Modeling approach

To predict vegetation photosynthesis and its light response, a nonrectangular hyperbolic model:

$$NEE = \frac{1}{2\theta} \left( \alpha Q + P_{\max} - \sqrt{(\alpha Q + P_{\max})^2 - 4\alpha\theta Q P_{\max}} \right) - RE \quad \text{Equation (1)}$$

has been widely applied (e.g., Rabinowitch, 1951; Peat, 1970), where  $\alpha$  is the initial slope of the light response curve and an approximation of the canopy light utilization efficiency ( $\mu\text{molCO}_2 (\mu\text{mol photon})^{-1}$ ),  $P_{\max}$  is the maximum  $\text{CO}_2$  uptake rate of the canopy ( $\mu\text{mol CO}_2 \text{ m}^{-2} \text{ s}^{-1}$ ),  $RE$  is the average daytime ecosystem respiration ( $\mu\text{mol CO}_2 \text{ m}^{-2} \text{ s}^{-1}$ ),  $\theta$  is a curvature parameter, and  $Q$  is PPFD. Johnson and Thornley (1984) have shown that a nonrectangular hyperbola predicts the integrated daily canopy photosynthesis with an accuracy better than 1% when it is averaged over various irradiances. More recently, this hyperbola has been successfully used in the gap-filling method to obtain continuous eddy covariance  $\text{CO}_2$  fluxes over a year, and to estimate the total annual carbon budget over various biomes (e.g., Gilmanov et al., 2003; Hirata et al., 2008).

Here, we derive a simple and empirical model for predicting the diurnal variability in  $NEE$  over a number of biomes on the basis of the nonrectangular hyperbolic model. To apply the nonrectangular hyperbola, the unknown number parameters ( $\alpha$ ,  $P_{\max}$ , and  $RE$  in Eq. (1)) have to be determined, whereas  $\theta$  is fixed at 0.9 following Kosugi et al. (2005) and Saigusa et al. (2008). To formulate individual unknown parameters, we first calculated the seasonal course of those parameters for every site listed in Table 4.1 by using all available daytime data. The values of parameters were estimated for each day by fitting the data to Eq. (1) using the least-squares method. To reduce poor fitting of Eq. (1) that results from the limited availability and noise in  $\text{CO}_2$  flux data, the parameters for each day were estimated using a 15-day moving window. Individual parameters exhibited seasonal variations, and the variability and amplitude of individual parameters clearly differed among the ecosystem sites and biomes measured. Below we describe how we formulated the seasonal courses of three unknown parameters for each biome.

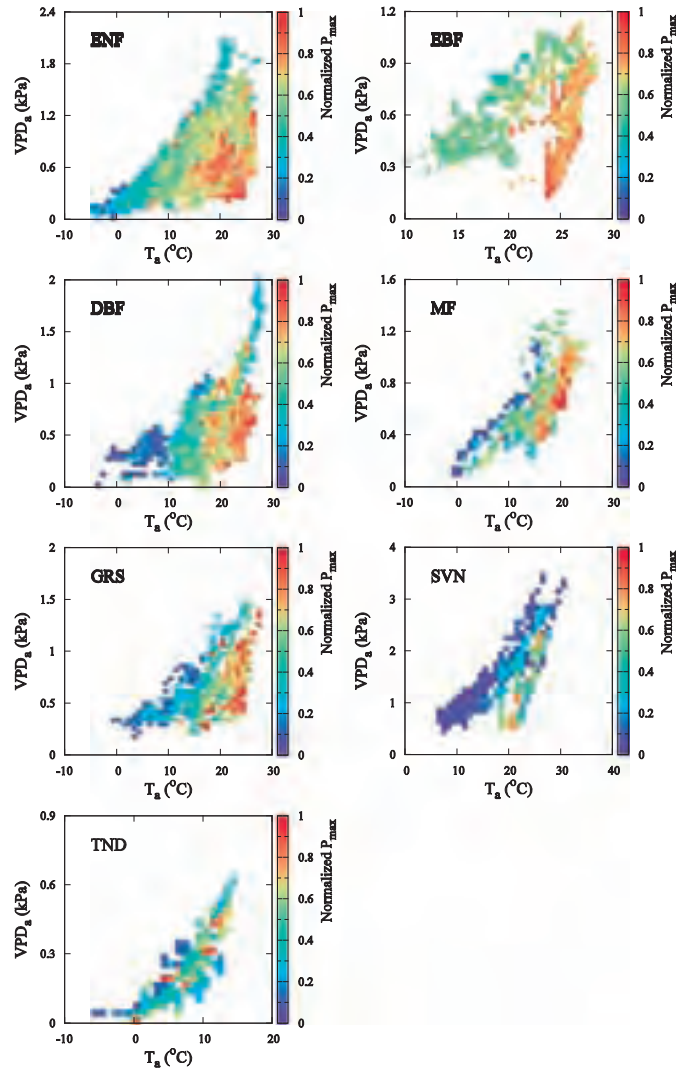


**Figure 4.1** Dependence of normalized  $P_{\max}$  on daily mean air temperature ( $T_a$ ; °C) and vapor pressure deficit ( $VPD_a$ ; kPa) over 15-day periods for seven biomes. The daily values of  $P_{\max}$  were normalized by the maximum  $P_{\max}$  at the site, and were then aggregated for each biome. The normalized values of  $P_{\max}$  in each grid are averages corresponding to the range of  $T_a$  and  $VPD_a$ , and the magnitudes of these are represented in color.

**Table 4.2** List of biome-specific parameter values.

Types	Terms	Eq. (3)			Eq. (4)		Eq. (6)		Eq. (7)		Eq. (8)	
		$T_{\max}$	$T_{\min}$	$T_{\text{opt}}$	$a_{FV}$	$b_{FV}$	$a_{PM}$	$b_{PM}$	$a_{\text{Ini}}$	$b_{\text{Ini}}$	$RE_{\text{ref}}$	$Q_{10}$
	Units	°C	°C	°C	kPa	—	$\mu\text{mol CO}_2$ $\text{m}^{-2} \text{s}^{-1}$	$(\text{g C m}^{-2})^{-1}$	$(\mu\text{mol photon m}^{-2} \text{s}^{-1})^{-1}$	$\mu\text{mol CO}_2$ $(\mu\text{mol photon})^{-1}$	$\mu\text{mol CO}_2$ $\text{m}^{-2} \text{s}^{-1}$	
ENF		41	1	25	3.78	0.73	14.85	0.0013	0.00075	0.0059	1.48	1.91
EBF		43	2	28	2.14	0.73	11.03	0.0015	0.0014	-0.0058	1.55	2.32
DBF		41	1	25	1.87	0.52	34.64	0.0004	0.00078	0.008	1.88	1.62
MF		40	0	23	3.28	0.60	4.21	0.0045	0.0012	0.0003	1.24	1.61
GRS		40	3	25	1.60	0.56	16.03	0.0013	0.00082	0.0059	1.51	1.94
SVN		40	9	28	1.11	1.55	8.82	0.0043	0.0009	0.0028	0.25	3.36
TND		26	-3	15	0.59	0.60	2.06	0.0108	0.0011	0.0048	0.96	1.49

The seasonal course of  $P_{\max}$  was correlated with those of temperature and VPD for each biome, and the strength of the correlations with these environmental factors differed among biomes. Figure 4.1 shows the normalized  $P_{\max}$  under different daily mean air temperatures  $T_a$  (°C) and VPD<sub>a</sub> (kPa) averaged over a 15-day period, consistent with that used in the fitting of Eq. (1). The value of  $P_{\max}$  was normalized by the maximum  $P_{\max}$  at the site over the entire period analyzed. The largest values of the normalized  $P_{\max}$  occurred in each biome, except for TND, when  $T_a$  was approximately between 20°C and 25°C, and VPD<sub>a</sub> was lower than 1 kPa. Although scatter exists, the normalized  $P_{\max}$  for each biome decreased with decreasing  $T_a$  and increasing VPD<sub>a</sub>. On the basis of the variability in the normalized  $P_{\max}$  shown in Figure 4.1, and in the interest of reducing the number of parameters and using meteorological data that were readily available everywhere, we expressed  $P_{\max}$  as a function of the environmental variables of air temperature and VPD as follows:

$$P_{\max} = P_{\max}^{\text{PM}} \cdot F_T \cdot F_V \quad \text{Equation (2)}$$

where  $P_{\max}^{\text{PM}}$  is the potential maximum value of  $P_{\max}$  under unstressed conditions, and  $F_T$  and  $F_V$  denote the coefficient functions for air temperature and VPD, respectively. We used the following equations to express  $F_T$  and  $F_V$ , respectively:

$$F_T = \frac{(T_a - T_{\max})(T_a - T_{\min})}{(T_a - T_{\max})(T_a - T_{\min}) - (T_a - T_{\text{opt}})^2} \quad \text{Equation (3)}$$

$$F_V = \left[ \frac{1}{1 + (\text{VPD}_a / a_{\text{FV}})^{b_{\text{FV}}}} \right] \quad \text{Equation (4)}$$

where  $T_{\max}$ ,  $T_{\min}$ , and  $T_{\text{opt}}$  are the maximum, minimum, and optimum temperatures (°C), respectively, for photosynthesis, and  $a_{\text{FV}}$  (kPa) and  $b_{\text{FV}}$  are constant coefficients.  $a_{\text{FV}}$  is the value of VPD when  $F_V = 0.5$ . The parameter values of  $T_{\max}$ ,  $T_{\min}$ ,  $T_{\text{opt}}$ ,  $a_{\text{FV}}$ , and  $b_{\text{FV}}$  were determined for each biome by fitting the normalized  $P_{\max}$  to Eqs. (3) and (4) using the nonlinear least-squares method (Table 4.2). An example of the fitting is shown in Figure 4.2 for ENFs.

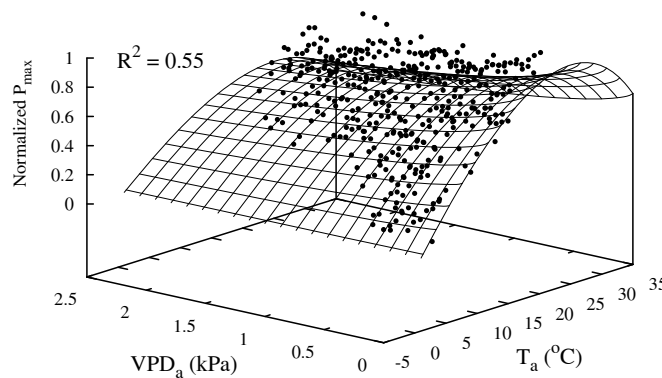


**Figure 4.2 Normalized  $P_{\max}$  in evergreen needle-leaf forests (ENF) under different conditions of  $T_a$  (°C) and VPD<sub>a</sub> (kPa).** The solid circles corresponds to grids shown in Figure 4.1, and the response surface fit of Eqs. (3) and (4) using the nonlinear least squares method.

To formulate  $P_{\max}^{\text{PM}}$  in Eq. (2), all daily  $P_{\max}$  obtained by fitting Eq. (1) with observed CO<sub>2</sub> flux data were divided by  $F_T$  and  $F_V$ , and then the annual maximum value of unstressed  $P_{\max}$  was selected for each ecosystem site from among the data observed under conditions when  $T_a$  was  $\pm 5^\circ\text{C}$  in  $T_{\text{opt}}$ . To avoid uncertainty in the value of  $P_{\max}$  due to random flux measurement error, a computed unstressed maximum  $P_{\max}$  was averaged for the 7-day period around the maximum day. This value was defined as  $P_{\max}^{\text{PM}}$ . Next,  $P_{\max}^{\text{PM}}$  was approximated as a function of annual NPP, assuming that the maximum value of  $P_{\max}$  was proportional to the annual NPP. Annual NPP ( $\text{g C m}^{-2} \text{y}^{-1}$ ) for each site was estimated using the Miami model (Lieth, 1975), as follows:

$$\begin{aligned} \text{NPP}(\text{AMT}, \text{AP}) &= \min\{\text{NPP}_T(\text{AMT}), \text{NPP}_h(\text{AP})\}; \\ \text{NPP}_T(\text{AMT}) &= \frac{1350}{1 + \exp(1.315 - 0.119 \cdot \text{AMT})}, \\ \text{NPP}_h(\text{AP}) &= 1350(1 - \exp(-0.000664 \cdot \text{AP})) \end{aligned} \quad \text{Equation (5)}$$

where AMT is annual mean temperature ( $^\circ\text{C}$ ) and AP is annual precipitation (mm). The unstressed maximum  $P_{\max}$  (i.e.,  $P_{\max}^{\text{PM}}$ ) computed from the observed CO<sub>2</sub> flux data increased substantially with increasing NPP (Figure 4.3). This  $P_{\max}^{\text{PM}}$  dependence on NPP was found for all biomes examined.  $P_{\max}^{\text{PM}}$  was defined as follows:

$$P_{\max}^{\text{PM}} = a_{\text{PM}} \exp(b_{\text{PM}} \cdot \text{NPP}) \quad \text{Equation (6)}$$

where  $a_{\text{PM}}$  ( $\mu\text{mol CO}_2 \text{ m}^{-2} \text{ s}^{-1}$ ) and  $b_{\text{PM}}$  ( $(\text{g C m}^{-2} \text{ y}^{-1})^{-1}$ ) are constant coefficients empirically determined for each biome by the least-squares method (Table 4.2).

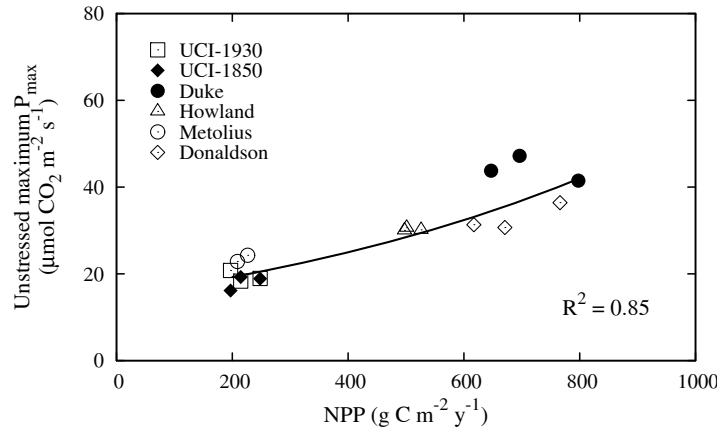


**Figure 4.3 Relationship between annual NPP and unstressed maximum  $P_{\max}$  in evergreen needle-leaf forests.** Sites are indicated as follows: open squares, UCI-1930 burn; solid diamonds, UCI-1850 burn; solid circles, Duke Forest loblolly pine; open triangles, Howland forest; open circles, Metolius; and open diamonds Slashpine-Donaldson, for each year. The solid line is the regression curve. The square of the correlation coefficient  $R^2$  was determined by the least squares method.



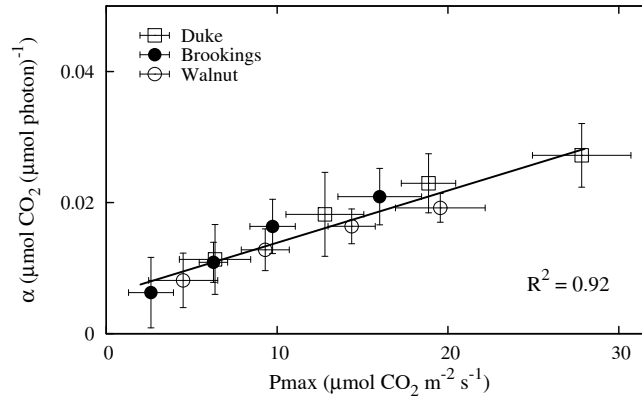


**Figure 4.4 Relationship between bin-averaged  $P_{\max}$  and initial slope  $\alpha$  in grassland.** Sites are indicated as follows: open squares, Duke forest open field; solid circles, Brookings; and open circles, Walnut River Watershed. The solid line is the regression curve, and error bars represent standard deviation from the mean.

The initial slope  $\alpha$  in Eq. (1) shows the complicated seasonal course of the light response curve and of  $P_{\max}$ , as shown in previous studies (e.g., Gilmanov et al., 2003). Owen et al. (2007) have shown that  $\alpha$  can be expressed as a linear function of canopy  $\text{CO}_2$  uptake capacity. Similarly, we found that seasonal variation in  $\alpha$  was correlated with that in  $P_{\max}$  (Figure 4.4). Therefore, we defined  $\alpha$  as a linear function of  $P_{\max}$ :

$$\alpha = a_{\text{Ini}} \cdot P_{\max} + b_{\text{Ini}} \quad \text{Equation (7)}$$

where  $a_{\text{Ini}}$  and  $b_{\text{Ini}}$  are also constant coefficients empirically determined for each biome by the least-squares method (Table 4.2).

RE is the sum of autotrophic plant respiration and heterotrophic soil respiration, and is usually expressed as a function of soil temperature (e.g., Falge et al., 2001). It has been further argued that RE varies with differences in short- and long-term temperature sensitivities (Reichstein et al., 2005), the start of the wet season and the timing of rain events (Xu and Baldocchi, 2004), differences in temperature sensitivities among ecosystem sites, even in the same biome (Gilmanov et al., 2007), and photosynthetic rate (Sampson et al., 2007). Accordingly, we can expect that seasonal variation in RE is in part site-specific, so universal attributes are difficult to formulate with a single equation. However, for application over large areas covering numerous biomes, a simple model driven by limited input data is required. We therefore used a traditional exponential relationship between RE and temperature as:

$$\text{RE} = \text{RE}_{\text{ref}} Q_{10}^{(T_a - 10)/10} \quad \text{Equation (8)}$$

where  $\text{RE}_{\text{ref}}$  is the ecosystem respiration rate ( $\mu\text{mol CO}_2 \text{ m}^{-2} \text{ s}^{-1}$ ) when  $T_a = 10^\circ\text{C}$ , and  $Q_{10}$  represent the temperature sensitivity of RE. The values of  $\text{RE}_{\text{ref}}$  and  $Q_{10}$  were empirically determined for each biome by fitting all available RE data, estimated in the fitting of Eq. (1), to Eq (8) using the least-squares method (Table 4.2).

To summarize the approach used for modeling diurnal variations in NEE presented in the section above, all parameters required to operate the model involve only four variables: air temperature, VPD, annual precipitation, and PPFD. In applying the model, the parameters  $P_{\max}$  and  $\alpha$  in the nonrectangular hyperbola are estimated by using Eqs. (2) and (7) for each

day, whereas the value of  $P_{\max}^{\text{PM}}$  in Eq. (2) is determined for each year using Eq. (6). Hence, diurnal variation in gross primary production (GPP) – the first term on the right-hand side in Eq. (1) – is attributed to changes in the diurnal course of PPFD, as obtained from local observations. On the other hand, RE is estimated for every half-hour or hourly time step, both during the day and at night, with local observed air temperature data in place of  $T_a$  in Eq. (8). This assumes that the half-hour or hourly temperature response of RE is the same as that in the 15-day period, the temperature of which was used as the representative mean temperature to determine the empirical coefficients in Eq. (8). In general, the temperature response of RE is determined using nocturnal eddy covariance CO<sub>2</sub> flux data, and this nocturnal temperature dependence is extrapolated to daytime (e.g., Goulden et al., 1996; Falge et al., 2002). However, nocturnal eddy covariance surface fluxes calculated using typical averaging times of about 30 min generally exhibit large scatter because of measurement error by mesoscale motion, since the cospectral gap, which separates turbulence and mesoscale contributions, is commonly located at a time scale of a few minutes or less during the nocturnal period (e.g., Vickers and Mahrt, 2003). Therefore, we extrapolated the daytime temperature dependence of RE to the night-time dependence (e.g., Suyker and Verma, 2001; Gilmanov et al., 2003).

### 4.2.3 Validation data

To examine model validity, we used higher-quality Level 4 products of 10 AmeriFlux ecosystem sites (Table 4.3). Only the data not used in model construction were selected here. Half-hourly air temperature, VPD, and annual precipitation, used as input data to operate the model, and variability in observed NEE were obtained from Level 4 products, while PPFD data were obtained from quality-checked Level 3 products, since Level 4 does not contain PPFD data.

**Table 4.3 List of AmeriFlux eddy covariance measurement sites used for validation.**

Site	Year	AMT (°C)	AP (mm)
<b>ENF</b>			
UCI-1930 burn site	2005	-1.3	882
Howland forest	2001	7.2	524
Slashpine-Donaldson	2001	19.7	1047
<b>EBF</b>			
Florida-Kennedy Space Center	2002	21.2	932
<b>DBF</b>			
Harvard Forest EMS Tower	2004	7.6	1175
Missouri Ozark Site	2007	13.7	645
<b>MF</b>			
Mature red pine	2002	6.4	640
<b>GRS</b>			
Brookings	2004	7.6	831
<b>SVN</b>			
Audubon Research Ranch	2003	16.5	353
<b>TND</b>			
Barrow	1999	-11.3	94

We also ran the model using the AsiaFlux network data (Fukushima, 2002) to check the simulation performance of the model in regions other than North America. For this check, data from four selected sites, which are located in ENF, EBF, DBF, and MF, were used.

## 4.3 Results and discussion

### 4.3.1 Variations in parameters among biomes

We examined the relationships between estimated annual NPP and unstressed maximum  $P_{\max}$  at all sites (Figure 4.5a). Increasing NPP was correlated with increasing unstressed maximum  $P_{\max}$ , regardless of the biome type. Since NPP is estimated using annual mean temperature or annual precipitation, this result suggests that canopy assimilation capacity, to a large degree, depends on temperature and water conditions at the measurement sites. The NPP response of the unstressed maximum  $P_{\max}$  varied among biomes: the unstressed maximum  $P_{\max}$  in TND ecosystems was most sensitive to NPP, and that in DBFs was least sensitive (Table 4.2 and Figure 4.5a). The low values of  $R^2$  may be mainly associated with the limited amount of available data, and additional datasets covering various ranges in temperature and precipitation would improve the estimate of unstressed maximum  $P_{\max}$ .

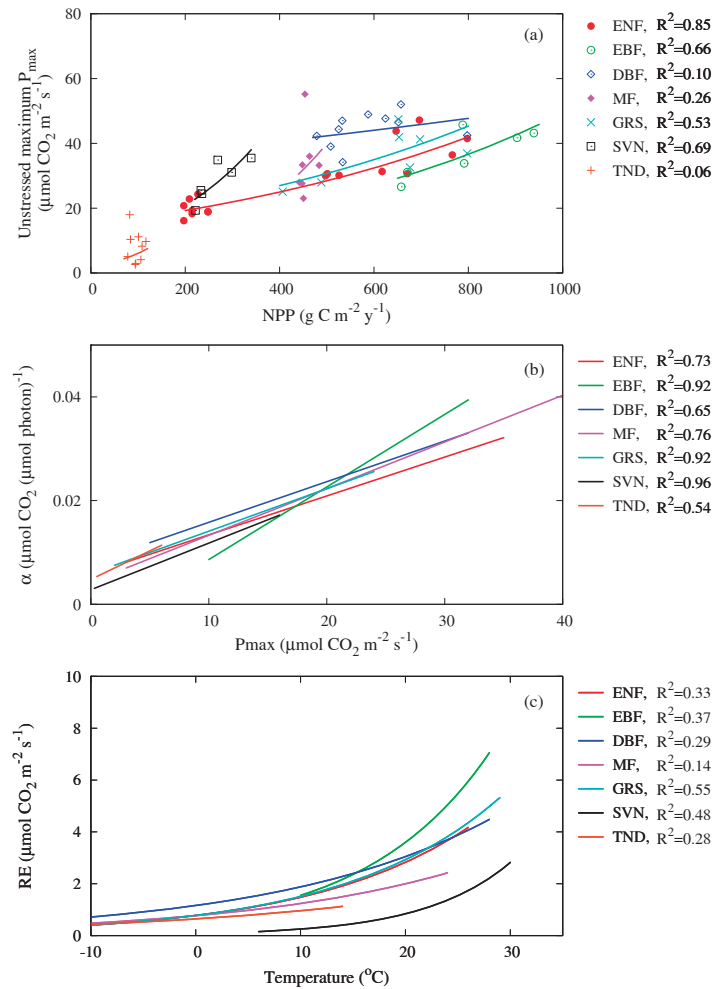


**Figure 4.5 Distributions of three parameters for seven biomes.** (a) Same as Figure 4.3, but for all biomes analyzed, (b) relationships between  $P_{\max}$  and  $\alpha$ , and (c) between temperature and RE. Red: evergreen needle-leaf forests (ENF); green: evergreen broadleaf forests (EBF); blue: deciduous broadleaf forests (DBF); magenta: mixed forests (MF); light blue: grass lands (GRS); black: savanna (SVN); and orange: tundra (TND).

We plotted regression lines of  $\alpha$ , estimated as a linear function of  $P_{\max}$ , for every biome (Figure 4.5b). At the leaf level, previous studies (e.g., Ehleringer and Björkman, 1977; Ehleringer and Pearcy, 1983) have shown that  $\alpha$  is nearly universally the same among unstressed plants. At the canopy level in the current analyses, however, for the seven biomes showed clear seasonal variations; these may result from seasonal changes in the canopy including physiological development and changes in leaf area index (LAI). A remarkable point in Figure 4.5b is the similarities in the correlation between  $P_{\max}$  and  $\alpha$  for all biomes analyzed. This result suggests that the relationship between  $P_{\max}$  and  $\alpha$  may be universal, regardless of biome type. A similar result has been reported by Owen et al. (2007). However, little information is available on the physiological mechanisms behind the general relationship between  $\alpha$  and  $P_{\max}$ , and the similarities in the correlation between  $\alpha$  and  $P_{\max}$  may, in part, be the result of poor fitting in Eq. (1). In the following analyses we therefore used the individual regression lines estimated for each biome (see Table 4.2).

The relationships between temperature and RE for the seven biomes are shown in Figure 4.5c. The sensitivities of RE to temperature varied among biomes. SVN had the highest temperature response ( $Q_{10}=3.36$ ), and the lowest response was found in TND ( $Q_{10}=1.49$ ) (Table 4.2). Tjoelker et al. (2001) reported that the  $Q_{10}$  value is not constant and declines with increasing temperature for various species, and they represented this fraction in  $Q_{10}$  as a function of temperature. In addition, Curiel Yuste et al. (2004) found that the fraction in  $Q_{10}$  for soil respiration also depends on seasonal patterns of plant activity, such as changes in LAI. Consideration of this seasonality in  $Q_{10}$  may improve RE estimation in the model; however, it would require further investigation of the relationship between the seasonal  $Q_{10}$  course and environmental factors. In this study, therefore, simple temperature dependence and constant  $Q_{10}$  values estimated for each biome were used to represent the diurnal variations in RE at all ecosystem sites.

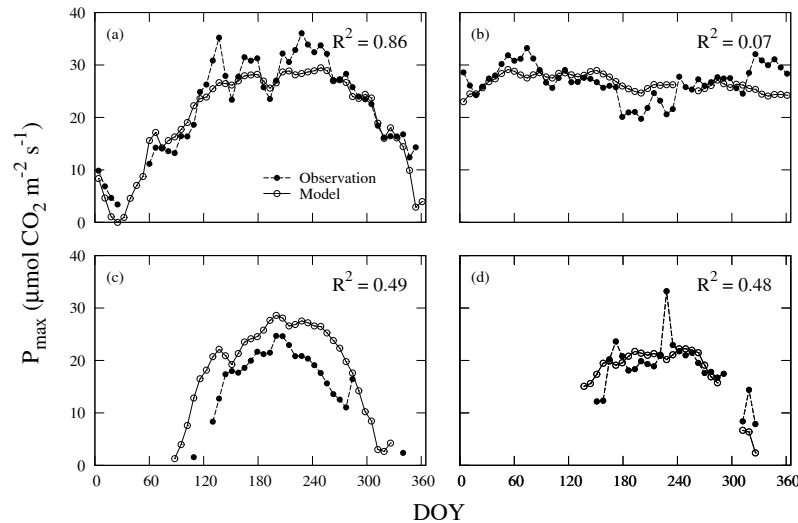


**Figure 4.6** Seasonal course of weekly averaged  $P_{\max}$  at (a) the Duke Forest site, ENF, in 2004; (b) the Santarem site, EBF, in 2003; (c) the Bartlett site, DBF, in 2004; and (d) the mature red pine site, MF, in 2004. The dashed line with closed circles represents  $P_{\max}$  estimated from the observed data, and the solid line with open circles is  $P_{\max}$  predicted using the proposed model. DOY=day of year.

Before comparing the observed and predicted diurnal variations in NEE, we compared the seasonal changes in  $P_{\max}$  (Figure 4.6) and  $\alpha$  (Figure 4.7) computed by the model with the observed changes. Individual points in the graphs are the weekly averaged values of parameters. The seasonal cycle amplitudes of  $P_{\max}$  and  $\alpha$  at the Duke Forest site, an ENF, were larger than those at the other sites. The Santarem site, an EBF, had large values with small amplitudes year round. The results for the DBF and MF sites clearly reflected the existence of both growing and non-growing seasons in a year, while the start and end times of the growing season in the mature red pine site are not shown in the figures because of a lack of data. In contrast, variability of  $P_{\max}$  and  $\alpha$  was always observed at the evergreen sites.

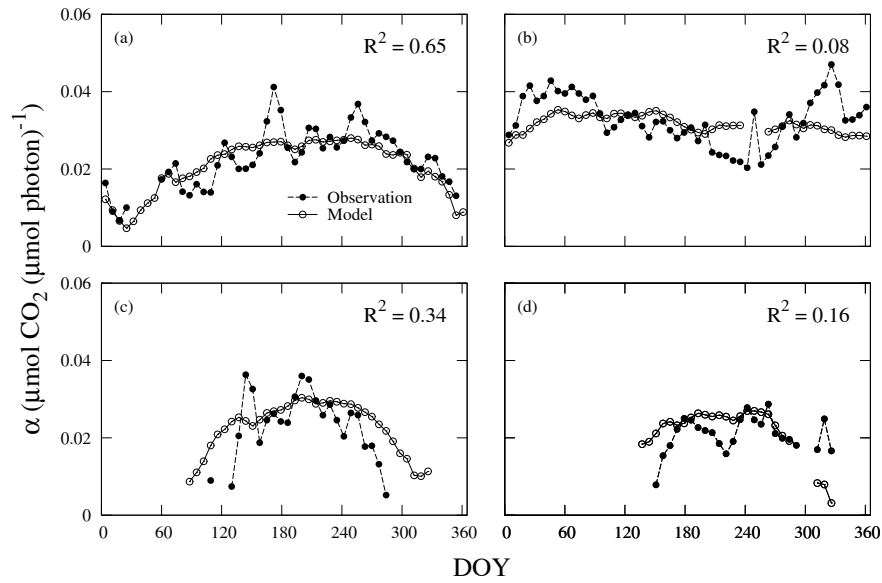


Figure 4.7 Same as Figure 4.6, but for  $\alpha$ .

The seasonal courses of the modeled  $P_{\max}$  and  $\alpha$ , and the magnitudes of these two parameters, showed good agreement with observational data from the Duke Forest site. On the other hand, the model did not account for the seasonality in two parameters at the Santarem site. Small variations in temperature and VPD at the site throughout the year resulted in a smooth and small amplitude in parameters estimated by the model. However, the model captured mean magnitudes of parameters when compared with observed values. For DBF and MF sites, the model captured the seasonality of  $P_{\max}$  and  $\alpha$ , and the approximate timing of the start and end of ecosystem productivity, but overestimates of  $P_{\max}$  were found at the Bartlett site. This overestimation of  $P_{\max}$  during the growing season is due to the overestimated  $P_{\max}^{\text{PM}}$  in Eq. (2), which was estimated from the annual NPP computed using the Miami model. Additional data from new sites may lead to an alteration of the constant coefficients empirically determined for individual parameters.

### 4.3.2 Variations in NEE

Next, to demonstrate the capability of the proposed model, we ran the model for 10 AmeriFlux ecosystem sites with data for a year not used in the model development (Table 4.3). Variations in half-hourly NEE were calculated for all sites during the entire period for

which input meteorological data were available (Figure 4.8). At the Slashpine-Donaldson site, in an ENF, net CO<sub>2</sub> uptake was observed during daytime year round, but at the Howland site in an ENF, NEE was very close to 0  $\mu\text{mol CO}_2 \text{ m}^{-2} \text{ s}^{-1}$  during the period between the end of the year and spring. The model successfully predicted these seasonal variations in NEE; in addition, it predicted the diurnal variations, such as when NEE becomes positive or negative, for both ENF and EBF sites.

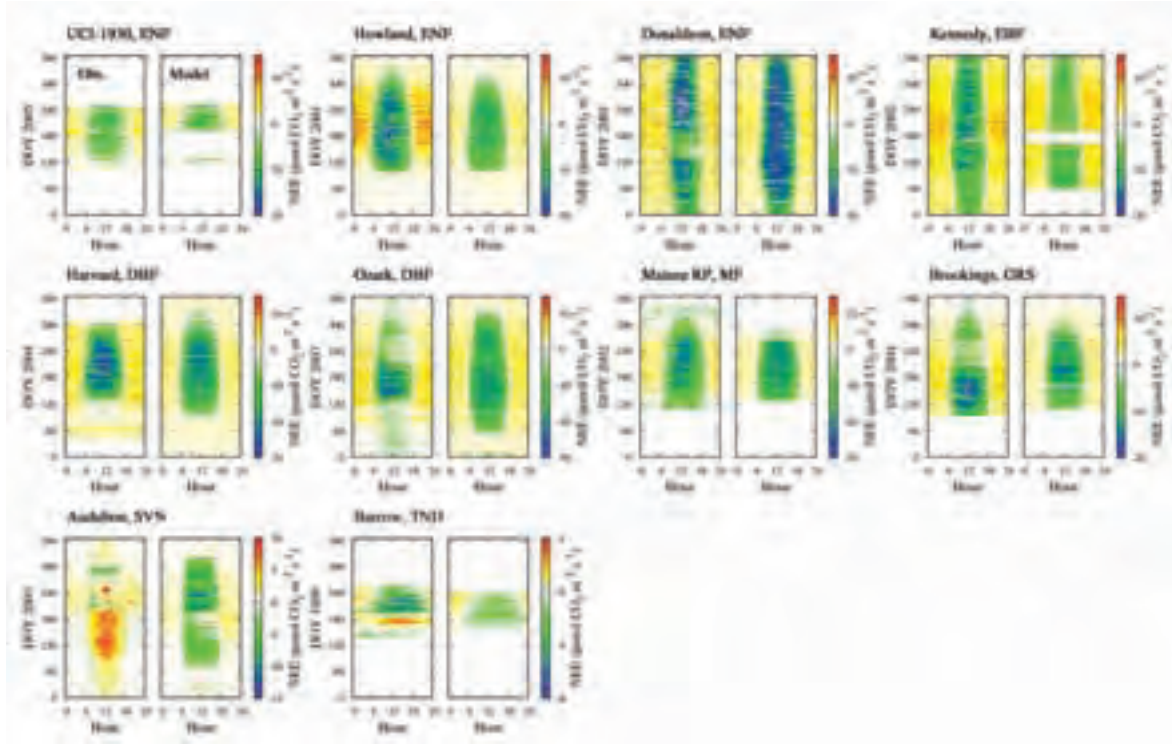


**Figure 4.8** Diurnal and seasonal patterns of observed (left) and predicted (right) NEE at 10 AmeriFlux ecosystem sites. The magnitudes of half-hourly NEE are represented by colors. The blank spaces in the figure, such as the period between DOY 1 and about DOY 100 for the UCI-1930 site, are due to gaps in NEE and meteorological data.

On the other hand, the model underestimated the length of the net CO<sub>2</sub> uptake periods at the Missouri Ozark and Brookings sites (DBF and GRS, respectively), and did not predict the low observed negative NEE during the daytime in winter (Figure 4.8). This is because net CO<sub>2</sub> uptake was observed at both sites, even in winter when  $T_a < 0^\circ\text{C}$ , while the minimum temperatures for photosynthesis in this model were set to  $1^\circ\text{C}$  for DBF and  $3^\circ\text{C}$  for GRS (Table 4.2). Burba et al. (2008) reported that CO<sub>2</sub> flux measured with an open-path gas analyzer can yield unreasonable CO<sub>2</sub> uptake values under low-temperature conditions, due to heating of the instrument body. Differences in NEE between the observations and the model during the winter may result partly from this problem.



**Table 4.4 Slopes (a), intercepts (b), and  $R^2$  values of regression lines,  $y=ax+b$ , between the observed and modeled NEE, and the number of observations (N) at 10 AmeriFlux sites.** The y-axis values are model predictions and the x-axis values are the observations.  $a_{all}$  represents the values calculated from all available half-hourly NEE data, and  $a_{10\text{ day}}$  the values from NEE averaged at half-hourly intervals over 10-day periods.

Site	$a_{all}$	$a_{10\text{ day}}$	$b_{all}$	$b_{10\text{ day}}$	$R^2_{all}$	$R^2_{10\text{ day}}$	$N_{all}$	$N_{10\text{ day}}$
UCI-1930 burn site, ENF	0.79	0.84	-0.25	-0.19	0.84	0.95	3259	390
Howland forest, ENF	0.59	0.63	-0.66	-0.64	0.79	0.90	17518	1728
Slashpine-Donaldson, ENF	0.85	1.00	-2.07	-1.85	0.69	0.83	17424	1728
Florida-Kennedy Space Center, EBF	0.71	0.74	0.74	0.75	0.82	0.91	13408	1392
Harvard Forest EMS Tower, DBF	0.79	0.81	-1.52	-1.44	0.83	0.89	12338	1294
Missouri Ozark Site, DBF	0.90	1.04	-1.64	-1.53	0.55	0.65	17468	1728
Mature red pine, MF	0.82	0.94	-1.37	-0.43	0.72	0.84	7890	864
Brookings, GRS	0.68	0.73	-1.04	-1.02	0.59	0.65	12114	1221
Audubon Research Ranch, SVN	-0.21	-0.29	-0.75	-0.68	0.03	0.05	17376	1728
Barrow, TND	0.10	0.15	-0.32	-0.25	0.13	0.23	4362	480

Overall, the predicted diurnal and seasonal patterns of  $\text{CO}_2$  uptake and release agree with the observed data, except for the SVN at the Audubon Research Ranch and the TND at the Barrow site. For SVN and TND, the model failed in the prediction of NEE variations, especially for SVN. The errors for these two biomes will be revisited later in this section. The degree of model prediction for half-hourly variations in the observed NEE was evaluated by regression analysis. At individual sites, the values of  $R^2$ , slope, and y-intercept were between 0.55 and 0.84, 0.59 and 0.90, and  $-2.07$  and  $0.74$ , respectively (Table 4.4), when all available half-hourly NEE data were used. The model explained only 55% of the half-hourly variations in NEE at the Missouri Ozark site ( $N=17468$ ), but explained 84% of the NEE variations in the UCI-1930 burn site ( $N=3259$ ). These results suggest that differences exist between predicted and observed NEE, and that the degree of agreement is site-dependent. However, the observation records often contain noise that, to some extent, is due to measurement error. To reduce the influence of measurement error and smooth the variability in NEE, the observed and predicted NEE data were averaged for each half-hourly interval over 10-day periods.

The model performance improved considerably when the 10-day averaged half-hourly NEE variations were used (Table 4.4 and Figure 4.9). At six forest sites, except the Missouri Ozark and Brookings sites, the model provided acceptable values of  $R^2$ , ranging between 0.83 and 0.95. The slope of the regression line was 0.63 at the Howland forest site, but this small slope value is partly attributable to model underestimation of RE at night. Indeed, the slope of the regression line was improved to 0.72 at the Howland forest site when only daytime NEE data were used. Nighttime RE will be discussed in the next subsection.



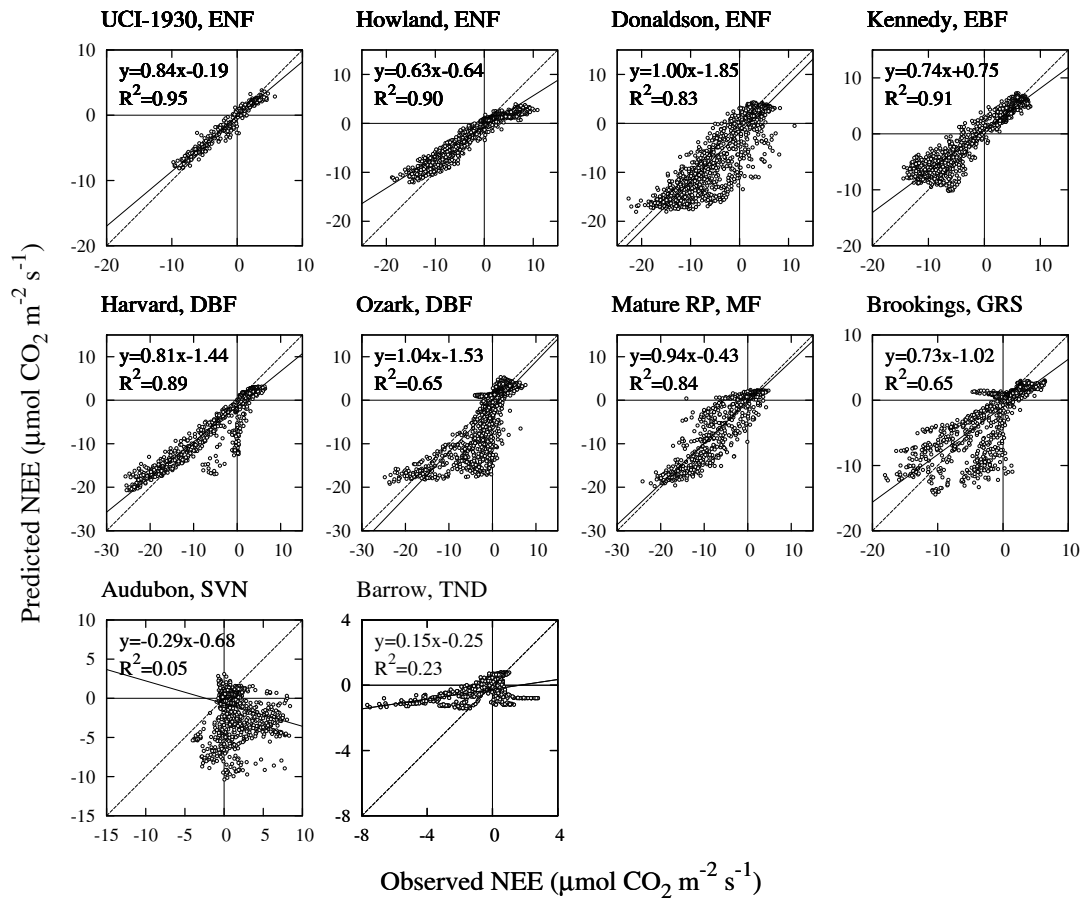


**Figure 4.9 Comparisons between half-hourly variations in observed and predicted NEE, averaged over 10-day periods, at 10 AmeriFlux ecosystem sites.** The open circles represent NEE, solid lines are regression lines, and dashed lines are  $y=x$ .

In contrast to the six forest sites described above, the model explained only 65% of 10-day averaged half-hourly NEE variations at the Missouri Ozark site. A steep net uptake of CO<sub>2</sub> was observed at this site after DOY 120 in 2007, and this net uptake rapidly decreased around DOY 220 (Figure 4.8). However, the model predicted smooth net uptake over the period between DOY 60 and 330, which resulted in large differences between observed and predicted NEE, as shown in Figure 4.9. The rapid changes in amplitude of diurnal NEE variations during the growing season may be mainly associated with the rapid changes in LAI. Moderate Resolution Imaging Spectroradiometer (MODIS) MOD15A2 products indicated that LAI increased from 0.9 on DOY 121 in 2007 to 3.7 on DOY 129, and decreased from 4.2 on DOY 209 to 2.2 on DOY 225, and these drastic variation in LAI seem to be consistent with those in NEE.

The low value of  $R^2$  at the Brookings site ( $R^2=0.65$ ) is attributed, in part, to the low CO<sub>2</sub> uptake observed from DOY 200 to DOY 260 (Figure 4.8). A daytime maximum NEE of  $-11.3 \mu\text{mol CO}_2 \text{ m}^{-2} \text{ s}^{-1}$  was observed for DOY 171–180, but daytime NEE decreased to  $-3.2 \mu\text{mol CO}_2 \text{ m}^{-2} \text{ s}^{-1}$  for DOY 221–230, and increased again to  $-7.6 \mu\text{mol CO}_2 \text{ m}^{-2} \text{ s}^{-1}$  for DOY 261–270. One possible explanation for the low negative NEE observed in this period is disturbance such as grazing and mowing. Grazing intensity markedly affects aboveground

biomass (e.g., Cao et al., 2004) and can thus cause variations in ecosystem productivity. However, the MOD15A2 products did not show drastic changes in LAI during the period from DOY 200 to 260; thus, this pattern remains to be explained.

Daytime NEE observed at the Audubon and Barrow sites varied during the growing season (Figure 4.8). High  $\text{CO}_2$  release was observed at both sites during the daytime around DOY 180, but NEE changed to net  $\text{CO}_2$  uptake a few weeks later. At the Audubon site, analysis of the observation data revealed that the duration of the assimilation period was narrowly restricted to about 100 days, and the seasonal patterns of the physiological parameters were very sharp. These processes were less sensitive to changes in temperature and VPD than in other biomes. Leuning et al. (2005) have shown that the productivity of a SVN ecosystem is controlled almost exclusively by the amount and timing of rainfall during the wet season. Ma et al. (2007) similarly noted that both photosynthesis and respiration processes in SVN depend on the amount of seasonal precipitation. These previous studies suggest that precipitation is the dominant factor controlling SVN ecosystem productivity under drought conditions. Figure 4.10 shows the seasonal courses of LAI from the MOD15A2 products and daily precipitation at the Audubon site in 2003. LAI was nearly constant, ranging from 0.2 to 0.3, during the dry period before DOY 190, but rapidly increased following the rainfall events that occurred frequently after DOY 192. An LAI of 0.3 on DOY 193 increased to 0.8 on DOY 209. Figures 4.8 and 4.10 clearly show that plant development and  $\text{CO}_2$  gas exchange at the Audubon SVN site are mainly limited by water stress, as discussed by Leuning et al. (2005) and Ma et al. (2007).

For the Barrow site, LAI data for 1999 were not available from the MOD15A2 products, and the relationship between LAI and rapid changes in NEE could not be examined. However, Harazono et al. (2003) reported that photosynthetic activity on the flooded Barrow TND is immediately observed after snowmelt, which strongly influences the rapid development of TND vegetation. Although further investigation using local observation data is required, drastic changes in NEE at the Barrow site, shown in Figure 4.8, could be explained by the seasonal course of LAI at the site.

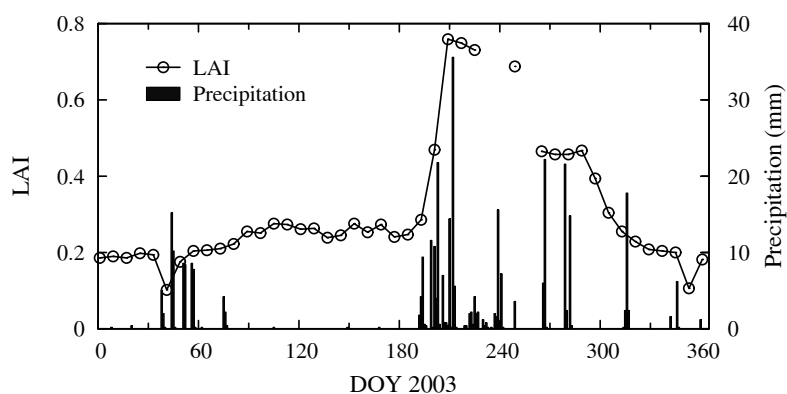


**Figure 4.10** Seasonal courses of LAI, from the MOD15A2 for the areas surrounding the Audubon Research Ranch site, and daily precipitation in 2003. Open circles represent LAI and bars precipitation.

Despite the simplicity of the proposed model and its basis in empirical regression methods driven by four environmental parameters, it performed well for half-hourly

variations in NEE over long periods, particularly for forest biomes. These results indicate that the nonrectangular hyperbola with biome-specific seasonality of physiological parameters can be applied to various biomes to predict diurnal variations in NEE. However, at some of the sites with very rapid changes in LAI, there was poor agreement between observed and predicted NEE. Because the proposed model does not use any plant physiological information to estimate diurnal variations in NEE, the model cannot predict rapid changes in NEE associated with changes in LAI. Yuan et al. (2007) developed a light-use-efficiency model using information from a normalized difference vegetation index (NDVI) that was able to predict seasonal variability in GPP in GRS and SVN biomes. Similarly, Leuning et al. (2005) estimated seasonal variability in a SVN during the wet season using MODIS data. These remote-sensing data products respond directly to changes in overall canopy conditions such as LAI and canopy structure. For future studies, these data may be useful for further improvement of the proposed model.

### 4.3.3 Nocturnal RE

As mentioned above, the model uses the response of daytime ecosystem respiration to temperature to estimate variability between daytime and nighttime RE over the entire period. To demonstrate the ability of the model to predict RE variability, we show the observed and modeled seasonal course of monthly averaged nocturnal RE at the Howland and Donaldson sites (ENF) and the Missouri Ozark site (DBF), for which nocturnal RE data are available over the entire period (Figure 4.11). The model captures the seasonal cycle of nocturnal RE at the Donaldson and Missouri Ozark sites, but the computed amplitudes are somewhat smaller than those of the observation data. For these two sites, the model slightly underestimates RE in summer; the difference between the observations and the model is approximately  $1.7 \mu\text{mol CO}_2 \text{ m}^{-2} \text{ s}^{-1}$ . This discrepancy could be attributed to the simplifying approach of the model. In the interest of constructing the model as simply as possible, RE variability over a year was introduced using a single equation as a function of temperature for each biome, regardless of differences in soil conditions and plant developmental stages. Sampson et al. (2007), for example, demonstrated that there is considerable variability in the temperature dependence of soil respiration associated with seasonal differences in photosynthesis. However, to avoid complexity and obviate the need to obtain additional information on the mechanics of the relationship between RE and photosynthesis, the model does not account for the influence of these physiological activities on RE. On the other hand, as shown by the large error bars in Figure 4.11, it is also clear that the nocturnal eddy covariance data provide large scatter associated with weak turbulence. This noise is mainly due to flux sampling errors, which may, in part, be the cause of the difference between the observed and predicted RE.

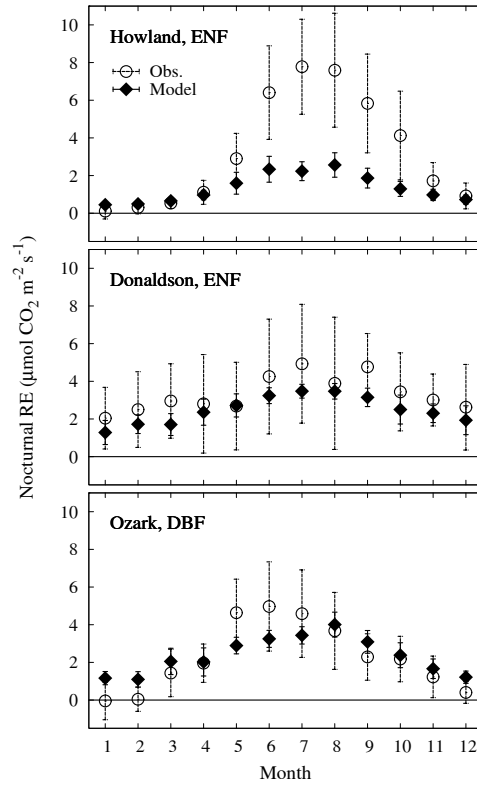


**Figure 4.11** Seasonal course of monthly averaged nocturnal RE at the Howland ENF site in 2001, the Donaldson ENF site in 2001, and the Ozark DBF site in 2007. A dashed line with open circles represents observed data, and a solid line with closed diamonds is the model data. Error bars represent the standard deviation from the mean.

In contrast to the Donaldson and Missouri Ozark sites, modeled nocturnal RE was clearly much lower than observed nocturnal RE at the Howland site during the growing season. The model predicted an average nocturnal RE of  $2.2 \mu\text{mol CO}_2 \text{ m}^{-2} \text{ s}^{-1}$  in July, while the observed data were  $7.8 \mu\text{mol CO}_2 \text{ m}^{-2} \text{ s}^{-1}$ . Air temperature at the Howland site was generally lower than that at the Donaldson site year round, which resulted in the lower predicted RE at the Howland site, since the proposed model estimates RE using the same temperature response for the same biome. However, higher nocturnal RE observed at the Howland site during the growing season compared to that at the Donaldson site led to the model being unable to predict this site-specific variability in RE. This high observed nocturnal RE at the Howland site may, in part, be due to carbon richness of the soil, although no detailed evidence exists to support this proposal. It is important to be aware of the abovementioned problems when computing RE variability using the model.

#### 4.3.4 Application to AsiaFlux ecosystems

To validate the applicability of the proposed empirical model, constructed with the AmeriFlux data sets, to other regions, we applied the model to data obtained from the AsiaFlux network. Details of individual ecosystem sites can be found in Table 4.5. All half-hourly or hourly  $\text{CO}_2$  fluxes were measured at four forest sites using the eddy covariance method. Micrometeorological data such as air temperature and PPFD were also obtained from the AsiaFlux network. The ecosystem-specific parameter values, such as  $T_{\text{max}}$  in Eq. (3) and

$a_{FV}$  in Eq. (4), from the AmeriFlux network listed in Table 4.2 were used without any modifications to estimate variations in half-hourly or hourly NEE in the AsiaFlux forest sites.

**Table 4.5 Same as Table 4.1, but for AsiaFlux eddy covariance measurement sites analyzed.**

Site, country	Year	Latitude, longitude	AMT (°C)	AP (mm)	Reference
<b>ENF</b>					
Fujiyoshida forest meteorology research site, Japan	2000	34.45°N, 138.76°E	9.6	1599	Ohtani et al. (2005)
<b>EBF</b>					
Sakaerat, Thailand	2002	14.29°N, 101.55°E	24.4	1813	Gamo and Panuthai (2005)
<b>DBF</b>					
Mae Klong, Thailand	2003	14.34°N, 98.50°E	24.7	1708	Huete et al. (2008)
<b>MF</b>					
CC-LaG experiment site, Japan	2002	45.03°N, 142.06°E	5.6	973	Takagi et al. (2005)

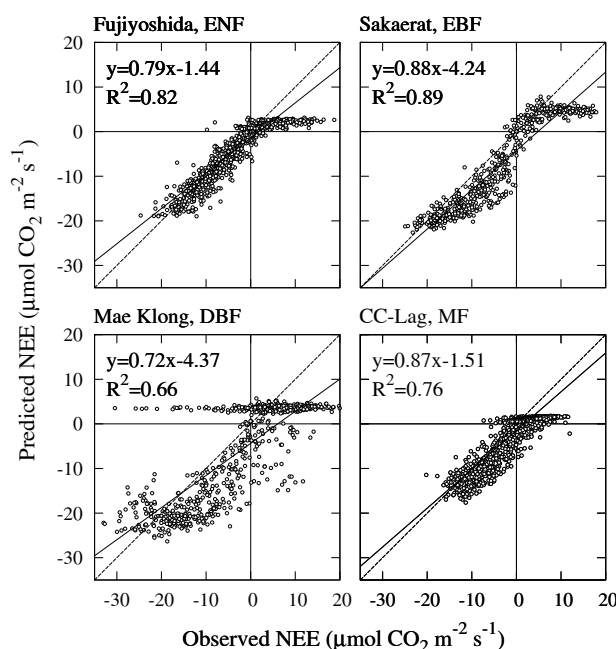


**Figure 4.12 Same as Figure 4.9, but for four AsiaFlux ecosystem sites.**

Figure 4.12 shows comparisons between the observations and model results of 10-day averaged half-hourly or hourly NEE variations at each site, as in Figure 4.9. Overall, the model gave reasonable predictions of NEE variation during the daytime CO<sub>2</sub> uptake period, although scatter was rather large at the Mae Klong DBF site. The values of  $R^2$  at three sites, apart from the Mae Klong site, ranged from 0.76 to 0.89, which are comparable to the results obtained using the model on the AmeriFlux sites. This result suggests that the environmental forces used in this model are critical determinants of photosynthesis in various biomes, and that the biome-specific responses to environmental forces, determined by the AmeriFlux data, may be applicable to other regions. However, it is evident that there was a discrepancy between observed and predicted nocturnal RE, and that the model produced systematic

underestimates. Unfortunately, this study was unable to generalize the variation in RE in response to temperature; therefore, accurate modeling of RE is necessary to substantially improve the model's simulation of long-term diurnal CO<sub>2</sub> exchange.

## 4.4 Conclusions

We explored a simple approach to predicting diurnal variations in NEE over seven biomes and proposed an empirical model based on the use of a nonrectangular hyperbola and eddy covariance flux data obtained from the AmeriFlux network. Physiological parameters in the nonrectangular hyperbola –  $P_{\max}$ ,  $\alpha$  and RE – clearly exhibited seasonal variations. While these seasonal variations were complex,  $P_{\max}$  and  $\alpha$  generally showed a dependence on temperature and VPD, and the degree of this dependence varied among biomes. The study expressed the seasonality in parameters as a function of only environmental variables – air temperature, VPD, and precipitation – for each biome, and diurnal variability in NEE was predicted using these biome-specific parameters together with PPFD. The proposed model successfully predicted the diurnal variability of NEE for almost all forest biomes in the AmeriFlux network over the entire annual observation period. However, the model was unable to account for drastic changes in the magnitude of NEE and CO<sub>2</sub> uptake and release associated with rapid changes in LAI that were mainly observed in SVN and TND ecosystems. The model demonstrated acceptable performance for the AsiaFlux ecosystem sites, although further refinement is needed for RE. Therefore, the approach used in this study should be applicable to many other regions. Adjustment of the methodology used in parameter estimations, application of remote-sensing products, and subdivision of the biome types would further improve the precision of the model.

## Acknowledgements

This study is conducted at the GOSAT project at NIES, Japan. We thank Yanhong Tang at NIES for useful comments on the manuscript, and the AmeriFlux and AsiaFlux networks and the NOAA Earth System Research Laboratory and Pennsylvania State University for providing the data. Data for the Bartlett and Howland sites were provided by the Northeastern States Research Cooperative, under support by the US Department of Energy (DOE) through the Office of Biological and Environmental Research (BER) Terrestrial Carbon Processes (TCP) program (No. DE-AI02-07ER64355) with additional support from the USDA Forest Services Northern Global Change program and Northern Research Station, and those for the Duke sites were supported by the DOE through the BER TCP program (No. 10509-0152, DE-FG02-00ER53015, and DE-FG02-95ER62083).

## References

- Baldocchi, D.D. (2008) “Breathing” of the terrestrial biosphere: lessons learned from a global network of carbon dioxide flux measurement systems. *Aust. J. Bot.*, 56, 1–26.
- Bonan, G.B. (1996) A land surface model (LSM version 1.0) for ecological, hydrological, and atmospheric studies: Technical description and user's guide. NCAR Tech. Note NCAR/TN-417+STR.
- Bonan, G.B. (1998) The land surface climatology of the NCAR Land Surface Model coupled to the NCAR Community Climate Model. *J. Climate*, 11, 1307–1326.



- Burba, G.G., McDermitt, D.K., Grelle, A., Anderson, D.J., Xu, L. (2008) Addressing the influence of instrument surface heat exchange on the measurements of CO<sub>2</sub> flux from open-path gas analyzers. *Glob. Change Biol.*, 14, 1854–1876.
- Cao, G., Tang, Y., Mo, W., Wang, Y., Li, Y., Zhao, X. (2004) Grazing intensity alters soil respiration in an alpine meadow on the Tibetan plateau. *Soil Biol. Biochem.*, 36, 237–243.
- Curiel Yuste, J., Janssens, I.A., Carrara, A., Ceulemans, R. (2004) Annual Q<sub>10</sub> of soil respiration reflects plant phenological patterns as well as temperature sensitivity. *Glob. Change Biol.*, 10, 161–169.
- Dore, S., Hymus, G.J., Johnson, D.P., Hinkle, C.R., Valentini, R., Drake, B.G. (2003) Cross validation of open-top chamber and eddy covariance measurements of ecosystem CO<sub>2</sub> exchange in a Florida scrub-oak ecosystem. *Glob. Change Biol.*, 9, 84–95.
- Ehleringer, J., Björkman, O. (1977) Quantum yield for CO<sub>2</sub> uptake in C<sub>3</sub> and C<sub>4</sub> plants. *Plant Physiol.*, 59, 86–90.
- Ehleringer, J., Pearcy, R.W. (1983) Variation in quantum yield for CO<sub>2</sub> uptake among C<sub>3</sub> and C<sub>4</sub> plants. *Plant Physiol.*, 73, 555–559.
- Epstein, H.E., Calef, M.P., Walker, M.D., Chapin, F.S., Starfield, A.M. (2004) Detecting changes in arctic tundra plant communities in response to warming over decadal time scales. *Glob. Change Biol.*, 10, 1325–1334.
- Eugster, W., Rouse, W.R., Pielke, R.A., McFadden, J.P., Baldocchi, D.D., Kittel, T.G.F., Chapin, F.S., Liston, G. E., Vidale, P.L., Vaganov, E., Chambers, S. (2000) Land-atmosphere energy exchange in Arctic tundra and boreal forest: available data and feedbacks to climate. *Glob. Change Biol.*, 6, 84–115.
- Falge, E., Baldocchi, D., Olson, R., Anthoni, P., Aubinet, M., Bernhofer, C., Burba, G., Ceulemans, R., Clement, R., Dolman, H., et al. (2001) Gap filling strategies for defensible annual sums of net ecosystem exchange. *Agric. Forest Meteorol.*, 107, 43–69.
- Falge, E., Baldocchi, D., Tenhunen, J., Aubinet, M., Bakwin, P., Berbigier, P., Bernhofer, C., Burba, G., Clement, R., Davis, K.J., et al. (2002) Seasonality of ecosystem respiration and gross primary production as derived from FLUXNET measurements. *Agric. Forest Meteorol.*, 113, 53–74.
- Farquhar, G.D., von Caemmerer, S., Berry, J.A. (1980) A biochemical model of photosynthetic CO<sub>2</sub> assimilation in leaves of C<sub>3</sub> species. *Planta*, 149, 78–90.
- Fukushima, Y. (2002) Perspective of AsiaFlux. *AsiaFlux Newsletter*, 2, 1–2.
- Fung, I.Y., Tucker, C.J., Prentice, K.C. (1987) Application of Advanced Very High Resolution Radiometer vegetation index to study atmosphere-biosphere exchange of CO<sub>2</sub>. *J. Geophys. Res.*, 92, 2999–3015.
- Gamo, M., Panuthai, S. (2005) Carbon flux observation in the tropical seasonal evergreen forest in Sakaerat, Thailand. *AsiaFlux Newsletter*, 14, 4–6.
- Gholz, H.L., Clark, K.L. (2002) Energy exchange across a chronosequence of slash pine forests in Florida. *Agric. Forest Meteorol.*, 112, 87–102.
- Gilmanov, T.G., Verma, S.B., Sims, P.L., Meyers, T.P., Bradford, J.A., Burba, G.G., Suyker, A.E. (2003) Gross primary production and light response parameters of four Southern Plains ecosystems estimated using long-term CO<sub>2</sub>-flux tower measurements. *Global Biogeochem. Cy.*, 17, 1071, doi:10.1029/2002GB002023.
- Gilmanov, T.G., Tieszen, L.L., Wylie, B.K., Flanagan, L.B., Frank, A.B., Haferkamp, M.R., Meyers, T.P., Morgan, J.A. (2005) Integration of CO<sub>2</sub> flux and remotely-sensed data for primary production and ecosystem respiration analyses in the Northern Great Plains: potential for quantitative spatial extrapolation. *Global Ecol. Biogeogr.*, 14, 271–292.
- Gilmanov, T.G., Soussana, J.F., Aires, L., Ammann, C., Balzarola, M., Barcza, Z., Bernhofer, C., Campbell, C. L., Cernusca, A., Cescatti, A., et al. (2007) Partitioning European grassland net ecosystem CO<sub>2</sub> exchange into gross primary productivity and ecosystem respiration using light response function analysis. *Agr. Ecosyst. Environ.*, 121, 93–120.
- Goulden, M.L., Munger, J.W., Fan, S.M., Daube, B.C., Wofsy, S.C. (1996) Measurements of carbon sequestration by longterm eddy covariance: methods and a critical evaluation of accuracy. *Glob. Change Biol.*, 2, 169–182.



- Gu, L., Meyers, T., Pallardy, S.G., Hanson, P.J., Yang, B., Heuer, M., Hosman, K.P., Riggs, J.S., Sluss, D., Wullschlegel, S.D. (2006) Direct and indirect effects of atmospheric conditions and soil moisture on surface energy partitioning revealed by a prolonged drought at a temperate forest site. *J. Geophys. Res.*, 111, D16102, doi:10.1029/2006JD007161.
- Harazono, Y., Mano, M., Miyata, A., Zulueta, R.C., Oechel, W.C. (2003) Inter-annual carbon dioxide uptake of a wet sedge tundra ecosystem in the Arctic. *Tellus B*, 55, 215–231.
- Hargrove, W.W., Hoffman, F.M., Law, B.E. (2003) New analysis reveals representativeness of AmeriFlux network. *Eos Trans. AGU*, 84(48), 529 pp.
- Hirata, R., Saigusa, N., Yamamoto, S., Ohtani, Y., Ide, R., Asanuma, J., Gamo, M., Hirano, T., Kondo, H., Kosugi, Y., et al. (2008) Spatial distribution of carbon balance in forest ecosystems across East Asia. *Agric. Forest Meteorol.*, 148, 761–775.
- Hollinger, D.Y., Aber, J., Dail, B., Davidson, E.A., Goltz, S.M., Hughes, H., Leclerc, M., Lee, J.T., Richrdson, A.D., Rodrigues, C., et al. (2004) Spatial and temporal variability in forest-atmospheric CO<sub>2</sub> exchange. *Glob. Change Biol.*, 10, 1689–1706.
- Huete, A.R., Restrepo-Coupe, N., Ratana, P., Didan, K., Saleska, S.R., Ichii, K., Panuthai, S., Gamo, M. (2008) Multiple site tower flux and remote sensing comparisons of tropical forest dynamics in Monsoon Asia. *Agric. Forest Meteorol.*, 148, 748–760.
- Jenkins, J.P., Richardson, A.D., Braswell, B.H., Ollinger, S.V., Hollinger, D.Y., Smith, M.L. (2007) Refining light-use efficiency calculations for a deciduous forest canopy using simultaneous tower-based carbon flux and radiometric measurements. *Agric. Forest Meteorol.*, 143, 64–79.
- Johnson, I.R., Thornley, J.H.M. (1984) A model of instantaneous and daily canopy photosynthesis. *J. Theor. Biol.*, 107, 531–545.
- Katul, G., Leuning, R., Oren, R. (2003) Relationship between plant hydraulic and biochemical properties derived from a steady-state coupled water and carbon transport model. *Plant Cell Environ.*, 26, 339–350.
- Katul, G.G., Hsieh, C., Bowling, D., Clark, K., Shurpali, N., Turnipseed, A., Albertson, J., Tu, K., Hollinger, D., Evans, B., Offerle, B., et al. (1999) Spatial variability of turbulent fluxes in the roughness sublayer of an even-aged pine forest. *Bound.-Lay. Meteorol.*, 93, 1–28.
- Kosugi, Y., Tanaka, H., Takanashi, S., Matsuno, N., Ohta, N., Shibata, S., Tani, M. (2005) Three years of carbon and energy fluxes from Japanese evergreen broad-leaved forest. *Agric. Forest Meteorol.*, 132, 329–343.
- LeMone, M.A., Grossman, R.L., McMillen, R.T., Liou, K.N., Ou, S.C., McKeen, S., Angevine, W., Ikeda, K., Chen, F. (2002) Cases-97: Late-morning warming and moistening of the convective boundary layer over the Walnut River Watershed. *Bound.-Lay. Meteorol.*, 104, 1–52.
- Leuning, R., Cleugh, H.A., Zegelin, S.J., Hughes, D. (2005) Carbon and water fluxes over a temperate Eucalyptus forest and a tropical wet/dry savanna in Australia: measurements and comparison with MODIS remote sensing estimates. *Agric. Forest Meteorol.*, 129, 151–173.
- Lieth, H. (1975) Modeling the primary productivity of the world. in: *Primary Productivity of the Biosphere*, edited by: Lieth, H. and Whittaker, R.H., Springer-Verlag, 237–263.
- Ma, S., Baldocchi, D.D., Xu, L., Hehn, T. (2007) Inter-annual variability in carbon dioxide exchange of an oak/grass savanna and open grassland in California. *Agric. Forest Meteorol.*, 147, 157–171.
- Martens, C.S., Shay, T.J., Mendlovitz, H.P., Matross, D.M., Saleska, S.R., Wofsy, S.C., Woodward, W.S., Menton, M.C., De Moura, J.M.S., Crill, P.M., et al. (2004) Radon fluxes in tropical forest ecosystems of Brazilian Amazonia: night-time CO<sub>2</sub> net ecosystem exchange derived from radon and eddy covariance methods. *Glob. Change Biol.*, 10, 618–629.
- McMillan, A.M.S., Winston, G.C., Goulden, M.L. (2008) Agedependent response of boreal forest to temperature and rainfall variability. *Glob. Change Biol.*, 14, 1904–1916.
- Monteith, J.L. (1972) Solar radiation and productivity in tropical ecosystems. *J. Appl. Ecol.*, 9, 747–766.
- Nemry, B., Francois, L., G'érard, J.C., Bondeau, A., Heimann, M., and the participants of the Potsdam NPP Model Intercomparison (1999) Comparing global models of terrestrial net primary productivity (NPP): analysis of the seasonal atmospheric CO<sub>2</sub> signal. *Glob. Change Biol.*, 5, 65–76.

- Ohtani, Y., Mizoguchi, Y., Watanabe, T., Yasuda, Y. (2005) Parameterization of NEP for gap-filling in a cool-temperate coniferous forest in Fujiyoshida, Japan. *Journal of Agricultural Meteorology*, 60(5), 769–772.
- Owen, K.E., Tenhunen, J., Reichstein, M., Wang, Q., Falge, E., Geyer, R., Xiao, X., Stoy, P., Ammann, C., Arain, A., et al. (2007) Linking flux network measurements to continental scale simulations: ecosystem carbon dioxide exchange capacity under non-water-stressed conditions. *Glob. Change Biol.*, 13, 734–760.
- Peat, W.E. (1970) Relationships between photosynthesis and light intensity in the tomato. *Ann. Bot.-London*, 34, 319–328.
- Potter, C.S., Randerson, J.T., Field, C.B., Matson, P.A., Vitousek, P.M., Moonet, H.A., Klooster, S.A. (1993) Terrestrial ecosystem production: a process model based on global satellite and surface data. *Global Biogeochem. Cy.*, 7, 811–841.
- Rabinowitch, E.I. (1951) *Photosynthesis and Related Processes*. Interscience Publishers.
- Randerson, J.T., Thompson, M.V., Conway, T.J., Fung, I.Y., Field, C.B. (1997) The contribution of terrestrial sources and sinks to trends in the seasonal cycle of atmospheric carbon dioxide. *Global Biogeochem. Cy.*, 11, 535–560.
- Reichstein, M., Falge, E., Baldocchi, D., Papale, D., Aubinet, M., Berbigier, P., Bernhofer, C., Buchmann, N., Gilmanov, T., Granier, A., et al. (2005) On the separation of net ecosystem exchange into assimilation and ecosystem respiration: review and improved algorithm. *Glob. Change Biol.*, 11, 1424–1439.
- Ruimy, A., Dedieu, G., Saugier, B. (1996) TURC: a diagnostic model of continental gross primary productivity and net primary productivity. *Global Biogeochem. Cy.*, 10, 269–285.
- Saigusa, N., Yamamoto, S., Hirata, R., Ohtani, Y., Ide, R., Asanuma, J., Gamo, M., Hirano, T., Kondo, H., Kosugi, Y., et al. (2008) Temporal and spatial variations in the seasonal patterns of CO<sub>2</sub> flux in boreal, temperate, and tropical forests in East Asia. *Agric. Forest Meteorol.*, 148, 700–713.
- Sampson, D.A., Janssens, I.A., Curiel Yuste, J., Ceulemans, R. (2007) Basal rates of soil respiration are correlated with photosynthesis in a mixed temperate forest. *Glob. Change Biol.*, 13, 2008–2017.
- Schwarz, P.A., Law, B.E., Williams, M., Irvine, J., Kurpius, M., Moore, D. (2004) Climatic versus biotic constraints on carbon and water fluxes in seasonally drought-affected ponderosa pine ecosystems. *Global Biogeochem. Cy.*, 18, GB4007, doi:10.1029/2004GB002234.
- Sellers, P.J., Mintz, Y., Sub, Y.C., Dalcher, A. (1986) A simple biosphere model (SiB) for use within general circulation models. *J. Atmos. Sci.*, 43, 305–331.
- Suyker, A.E., Verma, S.B. (2001) Year-round observations of the net ecosystem exchange of carbon dioxide in a native tallgrass prairie. *Glob. Change Biol.*, 7, 279–289.
- Takagi, K., Nomura, M., Ashiya, D., Takahashi, H., Sasa, K., Fujinuma, Y., Shibata, H., Akibayashi, Y., Koike, T. (2005) Dynamic carbon dioxide exchange through snowpack by wind-driven mass transfer in a conifer-broadleaf mixed forest in northernmost Japan. *Global Biogeochem. Cy.*, 19, GB2012, doi:10.1029/2004GB002272.
- Thornley, J.H.M. (2002) Instantaneous Canopy Photosynthesis: Analytical Expressions for Sun and Shade Leaves Based on Exponential Light Decay Down the Canopy and an Acclimated Non-rectangular Hyperbola for Leaf Photosynthesis. *Ann. Bot.-London*, 81, 451–458.
- Tjoelker, M.G., Oleksyn, J., Reich, P.B. (2001) Modelling respiration of vegetation: evidence for a general temperature-dependent Q<sub>10</sub>. *Glob. Change Biol.*, 7, 223–230.
- Vickers, D., Mahrt, L. (2003) The cospectral gap and turbulent flux calculations. *J. Atmos. Ocean Tech.*, 20, 660–672.
- Wang, C.K., Bond-Lamberty, B., Gower, S.T. (2003) Carbon distribution of a well- and poorly-drained black spruce fire chronosequence. *Glob. Change Biol.*, 9, 1066–1079.
- Xu, L., Baldocchi, D.D. (2004) Seasonal variation in carbon dioxide exchange over a Mediterranean annual grassland in California. *Agric. Forest Meteorol.*, 123, 79–96.
- Yi, C. X., Davis, K.J., Berger, B.W., Bakwin, P.S. (2001) Long-term observations of the dynamics of the continental planetary boundary layer. *J. Atmos. Sci.*, 58, 1288–1299.

Yuan, W., Liu, S., Zhou, G., Zhou, G., Tieszen, L.L., Baldocchi, D., Bernhofer, C., Gholz, H., Goldstein, A.H., Goulden, M.L., et al. (2007) Deriving a light use efficiency model from eddy covariance flux data for predicting daily gross primary production across biomes. *Agric. Forest Meteorol.*, 143, 189–207.



## Chapter 5

### **Role of simulated GOSAT total column CO<sub>2</sub> observations in surface CO<sub>2</sub> flux uncertainty reduction**

(Published in Journal of Geophysical Research Vol. 114, D21208, 2009. Reproduced by permission of American Geographical Union.)

Nikolay Kadygrov<sup>1\*</sup>, Shamil Maksyutov<sup>1</sup>, Nawo Eguchi<sup>1</sup>, Tadao Aoki<sup>1,2</sup>,  
Takakiyo Nakazawa<sup>3</sup>, Tatsuya Yokota<sup>1</sup>, and Gen Inoue<sup>4</sup>

1. Center for Global Environmental Research, National Institute for Environmental Studies, Tsukuba, Ibaraki 305-8506, Japan.
2. Deceased 30 December 2008.
3. Center for Atmospheric and Oceanic Studies, Graduate School of Science, Tohoku University, Sendai, Miyagi 980-8578, Japan.
4. Research Institute for Humanity and Nature, Kyoto 603-8047, Japan.

\*Corresponding author: Dr. Nikolay Kadygrov, Central Aerological Observatory,  
3 Pervomayskaya street Dolgoprudny city, Moscow region 141700, Russia.  
E-mail: kadygrov@gmail.com

## Abstract

We investigated the utility of Greenhouse gases Observing SATellite (GOSAT) column CO<sub>2</sub> observations in surface CO<sub>2</sub> flux estimation. We addressed two key issues in carbon flux estimation from satellite data: (1) reduction of the CO<sub>2</sub> flux uncertainty and (2) bias in the constrained surface fluxes. Our results showed that GOSAT data with 1.7 ppm precision (monthly mean, land observation only) had the same utility as observational data from the existing surface network. By adding satellite observations with 2.5 ppm single-shot precision and a randomly distributed retrieval bias of 1 ppm, it was possible to reduce the mean regional flux uncertainty by approximately 30%. Unbiased data with 2.5 ppm single-shot precision (0.8 ppm for the monthly mean) halved the flux uncertainty. The aerosol-dependent bias in satellite data with 1 ppm mean variance led to significant absolute errors in the surface CO<sub>2</sub> fluxes, highlighting a need for the accurate detection and rejection of biased data.

**Keywords:** *CO<sub>2</sub> flux estimation, CO<sub>2</sub> flux uncertainties, GOSAT column-averaged CO<sub>2</sub>, Surface flux biases*

## 5.1 Introduction

Several studies have estimated the utility of satellite CO<sub>2</sub> data in constraining surface CO<sub>2</sub> fluxes (Rayner and O'Brien, 2001; Houweling et al., 2004; Miller et al., 2007; Chevallier et al., 2007). In these studies, the utility of satellite measurements was investigated using moderate-resolution inverse modeling (inverting approximately 20-100 regions) (Rayner and O'Brien, 2001; Pak and Prather, 2001; Rayner et al., 2002; Patra et al., 2003; Maksyutov et al., 2003) and assimilation-type inverse models at grid-size resolution (Baker et al., 2006; Chevallier et al., 2007). Rayner and O'Brien (2001) showed that monthly averaged column data precision greater than 2.5 ppm on an  $8^\circ \times 10^\circ$  footprint is needed to reach the same performance as the existing surface network.

Miller et al. (2007) recently conducted a detailed investigation of the requirements necessary for CO<sub>2</sub> flux uncertainty reduction in observations of the Orbiting Carbon Observatory (OCO) satellite. The influence of perturbed pseudo-observations on CO<sub>2</sub> flux uncertainties was also evaluated for the OCO (Chevallier et al., 2007). However, the precise requirements and observational impacts of the flux inversion depend on observation frequency and accuracy, which are unique to each satellite.

We used an established inverse model setup that divides the globe into 66 regions to evaluate the utility of column-averaged CO<sub>2</sub> retrieved from spectra in the shortwave infrared (SWIR) band of the Greenhouse gases Observing SATellite (GOSAT). We compared our GOSAT results with estimates from other satellites (Rayner and O'Brien, 2001; Houweling et al., 2004; Miller et al., 2007; Chevallier et al., 2007) and found that GOSAT provided effective CO<sub>2</sub> flux uncertainty reduction, with a comparable utility to the other satellites. We also compared our results with the inversion flux uncertainties of the surface measurement network.

## 5.2 Materials and methods

We were interested in two GOSAT data inversion issues: (a) CO<sub>2</sub> flux uncertainty reduction and (b) the bias in fluxes caused by bias in the observational data. As in many linear inverse problems, the estimated uncertainties of fluxes depend only on the observational errors, not on the data themselves (Rodgers, 2000). For issue (a), we used unbiased data and GOSAT observations with different random errors. For issue (b), we simulated the bias in the total column CO<sub>2</sub> with more realistic random errors (to be used as the “weight” of perturbed observations).

To complete our estimation, we needed to make a number of further steps. First, we simulated the global distribution of total column CO<sub>2</sub> in a  $7.5^\circ \times 7.5^\circ$  footprint over a monthly timescale (aggregated from 4-hourly simulations) in 2005 and simulated the surface network observations. Then, we assigned bias and random errors to all total column CO<sub>2</sub> observations (from both the surface network and satellite). Finally, we estimated the monthly mean CO<sub>2</sub> surface fluxes, and their uncertainties, using a 66-region Bayesian inverse model.

### 5.2.1 Total column CO<sub>2</sub> observations and errors

The GOSAT CO<sub>2</sub> observations simulated here will be acquired every five seconds in the nadir mode (Yokota et al., 2008). The GOSAT observing strategy is to observe CO<sub>2</sub> column-



averaged concentrations under cloud-free conditions, with little disturbance from aerosols and thin clouds. Thus, only approximately 1000 observations per day will be used in the CO<sub>2</sub> retrieval.

To retain integrity, we simulated both the concentrations of CO<sub>2</sub> at surface stations and the global distribution of total column CO<sub>2</sub> from GOSAT in 2005 using a transport model, with climatological CO<sub>2</sub> fluxes obtained from the inverse model (Maksyutov et al., 2007). Following the procedure described by Patra et al. (2003), we used the global transport model developed at the National Institute for Environmental Studies (NIES) and later improved jointly at the Frontier Research System for Global Change (FRSGC) and Tohoku University. Details of the model configuration and performance analysis can be found in a validation paper (Maksyutov et al., 2008b). We used reanalysis wind data from the National Centers for Environmental Prediction (NCEP) at 2.5° resolution.

To simplify the inverse modeling procedure, the satellite data were aggregated to monthly mean values in  $7.5^\circ \times 7.5^\circ$  grid boxes. The total column CO<sub>2</sub> was simulated for every month of 2005, limited to observations over land only. As an example, Figure 5.1a shows the total column CO<sub>2</sub> distribution in July.

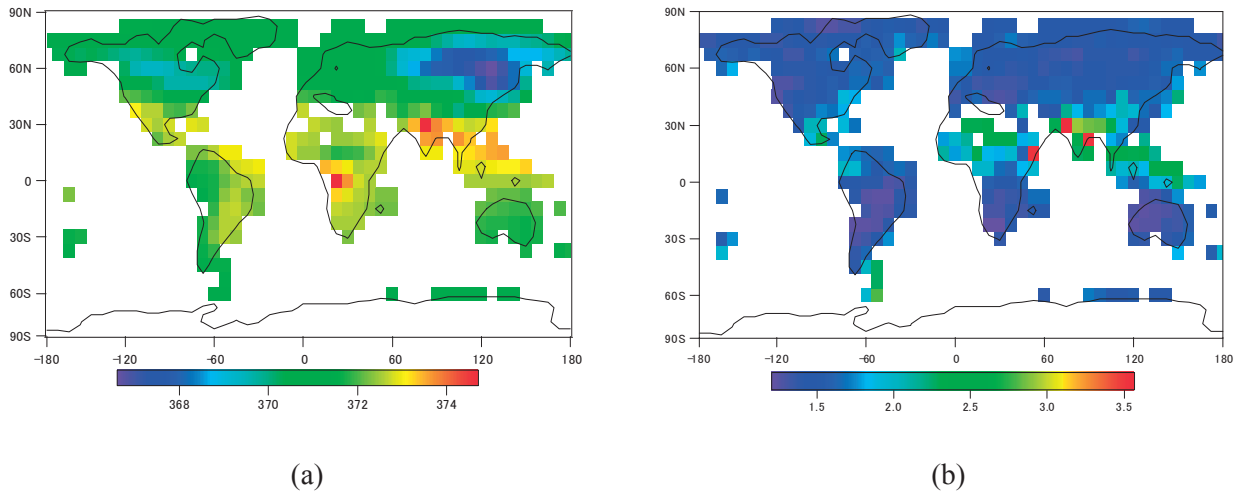


**Figure 5.1** Total column CO<sub>2</sub> and errors (in ppm) for July 2005, with 1.8-ppm error for the monthly mean value ( $\sigma_{\text{sys}} = 1$  ppm).

We simulated two total column CO<sub>2</sub> error types, bias and random error, and assumed that the bias depended on the aerosol optical thickness (AOT) and surface albedo. We used the relationship between the delta column CO<sub>2</sub> albedo and AOT (see Houweling et al., 2004, Figure 5.4), global monthly maps of aerosol optical depth measured by the Multi-angle Imaging Spectrometer (MISR) (Diner et al., 2005), and global albedo maps at 1.64  $\mu\text{m}$  with  $7.5^\circ \times 7.5^\circ$  horizontal resolution derived from the Moderate Resolution Imaging Spectroradiometer (MODIS) (Gao et al., 2005) to simulate the distribution of bias for every month in 2001. Following Houweling et al. (2004), we constructed an empirical relationship among bias, albedo, and AOT. The MODIS-derived albedo data are available at <http://modis.gsfc.nasa.gov/>. Then, we estimated the sensitivity of the fluxes obtained by the inverse model to the biased input data. Figure 5.2 shows the distribution of simulated bias for July 2005.

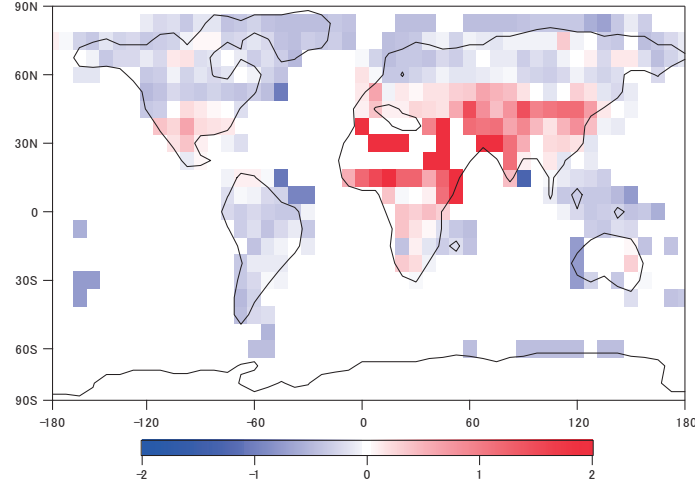


**Figure 5.2 Bias (ppm) for July 2005 (maximum value 3.9 ppm, minimum value -1.3 ppm).**

As proposed by Maksyutov et al. (2008b), the satellite data uncertainty  $\sigma_{total}$  (1) consisted of a random part, which could be reduced by increasing the number of independent observations  $N$ , and a systematic part  $\sigma_{syst}$ , which could involve a concentration retrieval procedure (Yokota et al., 2008) or a clear-sky bias (Corbin and Denning, 2006). Here, we distinguish the absolute bias in the data due to aerosols from the systematic part of the observational uncertainty  $\sigma_{syst}$ , which is a part of  $\sigma_{total}$ . We assumed that the random part was due to errors in the CO<sub>2</sub> column retrievals  $\sigma_{ret}$  and errors caused by atmospheric variability (Gurney et al., 2002) of CO<sub>2</sub>,  $\sigma_{RSD}$ , which also included the transport model error.

In our model, the systematic part of the error was not reduced by increasing the number of observations. It was composed of the spatial, temporal, and representation biases in the concentration retrieval from the GOSAT SWIR spectra. The total column error was given as

$$\sigma_{total} = \sigma_{syst.} + \sqrt{\frac{\sigma_{ret}^2 + \sigma_{RSD}^2}{N}}. \quad (1)$$

The monthly mean number of successful observations  $N$  in our estimates was based on the estimated probability of cloud-free sky  $P_{csr}$  along the GOSAT track and on the  $H$ -ratio of the number of data points with acceptable signal-to-noise ratios (SNRs) to all observational data within a grid box:

$$N = N_0 P_{csr} \frac{H}{100}. \quad (2)$$

$H$  varied from 0 to 100% (see Figure 5.3). The estimated climatology of  $P_{csr}$  was based on data from the Cloud-Aerosol Lidar and Infrared Pathfinder Satellite (CALIPSO) (Winker et al., 2006; Eguchi and Yokota, 2008) during a period from June 2006 to August 2007 (Figure 5.4).

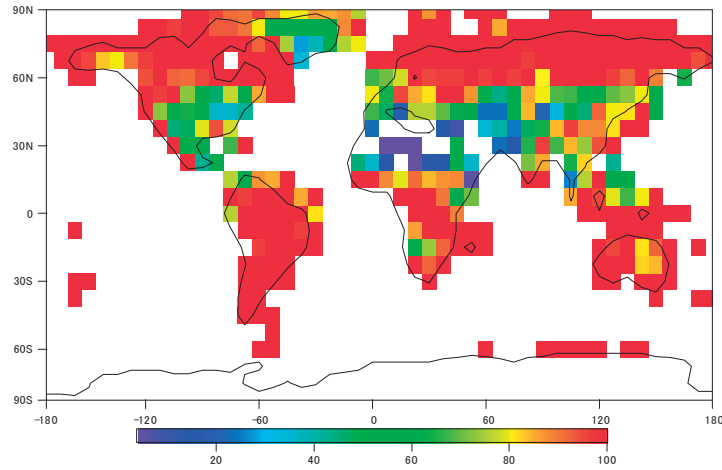


**Figure 5.3** Ratio  $H$  of data (%) with acceptable SNRs to all observational data within a  $7.5^\circ \times 7.5^\circ$  grid box in July 2005.

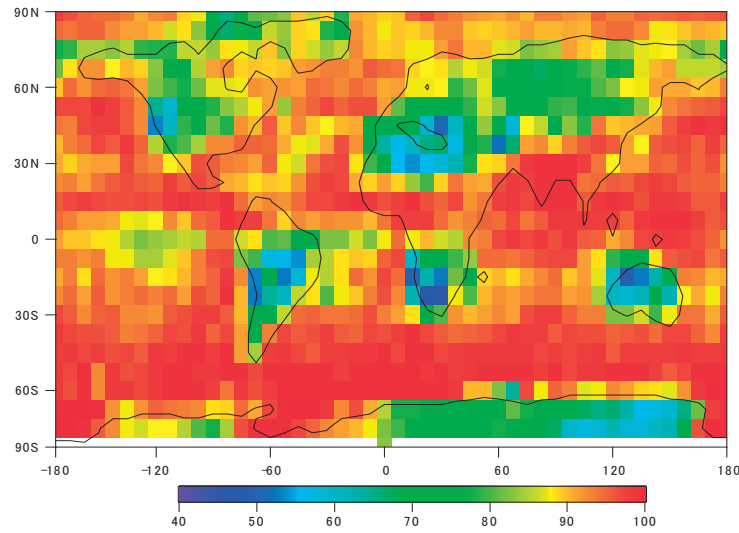


**Figure 5.4** Cloud cover (%) measured by CALIPSO in July 2005.

The  $\sigma_{total}$  should be considered as total column CO<sub>2</sub> uncertainty. After aggregation, the random part of the observational errors (the second term in (1)) was reduced to 0.8 ppm on average, assuming a single-shot retrieval error of 2.5 ppm. The total CO<sub>2</sub> errors were simulated using four different  $\sigma_{syst.}$  values: 0, 1, 2, and 3 ppm. Thus the mean total error for monthly average total column CO<sub>2</sub> varied between 0.8 and 3.8 ppm. Figure 5.1b shows the  $\sigma_{total}$  distribution calculated from (1) for total column CO<sub>2</sub> simulated for GOSAT in July 2005. Even after reductions due to the retrieval restrictions for SNR and cloudy conditions, the number of observations  $N$  (see Figure 5.5) was still quite large for direct use in the Bayesian inverse model of Enting et al. (1995).

We assigned an uncertainty to all simulated data for each month in 2005. The bias for surface stations was assumed to be zero. We used the “time-dependent” residual standard deviations (RSDs) of the CO<sub>2</sub> observations at ground-based stations as the surface data uncertainties (Enting et al., 1995; Maksyutov et al., 2008b). The seasonal-dependent RSDs were obtained from the statistical summary of monthly atmospheric variability described by GLOBALVIEW-CO<sub>2</sub> (2006). GOSAT observations taken during polar night were masked by assigning 100-ppm random error.

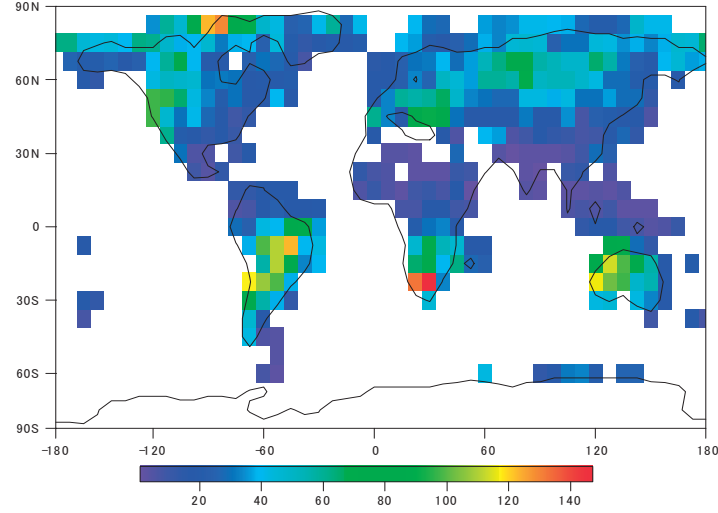


**Figure 5.5** Number of successful observations  $N$  in July 2005.

### 5.2.2 Time-dependent inversion of CO<sub>2</sub>

In the time-dependent inversion, we followed the method developed by Rayner et al. (1999) and later modified to 22- and 66-region cases by Gurney et al. (2004) and Patra et al. (2005), respectively. We used the 66-region configuration model (Maksyutov et al., 2008a) to estimate the uncertainties of monthly mean regional CO<sub>2</sub> fluxes. The monthly carbon emission pulses of 1 GtC yr<sup>-1</sup> intensity from each of the 66 regions were transported using the NIES tracer transport model (Maksyutov et al., 2008b) with  $2.5^\circ \times 2.5^\circ$  horizontal resolution. The model was driven by 2005 wind data from the NCEP reanalysis dataset. Therefore, the influences of regional fluxes on the observed CO<sub>2</sub> concentrations were simulated and summarized as a transport matrix for use in Bayesian synthesis inversion, following the method of Patra et al. (2005).

We used the Bayesian inverse modeling procedure of Gurney et al. (2002), which was based on that of Enting et al. (1995). We minimized a cost function  $F$  to reduce the mismatches between the atmospheric observations  $D$  and the responses to surface fluxes predicted by the transport model,  $G \cdot S$  (where  $G$  is the transport operator), and between the *a priori* and predicted fluxes,  $S^0$  and  $S$ , respectively:

$$F = (D - G \cdot S) \cdot C_D^{-1} \cdot (D - G \cdot S)^T + (S - S^0) \cdot C_{S^0}^{-1} \cdot (S - S^0)^T. \quad (3)$$

The solution to the inverse model provided optimal estimates for the regional fluxes and the *a posteriori* error covariance of the flux estimates  $C_S$ :

$$C_S = (G^T \cdot C_D^{-1} \cdot G + C_{S^0}^{-1})^{-1}, \quad (4)$$

where  $C_D$  and  $C_{S^0}$  are error covariance matrices of the atmospheric observations and *a priori* fluxes, respectively.

According to (4), the flux uncertainties are independent of the observed concentrations and prior fluxes and depend only on the observational uncertainties, prior flux uncertainties, and atmospheric transport. Therefore, we can discuss flux uncertainties without using real observations. Our “real” observations were used to investigate the influence of perturbed concentrations (with absolute bias) on the CO<sub>2</sub> fluxes. However, we used the four different parts of  $\sigma_{total}$  (not to be confused with the absolute bias) in the CO<sub>2</sub> flux error estimation. The error covariance matrix  $C_D$  was assumed to be diagonal, where each diagonal element was equal to the squared data uncertainty  $\sigma_{total}^2$ . The prior flux uncertainties  $C_{S^0}$  for each region (see (3)) were set as proportional to the regional net primary production (NPP) for land and the oceanic bulk exchange for ocean, following Gurney et al. (2002). After this, we normalized the bias by subtracting the average value and dividing by its standard deviation. Thus, the average bias was almost zero, but there were some local areas with high bias values in the regions with large aerosol optical thickness anomalies. We only used the data with bias lower than 4 ppm, based on the assumption that the bias was already accounted for by retrieval, calibration, and validation procedures. We assumed that the spatially random part of the bias was included in  $\sigma_{total}$ .

## 5.3 Results and discussions

### 5.3.1 Flux uncertainty reduction

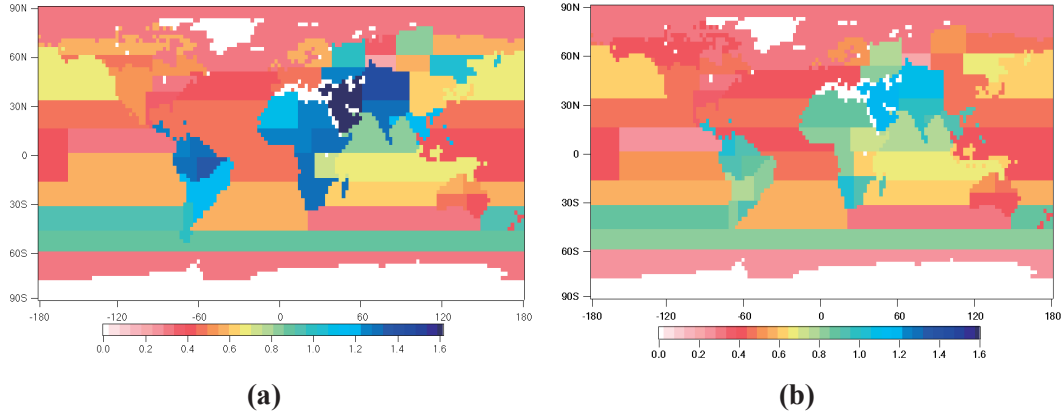
We initially reduced the flux uncertainties by adding ground-based observations, following Gurney et al. (2002), and then adding the simulated GOSAT observations with assumed uncertainties. Figures 5.6a and 5.6b show the flux uncertainties for (a) when only ground-based observations were used and (b) when both ground-based and GOSAT observations were used. In the first case, 151 stations were used in the inversion, while in the second case there were additional GOSAT observations aggregated to  $7.5^\circ \times 7.5^\circ$  grids over land for each month (565 additional points in total). Hereafter, we refer to the uncertainties in the flux in (a) and (b) as  $\sigma_{S,GV}$  and  $\sigma_{S,GV+GOSAT}$ , respectively. In Figure 5.6b, GOSAT observational data were assumed to have a 1-ppm bias and 2.5-ppm single-shot accuracy, corresponding to 1.8 ppm for the monthly mean error. For that case, the average reduction for land regions was about 30%. The relative reduction of mean flux uncertainty was defined as  $1 - \sigma_{S,GV+GOSAT} / \sigma_{S,GV}$ .

Figure 5.7 shows the relative reduction of annual CO<sub>2</sub> flux uncertainty for each of the 66 GOSAT data regions with 1.8-ppm monthly mean error. Following Rayner and O’Brien (2001), we calculated the total uncertainty  $\Sigma$  as

$$\Sigma = \sqrt{\sum_n \sigma_n^2}, \quad (5)$$

where  $\sigma_n$  is the flux uncertainty for region  $n$ , and the sum is over all 66 regions. Also following Rayner and O’Brien (2001), we expressed the sensitivity of the source uncertainty

$\Sigma$  as a function of the pseudo-data precision (Figure 5.8). When compared to the existing network of ground stations, our results indicated that the monthly averaged column data precision  $\sigma_{total}$  on  $7.5^\circ \times 7.5^\circ$  grids needed to be finer than 0.8 ppm to reduce the average uncertainties for all 66 regions by 50%.



**Figure 5.6 CO<sub>2</sub> flux uncertainties in 2005 (GtC yr<sup>-1</sup> region<sup>-1</sup>).** (a) Surface stations only and (b) surface stations and simulated GOSAT data with 1.8-ppm precision for the monthly mean ( $\sigma_{syst} = 1$  ppm) were used in the inversion.

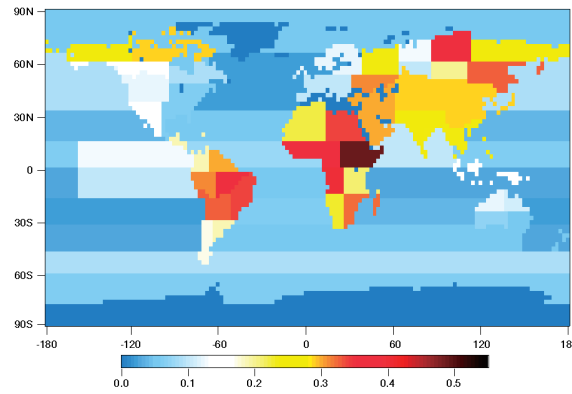


**Figure 5.7 Monthly mean reduction (× 100%) in the annual CO<sub>2</sub> flux uncertainties of GOSAT data with 1.8-ppm precision ( $\sigma_{syst} = 1$  ppm).**

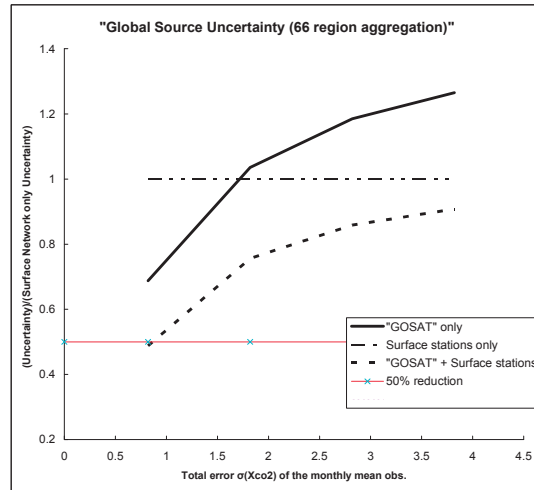


**Figure 5.8 Relative CO<sub>2</sub> flux uncertainties for different monitoring network configurations.** The dash-dot line shows the existing surface network case. The thin solid line shows the 50% reduction level of total flux uncertainties.

We can conclude that the high-precision satellite measurements were as effective as the surface observations in reducing the estimated flux uncertainty in the time-dependent inverse model. Data from GOSAT are expected to reduce flux uncertainty by as much as 50% for certain regions with low densities of existing ground-based observations (see Figure 5.7).

### 5.3.2 Perturbed data and bias in fluxes

The simulated bias varied from month to month over a range of -1.5 to 4 ppm. For example, in July 2005, the bias standard deviation was 0.9 ppm (see Figure 5.2). We defined the bias such that it could either increase or decrease the observational values. We quantified the impact of the total column CO<sub>2</sub> data bias on the inversion by the model sensitivity, which we defined as the difference between the calculated posterior fluxes with and without perturbed pseudo-observations. The fluxes obtained without bias in the input data were assumed to be the “true” predicted fluxes. Figure 5.9 shows the result of perturbing the total column CO<sub>2</sub> by adding the absolute bias to the unbiased GOSAT measurements for July 2005. We compared the corrections to the prior fluxes obtained from unbiased observations (see Figure 5.10a) with the perturbed observations (see Figure 5.10b). Our results (see Figures 5.10c, 5.11) indicated that the fluxes were very sensitive to biased observations, and perturbation with 1-ppm  $\sigma$  caused absolute errors comparable to the total flux values. The problem of flux constraint becomes unresolved when the noise background is too large.



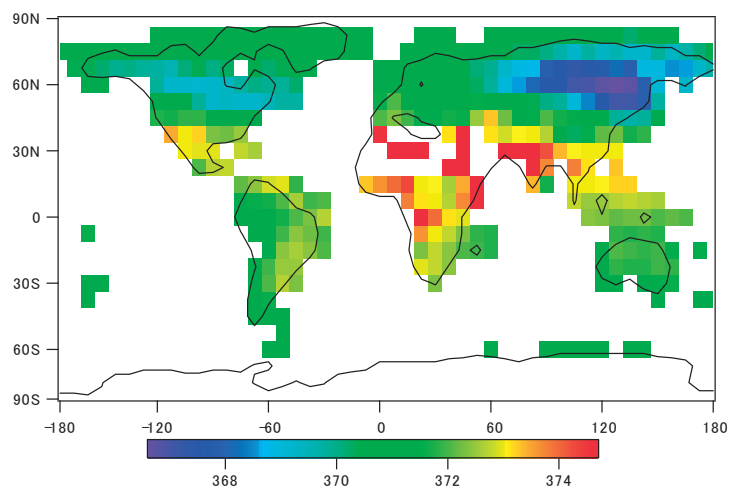


**Figure 5.9** Total column CO<sub>2</sub> (ppm) in July 2005, perturbed by bias.

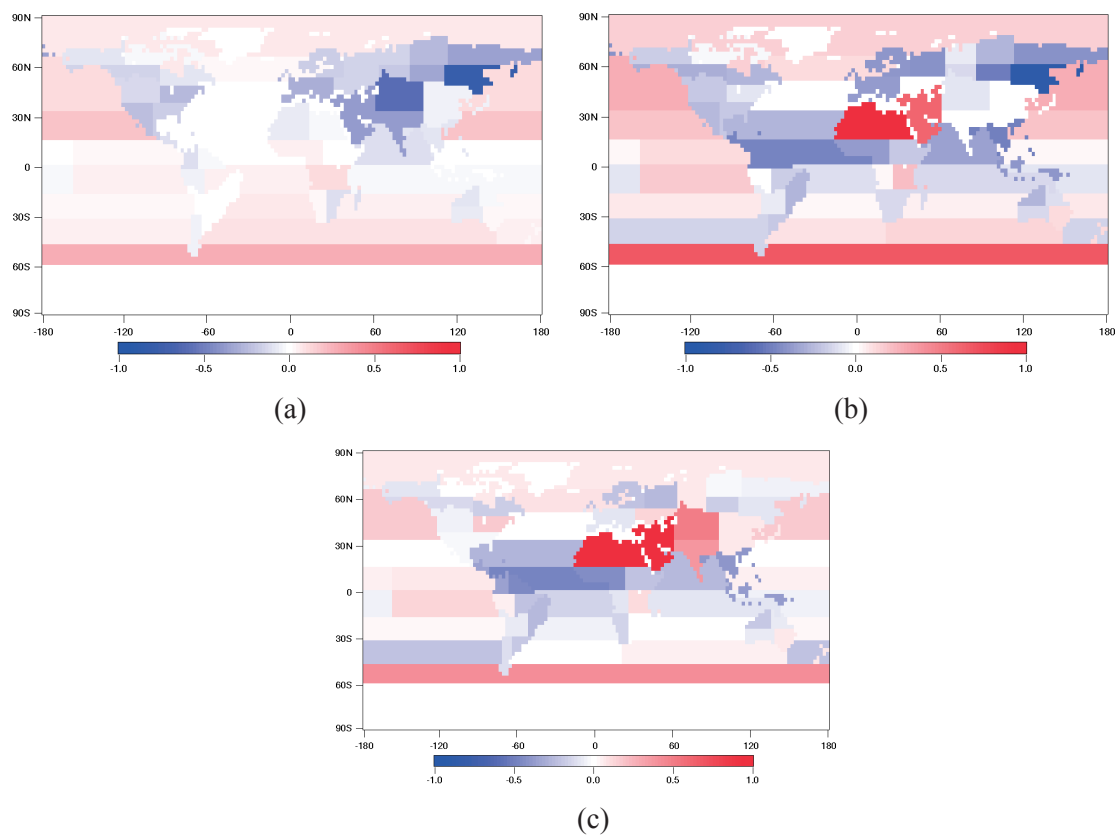


**Figure 5.10** Corrections (GtC yr<sup>-1</sup> region<sup>-1</sup>) of *a priori* fluxes in July 2005 with different inverse model configurations. (a) No bias in GOSAT observations (minimum = -0.78, maximum = 0.27). (b) Biased GOSAT observations (minimum = -0.87, maximum = 2.25). (c) Errors in the fluxes due to bias in GOSAT CO<sub>2</sub> data (minimum = -0.47, maximum = 2.29).

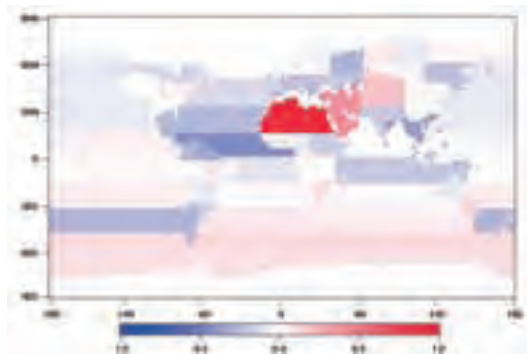


**Figure 5.11** Same as Figure 5.10c, but for the annual flux in 2005 (minimum = -0.44, maximum = 2.88).

## 5.4 Conclusions

We used an inverse model of atmospheric transport in order to evaluate performance and utility of GOSAT observations of total column CO<sub>2</sub>. One of the examined tasks was flux uncertainty reduction caused by extending the CO<sub>2</sub> surface observational network with GOSAT data. New numerical evaluations were aimed to get additional knowledge which would help us to build the reliable level 4 of the GOSAT mission containing CO<sub>2</sub> flux data. We estimated monthly fluxes and flux uncertainties via the inverse procedure. The NIES transport model has given us global distribution of total column CO<sub>2</sub> and has made it possible to simulate satellite observations on desirable time spatial resolution. We aggregated the simulated GOSAT data to  $7.5^\circ \times 7.5^\circ$  grid cells and averaged over 1 month to derive total CO<sub>2</sub> column monthly mean data. The number of successfully retrieved GOSAT data in our analysis was corrected by clear-sky factors, assuming a global mean clear-sky probability of 11%. One of the significant improvements to our previous studies (Maksyutov et al., 2008a) is screening the GOSAT observational frequency by a specific GOSAT signal-to-noise ratio distribution. Moreover, more precise evaluations of retrieval errors gave us the possibility to make our simulations as close to the real cases as possible. Our results showed that the total errors in the monthly averaged column data needed to be less than 0.8 ppm to reduce the mean regional flux uncertainties by 50% for a time-dependent 66-region inversion setup. As expected, we also found that uncertainty was reduced in regions with low surface observation densities. This result is also in good agreement with our previous 22-region version setup (Maksyutov et al., 2008a).

As a result of the studies on total error dependence on biased data we found that bias contributes a lot to the total error with significant power. To compensate for this, reduction of the random error has become important in time-dependent cyclostationary analyses; in addition, one should make efforts to eliminate biases.

In this study, we used a simplified criterion for biased data rejection; this criterion should be made more selective. A more detailed study of observation biases as functions of thin cloud cover, aerosols, and other retrieval-related parameters would also help to evaluate the utility of GOSAT observations for various applications. We found that bias in the data had a remarkable influence on the absolute flux errors. Bréon et al. (2005) and Houweling et al. (2005) have both noted that small, unbiased data sets generally yield more accurate flux estimates than large, biased ones. Presented simulations were performed with strict

restrictions for model parameters. Further, retrieval error for single-shot measurement was 1%; in any contentious cases concerning presence of clouds,  $P_{\text{csr}}$  was assumed to be zero. We tried to avoid underestimation of GOSAT performance, and our results show significant improvement in the tasks of CO<sub>2</sub> flux uncertainty reduction.

## References

- Baker, D.F., Doney, S.C., Schimel, D.S. (2006) Variational data assimilation for atmospheric CO<sub>2</sub>. *Tellus*, 58B, 359–365.
- Bréon, F.M., O’Brien, D.M., Spinhirne, J.D. (2005) Scattering layer statistics from space borne GLAS observations. *Geophys. Res. Lett.*, 32, L22802, doi:10.1029/2005GL023825.
- Chevallier, F., Bréon, F.-M., Rayner, P.J. (2007) Contribution of the Orbiting Carbon Observatory to the estimation of CO<sub>2</sub> sources and sinks: Theoretical study in a variational data assimilation framework. *J. Geophys. Res.*, 112, D09307, doi:10.1029/2006JD007375.
- Corbin, K.D., Denning, A.S. (2006) Using continuous data to estimate clear-sky errors in inversions of satellite CO<sub>2</sub> measurements. *Geophys. Res. Lett.*, 33, L12810, doi:10.1029/2006GL025910.
- Diner, D.J., Braswell, B.H., et al. (2005) The value of multiangle measurements for retrieving structurally and radiatively consistent properties of clouds, aerosols, and surfaces. *Rem. Sens. Environ.* 97 (4), 495–518.
- Eguchi, N., Yokota, T. (2008) Investigation of clear-sky occurrence rate estimated from CALIOP and MODIS observations. *Geophys. Res. Lett.*, 35, L23816, doi:10.1029/2008GL035897.
- Enting, I.G., Trudinger, C.M., Francey, R.J. (1995) A synthesis inversion of the concentration of  $\delta^{13}\text{C}$  of atmospheric CO<sub>2</sub>. *Tellus*, 47B, 35–51.
- Gao, F., Schaaf, C.B., Strahler, A.H., Roesch, A., Lucht, W., Dickinson, R. (2005) MODIS bidirectional reflectance distribution function and albedo Climate Modeling Grid products and the variability of albedo for major global vegetation types. *J. Geophys. Res.*, 110, D01104, doi:10.1029/2004JD005190.
- GLOBALVIEW-CO<sub>2</sub> (2006) Cooperative Atmospheric Data Integration Project – Carbon Dioxide. CD-ROM, NOAA ESRL, Boulder, Colorado (Also available on the internet *via* anonymous FTP to ftp.cmdl.noaa.gov, path: ccg/co2/GLOBALVIEW).
- Gurney, K.R., et al. (2002) Towards robust regional estimates of CO<sub>2</sub> sources and sinks using atmospheric transport models. *Nature*, 415, 626–630.
- Gurney, K.R., et al. (2004) Transcom 3 inversion intercomparison: Model mean results for the estimation of seasonal carbon sources and sinks. *Global Biogeochem. Cycles*, 18, GB1010, doi:10.1029/2003GB002111.
- Houweling, S., Breon, F.M., Aben, I., Rödenbeck, C., Gloor, M., Heimann, M., Ciais, P. (2004) Inverse modeling of CO<sub>2</sub> sources and sinks using satellite data: A synthetic inter-comparison of measurement techniques and their performance as a function of space and time. *Atm. Chem. Phys.*, 4, 523–538.
- Houweling, S., Hartmann, W., Aben, I., Schrijver, H., Skidmore, J., Roelofs, G.-J., Breon, F.-M. (2005) Evidence of systematic errors in SCIAMACHY-observed CO<sub>2</sub> due to aerosols. *Atmos. Chem. Phys.*, 5, 3003–3013.
- Maksyutov, S., Patra, P.K., Inoue, G. (2003) Pseudo-data inversion of column-CO<sub>2</sub> observations by remote sensing using a high resolution inverse model, *International Archives of Photogrammetry. Remote Sensing and Spatial Information System*, XXXIV, 7/W14, J-2.
- Maksyutov, S., Onishi, R., Naja, M., Yaremchuk, A., Patra, P., Inoue, G. (2007) Atmospheric CO<sub>2</sub> Simulations with a High Resolution Model and Synoptic Scale Variability of CO<sub>2</sub> Column, CGER Supercomputer Activity Report, vol. 14-2005, CGER-I070-2007, CGER NIES, Tsukuba, Japan, 49–54.
- Maksyutov, S., Kadyrov, N., Nakatsuka, Y., Shirai, T., et al. (2008a) Application of the transport model for inverse modeling studies of the regional and global budgets of CO<sub>2</sub>. CGER Supercomputer Activity Report, CGER-I078-2008, CGER NIES, Tsukuba, Japan, 23–32.

- Maksyutov, S., Patra, P.K., Onishi, R., Saeki, T., Nakazawa, T. (2008b) NIES/FRCGC global atmospheric tracer transport model: description, validation, and surface sources and sinks inversion. *J. Earth Simulator*, 9, 3–18.
- Miller, C.D., Crisp, D., DeCola, P.I., Olsen, S.C., et al. (2007) Precision requirements for space-based  $X_{CO_2}$  data. *J. Geophys. Res.*, 112, D10314, doi:10.1029/2006JD007659.
- Pak, B.M., Prather, J. (2001) CO<sub>2</sub> source inversions using satellite observations of the upper troposphere. *Geophys. Res. Lett.*, 28, 4571–4574.
- Patra, P.K., Maksyutov, S., Sasano, Y., Nakajima, H., Inoue, G., Nakazawa, T. (2003) An evaluation of CO<sub>2</sub> observations with Solar Occultation FTS for Inclined-Orbit Satellite sensor for surface source inversion. *J. Geophys. Res.*, 108(D24), 4759, doi:10.1029/2003JD003661.
- Patra, P.K., Ishizawa, M., Maksyutov, S., Nakazawa, T., Inoue, G. (2005) Role of biomass burning and climate anomalies on land-atmosphere carbon fluxes based on inverse modelling of atmospheric CO<sub>2</sub>. *Global Biogeochem. Cycles*, 19, GB3005, doi:10.1029/2004GB002258.
- Rayner, P., Enting, I., Francey, R., Langenfelds, R. (1999) Reconstructing the recent carbon cycle from atmospheric CO<sub>2</sub>,  $\delta^{13}C$  and O<sub>2</sub>/N<sub>2</sub> observations. *Tellus*, 51B, 213–232.
- Rayner, P.J., O'Brien, D.M. (2001) The utility of remotely sensed CO<sub>2</sub> concentration data in surface inversion. *Geophys. Res. Lett.* 28, 175–178.
- Rayner, P.J., Law, R.M., O'Brien, D.M., Butler, T.M., Dilley, A.C. (2002) Global observations of the carbon budget, 3, Initial assessment of the impact of satellite orbit, scan geometry, and cloud on measuring CO<sub>2</sub> from space. *J. Geophys. Res.*, 107(D21), 4557, doi:10.1029/2001JD000618.
- Rodgers, C.D. (2000) *Inverse Methods for Atmospheric Sounding, Theory and Practice*. World Scientific Publishing Co., Singapore, 67.
- Winker, D.M., Hostetler, C.A., Vaughan, M.A., Omar, A.H. (2006) CALIOP, Algorithm Theoretical Basis Document, Part 1: CALIOP Instrument, and Algorithms Overview.
- Yokota, T., Aoki, T., Eguchi, N., Ota, Y. (2008) Data retrieval algorithms of the SWIR bands of the TANSO-FTS sensor onboard GOSAT. *J. Remote Sens. Soc. Jap.*, 28, 2, 132–142.

## **CGER'S SUPERCOMPUTER MONOGRAPH REPORT**

### **Back Issues**

- Vol. 1 CGER-I021-'96 (Out of stock)  
Turbulence Structure and CO<sub>2</sub> Transfer at the Air-Sea Interface and Turbulent Diffusion in Thermally-Stratified Flows
- Vol. 2 CGER-I022-'96  
A Transient CO<sub>2</sub> Experiment with the MRI CGCM -Annual Mean Response -
- Vol. 3 CGER-I025-'97  
Study on the Climate System and Mass Transport by a Climate Model
- Vol. 4 CGER-I028-'97 (Out of stock)  
Development of a Global 1-D Chemically Radiatively Coupled Model and an Introduction to the Development of a Chemically Coupled General Circulation Model
- Vol. 5 CGER-I035-'99  
Three-Dimensional Circulation Model Driven by Wind, Density, and Tidal Force for Ecosystem Analysis of Coastal Seas
- Vol. 6 CGER-I040-2000  
Tropical Precipitation Patterns in Response to a Local Warm SST Area Placed at the Equator of an Aqua Planet
- Vol. 7 CGER-I045-2001  
New Meteorological Research Institute Coupled GCM (MRI-CGCM2)  
Transient Response to Greenhouse Gas and Aerosol Scenarios
- Vol. 8 CGER-I055-2003 (Out of stock)  
Transient Climate Change Simulations in the 21st Century with the CCSR/NIES CGCM under a New Set of IPCC Scenarios
- Vol. 9 CGER-I057-2004  
Vortices, Waves and Turbulence in a Rotating Stratified Fluid
- Vol. 10 CGER-I060-2005  
Modeling of Daily Runoff in the Changjiang (Yangtze) River Basin and Its Application to Evaluating the Flood Control Effect of the Three Gorges Project
- Vol. 11 CGER-I063-2006  
Development of Process-based NICE Model and Simulation of Ecosystem Dynamics in the Catchment of East Asia (Part I)
- Vol. 12 CGER-I073-2007  
Climate Change Simulations with a Coupled Ocean-Atmosphere GCM Called the Model for Interdisciplinary Research on Climate: MIROC
- Vol. 13 CGER-I080-2008  
Simulations of the Stratospheric Circulation and Ozone during the Recent Past (1980-2004) with the MRI Chemistry-Climate Model
- Vol. 14 CGER-I083-2008  
Development of Process-based NICE Model and Simulation of Ecosystem Dynamics in the Catchment of East Asia (Part II)

Copies of these reports can be obtained by contacting:  
Center for Global Environmental Research  
National Institute for Environmental Studies  
16-2 Onogawa, Tsukuba, Ibaraki 305-8506, Japan

These reports are also available as PDF files.  
See: [http://www-cger.nies.go.jp/cger-e/e\\_report/r\\_index-e.html](http://www-cger.nies.go.jp/cger-e/e_report/r_index-e.html)

